

AB INITIO NONSELF-CONSISTENT FACTORIZED
LCAO CALCULATIONS ON THE ELECTRONIC
STRUCTURE OF $(\text{ZnSe})_m(\text{ZnS})_n$ STRAINED-
LAYER SUPERLATTICES

By

TODD SCOTT MARSHALL

Bachelor of Science
California State University
Hayward, California
1984

Master of Science
San Jose State University
San Jose, California
1987

Submitted to the faculty of the
Graduate College of the
Oklahoma State University
in partial fulfillment of
the requirements for
the Degree of
DOCTOR OF PHILOSOPHY
December, 1993

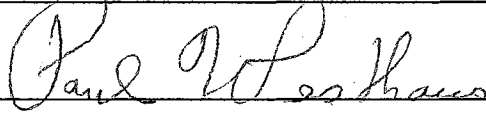
AB INITIO NONSELF-CONSISTENT FACTORIZED
LCAO CALCULATIONS ON THE ELECTRONIC
STRUCTURE OF $(\text{ZnSe})_m(\text{ZnS})_n$ STRAINED-
LAYER SUPERLATTICES

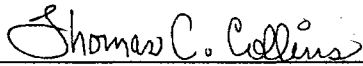
Thesis Approved:

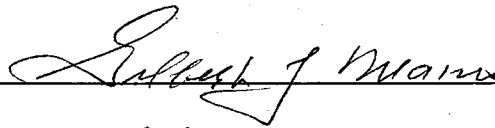


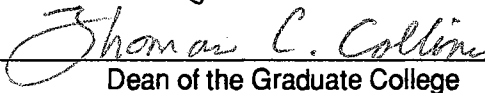
Thesis Adviser











Dean of the Graduate College

ACKNOWLEDGMENTS

I can still remember starting the drive from College Park to Stillwater on Christmas Day of 1989. I was leaving a nationally ranked graduate program that had over two hundred graduate students for one that had about forty and was feeling apprehensive about the transfer. After one week of research under Professor T. M. Wilson and Group Theory under Professor E. E. Lafon, though, this apprehension was gone. Both of these men have had a impact on my physics career, Professor Wilson through his patience and guidance as my doctoral advisor and Professor Lafon through his FLCAO code.

I would like to thank Professors T. C. Collins, G. S. Dixon, G. J. Mains, S. W. S. McKeever, and P. A. Westhaus for their willingness to serve on my graduate committee. In addition, I would like to thank Konrad Brandemuhl, Lorraine Goff, and David Worrell of the University Computing Center for their cooperation. During my doctoral research at Oklahoma State University, I was a recipient of a United States Department of Education fellowship (grant number P-200-A-900-59) and was a research assistant on the project for the "characterization of II-VI materials for optical technology applications" funded by the Defense Advanced Research Projects Agency (contract number MDA972-89-K-100). I would also like to thank the Department of Physics for the tuition waivers and teaching assistantships I have received and for the opportunity to be the instructor of the Physics 1114 course during the 1992 Summer semester.

In closing these acknowledgments, I would like to thank my beautiful wife for her love and support. While I was writing this thesis, Sherry Lynn was taking care of the minor issues such as finding us a place to live in El Paso and the packing and moving of our belongings. In addition, I would like to thank my in-laws, Dick and Mary Ann Taylor, for the kindness and generosity they have shown me this past year.

TABLE OF CONTENTS

Chapter	Page
I. INTRODUCTION	1
Crystal Growth	1
Technological Importance	2
Photoluminescence and Absorption Studies	6
Local Density Functional Approximation	6
<i>ab initio</i> LCAO Calculations	
II. THE FLCAO FORMULATION	11
Introduction	11
The Energy Matrix	13
The Atomic Orbitals	15
The Crystalline Potential	16
The Overlap Matrix Elements	20
The Kinetic Energy Matrix Elements	21
The Potential Energy Matrix Elements	22
Density of States	25
III. BULK ZnSe AND ZnS	27
Introduction	27
The Unit Cell	28
The Crystalline Potential	33
The Basis	33
Electronic Band Structure Results	37
IV. THE $(\text{ZnSe})_m(\text{ZnS})_n$ SLS's	51
Introduction	51
Elastic Strain	55
Electronic Band Structure and Density of States	64
Band Offsets	92
V. CONCLUSIONS	99
The FLCAO Method	100
The $(\text{ZnSe})_m(\text{ZnS})_n$ SLS's	102
BIBLIOGRAPHY	104

LIST OF TABLES

Table	Page
I. Coefficients for the analytic atomic-centered potentials of bulk ZnSe and ZnS	34
II. Gaussian orbital exponents and expansion coefficients for ZnSe	38
III. Gaussian orbital exponents and expansion coefficients for ZnS	40
IV. Calculated atomic core-like energies of bulk ZnSe and ZnS at the band edge	42
V. Calculated energies at high symmetry points for bulk ZnSe and ZnS	45
VI. Calculated energies at high symmetry points for bulk ZnSe	46
VII. Calculated energies at high symmetry points for bulk ZnS	47
VIII. Scaling factor of the k-points in the irreducible wedge	49
IX. Lattice constants for the $(\text{ZnSe})_m(\text{ZnS})_n$ SLS's	60
X. Adjusted linear coefficients for the ACP's of the $(\text{ZnSe})_m(\text{ZnS})_n$ SLS's	66
XI. Calculated atomic core-like energies of the $(\text{ZnSe})_1(\text{ZnS})_1$ SLS	75
XII. Calculated energies at the $\bar{\Gamma}$ -point for the $(\text{ZnSe})_1(\text{ZnS})_1$ SLS	79
XIII. The apparent chemical shift for the atomic-like Zn core states	93
XIV. The true chemical shift for the atomic-like Zn core states	94
XV. Lattice parameters for the bulk-like electronic structure calculations	96
XVI. The calculated band offsets of the $(\text{ZnSe})_5(\text{ZnS})_n$ SLS's for $n=10, 15,$ and 20	98
XVII. Computational time needed for the evaluation of the energy matrix elements and the diagonalization of the energy matrix	101

LIST OF FIGURES

Figure	Page
1. The crystal lattice structure of the $(\text{ZnSe})_1(\text{ZnS})_1$ SLS	3
2. The band alignments for type-I and type-II superlattices	5
3. Photoluminescence and absorption spectrums for the ZnSe (50 Å) - ZnS (20 Å) SLS	7
4. The crystal structure of znicblende compounds	29
5. The first Brillouin zone of the face-centered cubic lattice	31
6. The first Brillouin zone fo the tetragonal lattice	32
7. The difference between the numeric and analytic crystalline potentials for bulk ZnSe	35
8. The electronic band structure and total density of states of bulk ZnSe	43
9. The electronic band structure and total density of states of bulk ZnSe	44
10. The $m+n$ unique interatomic distances along the (001) growth direction for the $(\text{ZnSe})_m(\text{ZnS})_n$ SLS	57
11. The electronic band structure and total density of states of the $(\text{ZnSe})_1(\text{ZnS})_1$ SLS	76
12. The partial density of states for the Zn, Se, and S atoms in the $(\text{ZnSe})_1(\text{ZnS})_1$ SLS	77
13. The difference in energy between the light-hole and heavy-hole states at the band edge as a function of the number of monolayers	80
14. Partial density of states for Se in the $(\text{ZnSe})_7(\text{ZnS})_7$ SLS	82
15. Partial density of states for S in the $(\text{ZnSe})_7(\text{ZnS})_7$ SLS	83
16. Partial density of states for Zn in the $(\text{ZnSe})_7(\text{ZnS})_7$ SLS	84
17. Partial density of states for Se in the $(\text{ZnSe})_5(\text{ZnS})_9$ SLS	85

Figure	Page
18. Partial density of states for S in the $(\text{ZnSe})_5(\text{ZnS})_9$ SLS	86
19. Partial density of states for Zn in the $(\text{ZnSe})_5(\text{ZnS})_9$ SLS	87
20. The partial density of states for Zn, Se, and S in the $(\text{ZnSe})_7(\text{ZnS})_7$ SLS	89
21. The partial density of states for Zn, Se, and S in the $(\text{ZnSe})_5(\text{ZnS})_9$ SLS	90
22. The band gap energy for the $(\text{ZnSe})_m(\text{ZnS})_n$ SLS's	91

CHAPTER I

INTRODUCTION

Crystal Growth

$(\text{ZnSe})_m(\text{ZnS})_n$ strained-layer superlattices (SLS's) are manmade common-cation (Zn) II-VI heterostructures constructed by alternating m monolayers of ZnSe with n monolayers of ZnS for several periods (20-100) along the growth direction, generally chosen to be the (001) direction. Ideally, the SLS's would be grown on a substrate of bulk ZnSe. Since substrate quality bulk ZnSe has not yet been obtained, however, GaAs is typically used because of the small 0.3% mismatch between the lattice constants of bulk GaAs and ZnSe. With such a small mismatch, the possibility of dislocations at the substrate-ZnSe interface, which would result in poor quality ZnSe monolayers, is significantly reduced. The most widely used crystal growth techniques for the fabrication of the $(\text{ZnSe})_m(\text{ZnS})_n$ SLS's are metalorganic chemical vapor deposition (MOCVD) [e.g., Kawakami and Taguchi (1,2), Yamada *et al* (3), Parbrook *et al* (4-6), and Shen *et al* (7)]; metalorganic vapor phase epitaxy (MOVPE) [e.g., Yokogawa *et al* (8,9)]; metalorganic molecular beam epitaxy (MOMBE) [e.g., Teraguchi *et al* (10,11) and Oniyama *et al* (12)]; and molecular beam epitaxy (MBE) [e.g., Shen *et al* (13)]. Such techniques allow for clean interfaces, free of dislocations and good, but not precise, control over the number of monolayers. In addition, the low growth temperature (300-400 °C) results in a reduced contamination from the growth system. The $(\text{ZnSe})_m(\text{ZnS})_n$ SLS's are typically classified as either short-, medium- or long-period, where the criteria for which classification a specific SLS falls into is rather ambiguous. In general, the requirement for a SLS to be regarded as short-period is that the maximum thickness of either constituent compound is roughly 20 Å ($m, n \leq 7$). To be regarded as a medium-period SLS, the thickness of at least one compound is roughly

greater than 20 Å but less than 55 Å ($8 \leq m$ and/or $n \leq 20$). Should the thickness of either or both materials exceed 55 Å, then the SLS is classified as long-period. The crystal lattice structure for the short-period $(\text{ZnSe})_1(\text{ZnS})_1$ is shown in Figure 1. Experimentally, studies are restricted to the medium- and long-period SLS's because of the unavoidable fluctuations in the number of monolayers. For long-period SLS's, such fluctuations will have a negligible impact on the electronic properties. For short-period SLS's, however, such fluctuations would result in the non-uniformity of the electronic properties throughout the structure. On the other hand, practical computational limits restrict theoretical studies to the short-period SLS's.

Elastic strain is introduced into the crystal superlattice structure through the large 4.5% mismatch between the lattice constants of ZnSe (5.66 Å) and ZnS (5.41 Å). The strain acts to deform the crystal lattice structure and reduces the symmetry from cubic to tetragonal. Thus, the electronic properties of these SLS's are expected to differ from those found in the bulk compounds. The strain has been found to depend on the number of monolayers of each constituent compound (i.e. the set of $\{m,n\}$ values) so that the electronic properties can, in a sense, be manipulated. Should the thickness of either compound exceed a critical thickness h_c , however, then the strain is relieved and dislocations are formed at the interfaces (i.e. bonds between zinc and nearest neighbor selenium/sulfur atoms are broken). While the exact value of h_c is still unknown, Kawakami *et al* (14,15) determined the range of this value to be 100-200 Å through x-ray diffraction and transmission electron spectroscopy measurements.

Technological Importance

Bulk II-VI semiconductor compounds are known to have direct, wide band gaps at room temperature and high fractional ionic characters. It is assumed that the heterostructures constructed from these compounds will also have this nature, while offering desirable electronic properties which are not found in the constituent bulk compounds. Thus, recent interest has been given to these heterostructures as potential candidates in the development of tunable color light-emitting-diodes (LED's) and short wavelength semiconductor lasers. Also assumed,

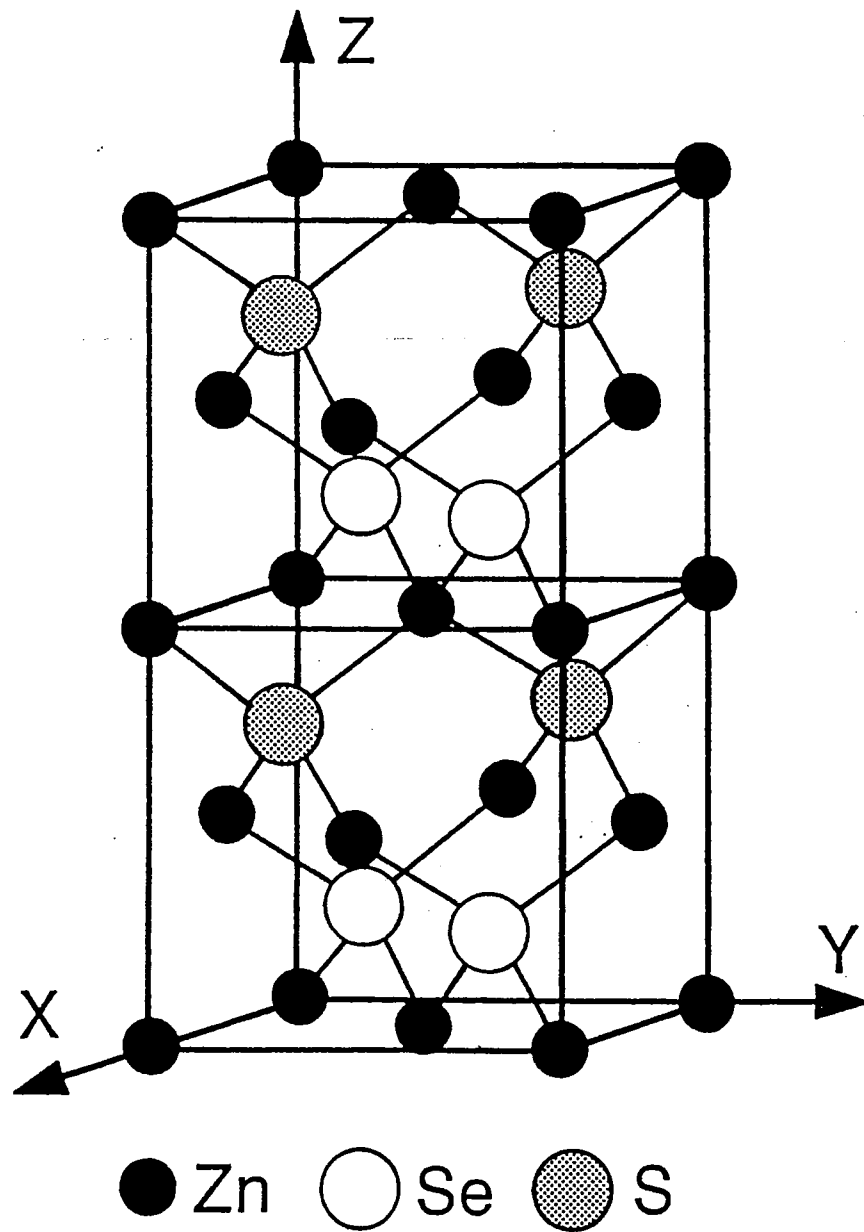


Figure 1. The crystal lattice structure of the $(\text{ZnSe})_1(\text{ZnS})_1$ strained-layer superlattice.

is that these heterostructures will form either a type-I or a type-II superlattice, as shown in Figure 2 for the $(\text{ZnSe})_m(\text{ZnS})_n$ SLS. In the case of a type-I superlattice, one of the two constituent compounds will serve as a quantum well to both the holes and electrons. For a type-II superlattice, however, one compound will serve as a quantum well to the holes and the other as a quantum well to the electrons. It is generally believed that for a LED structure based on double injection into a quantum well layer, the electrons and holes must be confined in quantum wells constructed from the same constituent compound. To achieve this desired confinement, a heterostructure must be type-I with large valence and conduction band offsets. The $(\text{ZnSe})_m(\text{ZnTe})_n$ SLS's have already been shown by Wu *et al* (16,17) to be unsuitable candidates in the development of such optoelectronic devices because of their type-II band alignment. The common-anion rule of McCaldin *et al* (18), furthermore, indicates that the common-anion II-VI heterostructures would also be poor candidates because of their expected small valence band offsets. It is generally assumed that the $(\text{ZnSe})_m(\text{ZnS})_n$ SLS's form type-I superlattices and would, therefore, be viable candidates in the development of a blue LED. However, a transition to a type-II superlattice has been indicated by Kawakami *et al* (19) for the ZnSe (>40 Å) - ZnS (50 Å) SLS's and by Yamada *et al* (20-22) for a moderate level of applied hydrostatic pressure. Present studies indicate that for either type of band alignment the confinement of the holes in the ZnSe quantum wells is strong (i.e. a large conduction band offset), but the confinement of the electrons is weak (i.e. a small conduction band offset). Only in the work of Yamada *et al*, was there any suggestion that the electrons were localized. This suggested localization, however, would seem to contradict their conclusion of a small conduction band offset. Thus, the potential of these SLS's for use in the development of a blue LED remains in question.

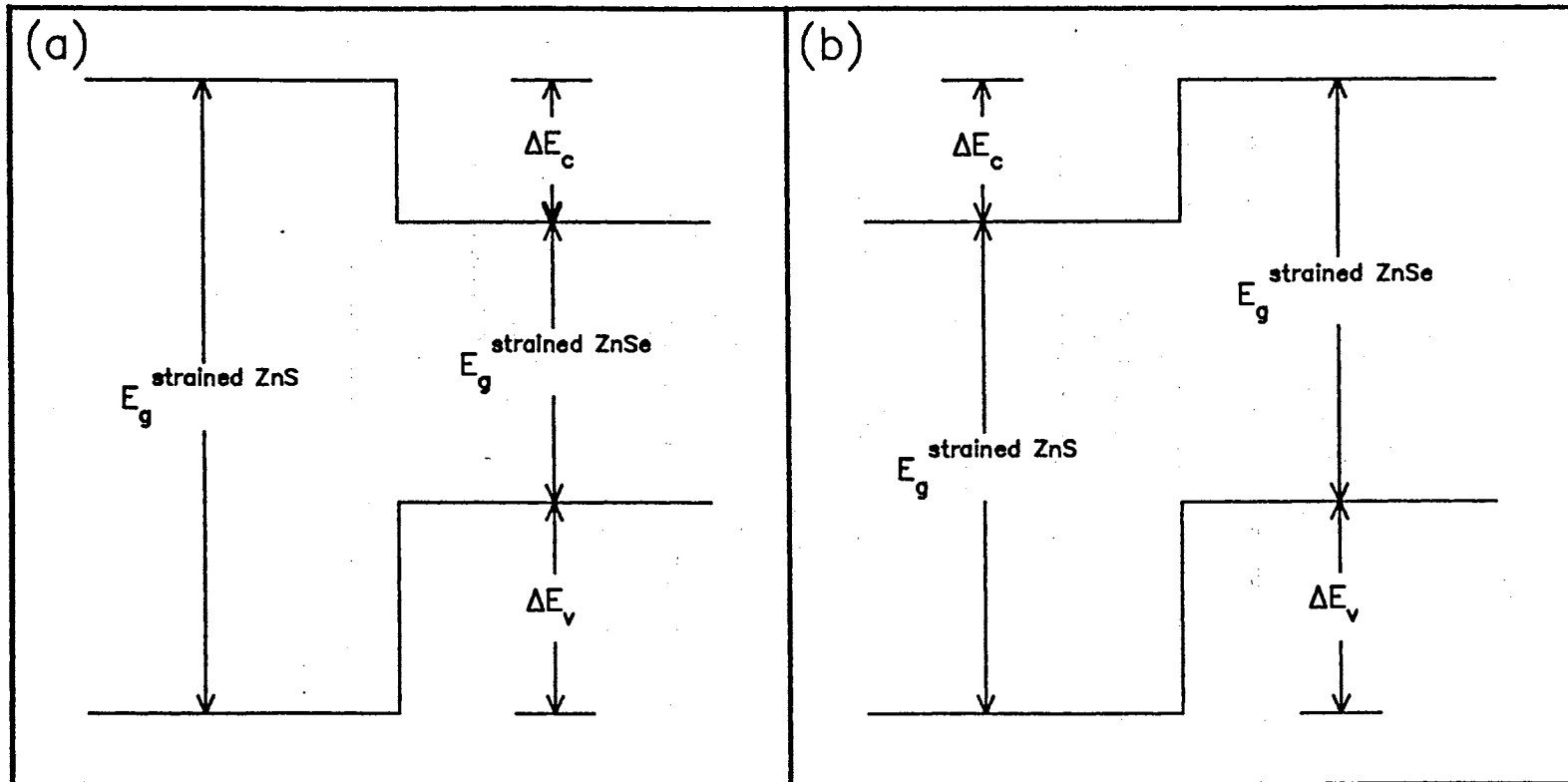


Figure 2. The band alignments for a type-I superlattice (a) and a type-II superlattice (b). For the type-I case, the strained ZnSe monolayers act as a quantum well for both the holes and electrons. For the type-II case, the strained ZnS monolayers assume the role of a quantum well for the electrons.

Photoluminescence and Absorption Studies

Medium- and long-period $(\text{ZnSe})_m(\text{ZnS})_n$ SLS's have been extensively studied through photoluminescence (PL) and absorption measurements by Kawakami *et al* (15,19), Yamada *et al* (3,20-22), Yokogawa *et al* (8,23), Teraguchi *et al* (10,11), Oniyama *et al* (12), Guan *et al* (24-26), Parbrook *et al* (27-31), Shen *et al* (32), and Kuwabara *et al* (33). In Figure 3, The PL and absorption spectra are shown for the ZnSe (20 Å) - ZnS (50 Å) SLS. The PL studies were performed with the GaAs substrate intact, while the absorption measurements were made only after the substrate was removed through chemical etching. When the substrate is removed, the SLS becomes free-standing and is subject to an entirely different elastic strain. Thus, any variation of the peak energies between the two measurements can be partially explained by the difference in the strain effects. From the PL spectrum, a blue emission line was observed and the peak was measured at higher energy than the emission peak from an undoped ZnSe film. Furthermore, the blue shift was observed in which the peak shifted towards higher energies as the number of ZnSe monolayers was decreased. This peak was attributed to a exciton, whose binding energy was increased by the confinement of the heavy-hole in the ZnSe quantum well. Through absorption measurements, the single PL exciton peak was resolved into two exciton peaks: the peak at the lower energy being attributed to the heavy-hole and the other to the light-hole. As the number of ZnSe monolayers was decreased, the separation between the two peaks was found to increase. Thus, both sets of studies indicate that the recombination of electron-hole pairs between the quantized levels in the ZnSe quantum wells was responsible for the observed blue luminescence. Furthermore, the blue shift is indicative that the band gap can be fine-tuned by varying the number of monolayers.

Local Density Functional Approximation

While the PL and absorption results suggest that the $(\text{ZnSe})_m(\text{ZnS})_n$ SLS's are viable candidates in the development of a blue LED, they also point out the need to gain an understanding of the electronic properties of these SLS's through theoretical studies. In semi-

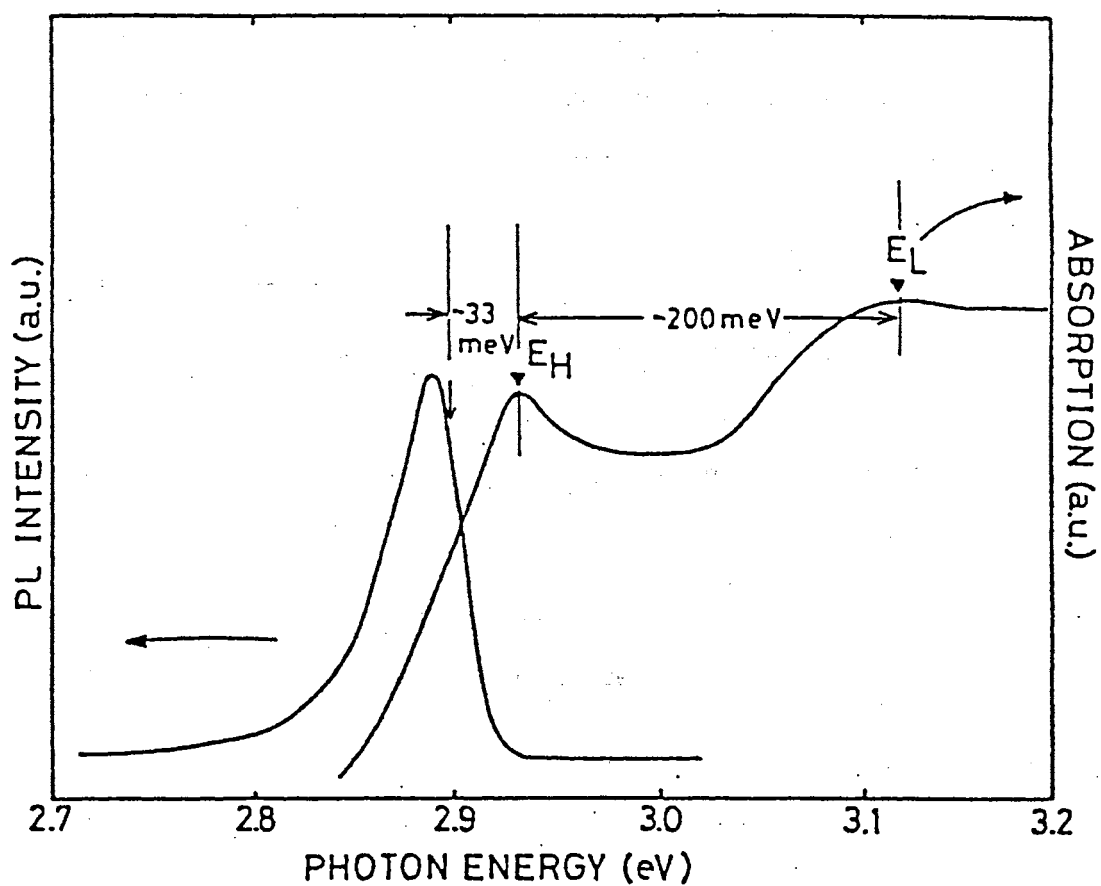


Figure 3. The photoluminescence and absorption spectra for the excitons attributed to the confined heavy- and light- holes at 4.2 K for the ZnSe (50 Å) - ZnS (20 Å) SLS Ref. (19).

empirical calculations, parameters of the energy matrix are fitted to existing experimental data. Since such data for the $(\text{ZnSe})_m(\text{ZnS})_n$ SLS's are not well established, the SLS parameters are fitted to the well known data of the bulk compounds instead. As a result, semi-empirical calculations cannot account for the interfacial region and are limited in their effectiveness. Thus, an accurate description of the electronic properties can only be derived from *ab initio* calculations. All *ab initio* electronic structure calculations involve determining the solution to the one-electron Schrödinger equation (in Rydbergs)

$$[-\nabla^2 + V_{\text{CRYST}}(\mathbf{r})]\psi_{\mu}(\mathbf{k}, \mathbf{r}) = E_{\mu}(\mathbf{k})\psi_{\mu}(\mathbf{k}, \mathbf{r}), \quad (1.1)$$

where $V_{\text{CRYST}}(\mathbf{r})$ is the crystalline potential, $\psi_{\mu}(\mathbf{k}, \mathbf{r})$ is the one-electron wave function, and $E_{\mu}(\mathbf{k})$ is the one-electron energy eigenvalue. In general, the crystalline potential is expressed as

$$V_{\text{CRYST}}(\mathbf{r}) = V_{\text{C}}(\mathbf{r}) + V_{\text{X}}(\mathbf{r}), \quad (1.2)$$

where the Coulomb potential $V_{\text{C}}(\mathbf{r})$ is the potential energy of an electron in a field of the nuclei and of all electrons (including itself) and the exchange potential $V_{\text{X}}(\mathbf{r})$ corrects for the fact that the electron does not act on itself. In principle, it is necessary to calculate a different exchange potential for each orbital. Since each exchange potential is determined by the sum of the exchange integrals, the number of which increases rapidly as the number of occupied orbitals increases, such a calculation would be impractical. Instead, the solution of Eq. (1.1) is generally determined from within the framework of the local density functional approximation (LDA), where $V_{\text{X}}(\mathbf{r})$ is replaced with an average exchange potential of a free-electron gas

$$V_{\text{X}}(\mathbf{r}) = -8F(\eta)[(3/8\pi)\rho(\mathbf{r})]^{1/3}. \quad (1.3)$$

In this approximation, $\rho(\mathbf{r})$ is the spherically averaged electronic charge density at the point \mathbf{r} and the function $F(\eta)$ is expressed as

$$F(\eta) = 1/2 + [(1-\eta^2)/4\eta]\ln|(1+\eta)/(1-\eta)|. \quad (1.4)$$

The variable η is given by $\eta = k/k_{\text{F}}$, where k^2 is the kinetic energy of a free-electron and k_{F}^2 is the Fermi energy. The three more common approximations made to Eq. (1.3) are the replacement of $F(\eta)$ with: i) its average value of 3/4 (when averaged over all of the occupied

states in a Fermi gas at absolute zero temperature) giving the Slater exchange potential (34)

$$V_{XS}(\mathbf{r}) = -6[(3/8\pi)\rho(\mathbf{r})]^{1/3}; \quad (1.5)$$

ii) its Fermi level value of $1/2$ giving the Kohn-Sham exchange potential (35)

$$V_{XKS}(\mathbf{r}) = -4[(3/8\pi)\rho(\mathbf{r})]^{1/3}; \quad (1.6)$$

and iii) $(3/4)\alpha$ (36,37) giving

$$V_{X\alpha}(\mathbf{r}) = -6\alpha[(3/8\pi)\rho(\mathbf{r})]^{1/3}, \quad (1.7)$$

where α is typically varied from $2/3$ to unity. A recent popular approximation is to use $V_{X\alpha}(\mathbf{r})$ along with the Ceperley-Alder correlation potential (38,39) for a unpolarized homogeneous electron gas (40). Although much more complicated than the other three, this approximation insures that the self-interaction is more effectively cancelled.

ab initio LCAO Calculations

The *ab initio* linear combination of atomic orbitals (LCAO) method has been shown capable of accurately predicting the electronic band structure and associated bulk properties of insulating, semiconducting, and metallic solids (41-53). More recently, the method has been extended to the study of surface states, complex crystals, and amorphous materials that require a large number of atoms per unit cell (54-63). These extensions are made possible by the fact that the LCAO method requires a relatively small number of basis functions per atom to accurately describe the electronic structure of a solid. As the number of atoms per unit cell increases, however, so does the size of the energy matrix. As a result, much computational time is needed for the evaluation of the energy matrix elements and the subsequent diagonalization of the matrix. Thus, there are practical limits present on the size of the problems that can be treated by this method.

One way to avoid these limitations has been to use alternative and somewhat more approximate methods, such as the linearized augmented plane-wave (LAPW) (64,65) and the linear combination of muffin-tin orbitals (LMTO) (66) methods. The recent development of the *ab initio* factorized LCAO (FLCAO) method of Lafon (67), though, has greatly increased the size

of the problems that can now be studied. The strength of this method is that for crystals having cubic, tetragonal or orthorhombic symmetry or those which can be forced to assume such symmetry by simply constructing a larger unit cell, the factorization of the energy matrix elements into x-, y-, and z-components effectively reduces the lattice sum over unit cells from a N^3 problem down to a $3N$ problem. Thus, by use of this factorization scheme, one of the computational burdens has been eliminated.

To date, the *ab initio* nonself-consistent FLCAO method has been used to determine the electronic structure of bulk copper (1 atom per unit cell) and a (001) copper surface (33 atoms per unit cell) (67); α -quartz (9 and 18 atoms per unit cell) and quartz with an oxygen vacancy (72 atoms per unit cell) (68); berlinite (18 atoms per unit cell) (69); and of bulk ZnSe and ZnS (2 and 4 atoms per unit cell) (70). Because of the success of these calculations, the FLCAO method has been used to determine the electronic structure of the (001) free-standing short- to medium-period $(\text{ZnSe})_m(\text{ZnS})_n$ SLS's. The objective of this work is three-fold: i) to calculate the electronic band structures and study the dependency of the band gap energy on the set of $\{m,n\}$ values, ii) to determine if any localization of the heavy-hole, light-hole, and lower conduction states occurs, and iii) to calculate the size of the valence- and conduction-band offsets. From these results, an evaluation of the $(\text{ZnSe})_m(\text{ZnS})_n$ SLS's as potential candidates in the development of a blue LED will be made.

CHAPTER II

THE FLCAO FORMULATION

Introduction

Every crystal has two lattices associated with it, the crystal lattice and the reciprocal lattice. The periodicity of the crystal lattice is represented by a unit cell constructed from the three lattice vectors \mathbf{A}_1 , \mathbf{A}_2 , and \mathbf{A}_3 , which define the symmetry of the unit cell. The lattice translation vector connecting the origin of the central unit cell to the origin of all other unit cells in the crystal is given by

$$\mathbf{R}_V = v_1 \mathbf{A}_1 + v_2 \mathbf{A}_2 + v_3 \mathbf{A}_3, \quad (2.1)$$

where v_1 , v_2 , and v_3 are integers. The position of the j th atom in the central unit cell is given by the vector \mathbf{t}_j , so that the vector connecting the origin of the central unit cell to any equivalent lattice site in the crystal is given by $\mathbf{R}_V + \mathbf{t}_j$. The axis vectors of the reciprocal lattice are given by

$$\mathbf{b}_1 = 2\pi(\mathbf{A}_2 \times \mathbf{A}_3)/\Omega, \quad \mathbf{b}_2 = 2\pi(\mathbf{A}_3 \times \mathbf{A}_1)/\Omega, \quad \text{and} \quad \mathbf{b}_3 = 2\pi(\mathbf{A}_1 \times \mathbf{A}_2)/\Omega; \quad (2.2)$$

where $\Omega = \mathbf{A}_1 \cdot \mathbf{A}_2 \times \mathbf{A}_3$ is the volume of the unit cell. The reciprocal lattice vector is then expressed as

$$\mathbf{K}_\mu = \mu_1 \mathbf{b}_1 + \mu_2 \mathbf{b}_2 + \mu_3 \mathbf{b}_3, \quad (2.3)$$

where μ_1 , μ_2 , and μ_3 are integers. Furthermore, any point in the first Brillouin zone of reciprocal space may be expressed by the wave vector

$$\mathbf{k} = k_1 \mathbf{b}_1 + k_2 \mathbf{b}_2 + k_3 \mathbf{b}_3, \quad (2.4)$$

where k_1 , k_2 , and k_3 can assume values from zero to unity.

In past *ab initio* LCAO calculations, much CPU time has been expended in the construction of the energy matrix, which requires the evaluation of numerous multi-center integrals. Consider the expression

$$f = \sum_{v_1} \sum_{v_2} \sum_{v_3} \exp\{i\mathbf{k} \cdot \mathbf{R}_v\} F(\mathbf{r} - \mathbf{R}_v), \quad (2.5)$$

where the function $F(\mathbf{r} - \mathbf{R}_v)$ can be factorized into x-, y-, and z-components irrespective of the unit cell's symmetry. The evaluation of this expression, as is, would be a N^3 problem because of the lattice sum over unit cells. In the FLCAO formulation of Lafon (67), though, this expression can be reduced down to a $3N$ problem should the unit cell have some form of rectangular symmetry: cubic, tetragonal or orthorhombic. For such symmetry, the lattice translation vector would be expressed as

$$\mathbf{R}_v = v_1 a_x \hat{\mathbf{x}} + v_2 a_y \hat{\mathbf{y}} + v_3 a_z \hat{\mathbf{z}} \quad (2.6)$$

and the wave vector would be expressed as

$$\mathbf{k} = (2\pi / a_x) k_1 \hat{\mathbf{x}} + (2\pi / a_y) k_2 \hat{\mathbf{y}} + (2\pi / a_z) k_3 \hat{\mathbf{z}} \quad (2.7)$$

so that the dot product of these two vectors is

$$\mathbf{k} \cdot \mathbf{R}_v = 2\pi k_1 v_1 + 2\pi k_2 v_2 + 2\pi k_3 v_3. \quad (2.8)$$

The expression in Eq. (2.5) can now be easily factorized into x-, y-, and z-components to yield

$$f = \left[\sum_{v_1} \exp\{i2\pi k_1 v_1\} F(x - v_1 a_x) \right] \times \left[\sum_{v_2} \exp\{i2\pi k_2 v_2\} F(y - v_2 a_y) \right] \left[\sum_{v_3} \exp\{i2\pi k_3 v_3\} F(z - v_3 a_z) \right], \quad (2.9)$$

which is the simpler $3N$ problem. Use of this factorization process typically results in a significant (>50%) CPU time savings for the construction of the energy matrix. If the primitive unit does not have rectangular symmetry, then it may be forced to assume such symmetry by simply constructing a larger non-primitive unit cell. One should note, however, that the consequence of increasing the number of atoms in the unit cell results is an increase in the size of the energy matrix. Thus, the CPU time saved factorizing the energy matrix elements into x-, y-, and z-components could be easily spent on the evaluation of the energy matrix.

The Energy Matrix

In the FLCAO formulation, the one-electron energy eigenvalues and wave functions are determined from

$$[-\nabla^2 + V_{\text{CRYST}}(\mathbf{r})]\psi_a(\mathbf{k}, \mathbf{r}) = E_a(\mathbf{k})\psi_a(\mathbf{k}, \mathbf{r}), \quad (2.10)$$

where the effective crystalline potential exhibits the periodicity of the lattice

$$V_{\text{CRYST}}(\mathbf{r} + \mathbf{R}_\nu) = V_{\text{CRYST}}(\mathbf{r}). \quad (2.11)$$

The one-electron wave functions are constructed from an expansion of basis functions

$$\psi_a(\mathbf{k}, \mathbf{r}) = \sum_j \sum_{n\ell m} C_{j,a}^{n\ell m}(\mathbf{k}) \Phi_{n\ell m}^j(\mathbf{k}, \mathbf{r}), \quad (2.12)$$

where the sum over j involves all atoms in the unit cell and the sum over $n\ell m$ is over all orbitals.

In its present form, the FLCAO code treats electronic configurations having open shells in the same manner as configurations with closed shells so that the same one-electron wave function will be assigned to both set of spins. Substitution of this expression into Eq. (2.10) gives

$$\sum_j \sum_{n\ell m} C_{j,a}^{n\ell m}(\mathbf{k}) [-(1/2)\nabla^2 + V_{\text{CRYST}}(\mathbf{r})] \Phi_{n\ell m}^j(\mathbf{k}, \mathbf{r}) = E_a(\mathbf{k}) \sum_j \sum_{n\ell m} C_{j,a}^{n\ell m}(\mathbf{k}) \Phi_{n\ell m}^j(\mathbf{k}, \mathbf{r}). \quad (2.13)$$

Multiplying both sides by $\Phi_{n'\ell'm'}^j(\mathbf{k}, \mathbf{r})^*$ and performing a spatial integration yields

$$\begin{aligned} \sum_j \sum_{n\ell m} C_{j,a}^{n\ell m}(\mathbf{k}) [-(1/2) \int \Phi_{n'\ell'm'}^j(\mathbf{k}, \mathbf{r})^* \nabla^2 \Phi_{n\ell m}^j(\mathbf{k}, \mathbf{r}) d\tau + \int \Phi_{n'\ell'm'}^j(\mathbf{k}, \mathbf{r})^* V_{\text{CRYST}}(\mathbf{r}) \Phi_{n\ell m}^j(\mathbf{k}, \mathbf{r}) d\tau \\ - E_a(\mathbf{k}) \int \Phi_{n'\ell'm'}^j(\mathbf{k}, \mathbf{r})^* \Phi_{n\ell m}^j(\mathbf{k}, \mathbf{r}) d\tau] = 0. \end{aligned} \quad (2.14)$$

Each basis function is then constructed from an expansion of Bloch functions (70,71)

$$\Phi_{n\ell m}^j(\mathbf{k}, \mathbf{r}) = \sum_i d_{n\ell m}^j(\alpha_i) b_{n\ell m}^j(\alpha_i, \mathbf{k}, \mathbf{r}). \quad (2.15)$$

Each Bloch function, in turn, is constructed from a lattice sum involving a single atomic orbital

$$b_{n\ell m}^j(\alpha_i, \mathbf{k}, \mathbf{r}) = N^{-1/2} \sum_{\nu} \exp\{i\mathbf{k} \cdot \mathbf{R}_\nu\} \chi_{n\ell m}[\alpha_i, \mathbf{r} - (\mathbf{R}_\nu + \mathbf{t}_j)], \quad (2.16)$$

where N represents the total number of unit cells in the crystal. Using this notation, the basis functions may now be expressed as

$$\Phi_{n\ell m}^j(\mathbf{k}, \mathbf{r}) = N^{-1/2} \sum_i d_{n\ell m}^j(\alpha_i) \sum_{\nu} \exp\{i\mathbf{k} \cdot \mathbf{R}_\nu\} \chi_{n\ell m}[\alpha_i, \mathbf{r} - (\mathbf{R}_\nu + \mathbf{t}_j)]. \quad (2.17)$$

Using this expression in Eq. (2.14) yields

$$\begin{aligned} \sum_j \sum_{n\ell m} C_{j,a}^{n\ell m}(\mathbf{k}) & \left[-\frac{1}{2} \sum_i \sum_i d_{n'\ell'm'}^j(\alpha_i) d_{n\ell m}^j(\alpha_i) \sum_V \exp\{i\mathbf{k} \cdot \mathbf{R}_V\} \int \chi_{n'\ell'm'}(\alpha_i, \mathbf{r}_A) \nabla^2 \chi_{n\ell m}(\alpha_i, \mathbf{r}_B) d\tau \right. \\ & + \sum_i \sum_i d_{n'\ell'm'}^j(\alpha_i) d_{n\ell m}^j(\alpha_i) \sum_V \exp\{i\mathbf{k} \cdot \mathbf{R}_V\} \int \chi_{n'\ell'm'}(\alpha_i, \mathbf{r}_A) V_{\text{CRYST}}(\mathbf{r}) \chi_{n\ell m}(\alpha_i, \mathbf{r}_B) d\tau \\ & \left. - E_a(\mathbf{k}) \sum_i \sum_i d_{n'\ell'm'}^j(\alpha_i) d_{n\ell m}^j(\alpha_i) \sum_V \exp\{i\mathbf{k} \cdot \mathbf{R}_V\} \int \chi_{n'\ell'm'}(\alpha_i, \mathbf{r}_A) \chi_{n\ell m}(\alpha_i, \mathbf{r}_B) d\tau \right] = 0, \quad (2.18) \end{aligned}$$

where $\mathbf{r}_A = \mathbf{r} - \mathbf{t}_j = \mathbf{r} - \mathbf{A}$ and $\mathbf{r}_B = \mathbf{r} - (\mathbf{R}_V + \mathbf{t}_j) = \mathbf{r} - \mathbf{B}$. The three terms in the brackets each represent a single element of, respectively, the kinetic energy matrix \mathbf{T} , the potential energy matrix \mathbf{V} , and the overlap matrix \mathbf{S} . Furthermore, the off-diagonal overlap matrix elements are generally non-vanishing since there are no orthogonality constraints placed on the atomic orbitals. Thus, without loss of generality, the energy matrix for a specified \mathbf{k} -point in reciprocal space can be easily derived from the above expression and written as

$$(\mathbf{T} + \mathbf{V} - E\mathbf{S})\mathbf{C} = 0. \quad (2.19)$$

For N number of basis functions; \mathbf{T} , \mathbf{V} , and \mathbf{S} are $N \times N$ square matrices and the one-electron wave function coefficient matrix \mathbf{C} is a N column matrix. For an independent set of wave function coefficients to exist, the determinant of the energy matrix must be vanishing

$$|\mathbf{T} + \mathbf{V} - E\mathbf{S}| = 0. \quad (2.20)$$

From this determinant, the one-electron energy eigenvalues and then the corresponding one-electron wavefunction coefficients are determined from Eq. (2.19). As was mentioned in the previous chapter, the major constraint to electronic structure calculations is the size of the energy matrix. While the number of atomic orbitals used in these calculations can be rather large, the number of basis functions should be minimal.

The Atomic Orbitals

The atomic orbitals are expressed as the products of radial wave and spherical harmonic functions

$$\chi_{NLM_L}(\alpha, r) = R_{NL}(\alpha, r)Y_{LM_L}(\theta, \phi), \quad (2.21)$$

where N is the principal quantum number, L is the orbital quantum number and M_L is the magnetic quantum number (72). The spherical harmonic function is given by

$$Y_{L,M_L}(\theta, \phi) = \sqrt{\frac{2L+1}{4\pi} \frac{(L-M_L)!}{(L+M_L)!}} P_L^{M_L}(\cos\theta) \exp\{iM_L\phi\}, \quad (2.22)$$

where the expression for the associated Legendre function is

$$P_L^{M_L}(x) = \frac{(-1)^{M_L}}{2^L L!} (1-x^2)^{M_L/2} \frac{d^{L+M_L}}{dx^{L+M_L}} (x^2-1)^L. \quad (2.23)$$

In the purest form of a LCAO calculation, the atomic orbitals would be represented by Slater-type orbitals (STO's) having the form

$$\chi_{NLM_L}(\alpha, r) = r^{(N-1)} \exp\{-\alpha r\} Y_{LM_L}(\theta, \phi). \quad (2.24)$$

In the past, STO's were popular because they were known to correctly describe the qualitative features of molecular orbitals. Evaluation of the multi-center integrals in Eq. (2.18) using STO's would be, however, difficult and time consuming. Instead, the atomic orbitals are represented by Gaussian-type orbitals (GTO's) having the form

$$\chi_{NLM_L}(\alpha, r) = r^{2(N-1)} \exp\{-\alpha r^2\} Y_{LM_L}(\theta, \phi), \quad (2.25)$$

which allows for the easy evaluation of the multi-center integrals. As with most electronic structure calculations involving GTO's, the FLCAO formulation only uses the angular functions with $L = (N-1)$ (i.e. only the 1s, 2p, 3d, ... atomic orbitals are explicitly used). With such a constraint, the GTO's can now be expressed in terms of real harmonics as

$$\chi_{n\ell m}(\alpha, r) = x^n y^\ell z^m \exp\{-\alpha r^2\}. \quad (2.26)$$

As a result, the representation for an s-orbital ($n + \ell + m = 0$) is given by

$$\chi_s(\alpha, r) = \exp\{-\alpha r^2\}. \quad (2.27)$$

For a p-orbital ($n + \ell + m = 1$), there are three possible representations

$$\chi_p = x \exp\{-\alpha r^2\}, \quad y \exp\{-\alpha r^2\}, \quad \text{and} \quad z \exp\{-\alpha r^2\}. \quad (2.28)$$

And for a d-orbital ($n + \ell + m = 2$), there are six possible representations

$$\begin{aligned} \chi_d = & x^2 \exp\{-\alpha r^2\}, \quad y^2 \exp\{-\alpha r^2\}, \quad z^2 \exp\{-\alpha r^2\}, \\ & xy \exp\{-\alpha r^2\}, \quad xz \exp\{-\alpha r^2\}, \quad \text{and} \quad yz \exp\{-\alpha r^2\}. \end{aligned} \quad (2.29)$$

In general, the orbital coefficients and the expansion coefficients of Eq. (2.15) are obtained from Gaussian basis sets constructed for use in *ab initio* molecular calculations (72,73). In the event that additional atomic orbitals need to be added to the basis, then the expansion coefficients will have to be redetermined through some contraction procedure. The procedure used in this work will be presented in the next chapter.

The Crystalline Potential

The crystalline potential in Eq. (2.10) is first numerically calculated for a specified grid within the unit cell from the superposition of self-consistent spherically-symmetric atomic charge densities. It is assumed that the exchange potential can be adequately described by the LDA of Eq (1.7). The atomic charge densities are calculated using a modified Herman-Skillman formulation (74), which is an iterative technique used to obtain self-consistent solutions of the non-relativistic Hartree-Fock equations (75) for free atoms and ions. Using the expression for the atomic orbital in Eq. (2.21), the three-dimensional spatial Hartree-Fock wave equations are reduced down to one-dimensional radial wave equations

$$\left[-d^2 / dr^2 + L(L + 1) / r^2 + V(r)\right]P_{NL}(r) = E_{NL}P_{NL}(r), \quad (2.30)$$

where $P_{NL}(r) = rR_{NL}(r)$ are the normalized radial wave functions and the expression for the

potential is given by

$$V(r) = V_C(r) + V_{X\alpha}(r) \\ = -2Z/r - 8\pi r \int_0^r \rho(t) dt - 8\pi r^2 \int_r^\infty [\rho(t)/t] dt - 6\alpha [(3/8\pi)\rho(r)]^{1/3}. \quad (2.31)$$

The iteration scheme used to obtain self-consistency is as follows. At the start of the m th iteration, it is assumed that $V^{mi}(r)$, E_{NL}^{mi} , and $P_{NL}^{mi}(r)$ are known. The initial potential $V^{mi}(r)$ is inserted into the radial wave equation, and this is solved for all orbitals NL to obtain the final one-electron energy eigenvalues E_{NL}^{mf} and radial wave functions $P_{NL}^{mf}(r)$. For the energy eigenvalues, E_{NL}^{mf} will equal the sum of E_{NL}^{mi} and a first order perturbation correction term. The final spherically-symmetric electronic charge density $\rho^{mf}(r)$ is then calculated from

$$\rho^{mf}(r) = -(4\pi r^2) \sum_{NL} \omega_{NL} [P_{NL}^{mf}(r)]^2, \quad (2.32)$$

where ω_{NL} is the occupation number for the orbital NL. The final potential $V^{mf}(r)$ is then calculated from Eq. (2.31). If the self-consistency criteria is not met, then the initial potential for the next iteration can be obtained by the arithmetic average scheme

$$V^{(m+1)i}(r) = (1/2)[V^{mi}(r) + V^{mf}(r)] \quad (2.33)$$

or the Pratt improvement scheme

$$V^{(m+1)i}(r) = \frac{V^{(m-1)i}(r) \cdot V^{mf}(r) - V^{mi}(r) \cdot V^{(m-1)f}(r)}{V^{(m-1)i}(r) + V^{mf}(r) - V^{mi}(r) - V^{(m-1)f}(r)} \quad (2.34)$$

or, as is typically done, by the incorporation of both schemes. The trial energy eigenvalue for the next iteration is obtained from first order perturbation theory

$$E_{NL}^{(m+1)i} = E_{NL}^{mf} + \int_0^\infty [P_{NL}^{mf}(r)]^2 [V^{(m+1)i}(r) - V^{mi}(r)] dr. \quad (2.35)$$

As can be seen from Eq. (2.31) for a neutral atom, however, the LDA breaks down at large distances from the nucleus. For sufficiently large values of r , the three Coulomb potential terms cancel each other out. Furthermore, the electronic charge density and, therefore, the exchange potential approach zero for large values of r . This, however, is incorrect. Since an electron

cannot self-interact, it must move in the field of a singly charged positive ion at large values of r . Therefore, $V(r)$ must approach $-2/r$ and not zero for large values of r . In the Herman-Skillman formulation, the Latter cutoff potential can be utilized to insure the correct asymptotic behavior for large r . The corrected Herman-Skillman potential to be used in Eq. (2.30) would then be expressed as

$$V(r) = \begin{cases} V_C(r) + V_{X\alpha}(r) & , r < r_0 \\ -2(Z - N + 1) / r & , r \geq r_0 \end{cases} \quad (2.36)$$

where $Z-N$ is the ionicity and the value of r_0 is obtained from

$$V_C(r_0) + V_{X\alpha}(r_0) = -2(Z - N + 1)/r_0. \quad (2.37)$$

The Latter cutoff potential is rarely used today because the derivative $dV(r)/dr$ is discontinuous at $r = r_0$.

After the crystalline has been numerically calculated, it is then fitted into the following analytic expression

$$V_{\text{CRYST}}(r) = \sum_V \sum_j [V_j^c(r - [\mathbf{R}_V + \mathbf{t}_j]) + V_j^g(r - [\mathbf{R}_V + \mathbf{t}_j])] + V^k(r); \quad (2.38)$$

where

$$V_j^c(r) = -Z_j \exp\{-\beta_0^j r^2\} / r, \quad (2.39)$$

$$V_j^g(r) = \sum_i \sigma_i^j \exp\{-\beta_i^j r^2\}, \quad (2.40)$$

and

$$V^k(r) = \sum_{\mu} U_{\mu}^k(\mathbf{C}) \exp\{i\mathbf{K}_{\mu} \cdot (\mathbf{r} - \mathbf{C})\}. \quad (2.41)$$

In the $V^k(r)$ term, the vector \mathbf{C} connects the origin to some arbitrary point in the lattice about which the Fourier series is expanded. The purpose of this term is to serve as the correction to the initial crystalline potential in the interatomic region during the self-consistency process. Thus, for nonself-consistent calculations, the Fourier contribution is ignored.

The purpose of the $V_j^c(\mathbf{r})$ term is to reproduce the Coulombic singularity. The integrals involving this term, however, cannot be factorized. The $V_j^g(\mathbf{r})$ term is an expansion of s-like GTO's, which were chosen to ease the burden of the multi-center integrals and are certainly amenable to factorization. Together, the $V_j^c(\mathbf{r})$ and $V_j^g(\mathbf{r})$ terms can be viewed as an analytic atomic-centered potential (ACP), displaying much the same behavior as an atomic potential in the region close to the nucleus. The values for the linear (σ_i^j 's) and non-linear (β_i^j 's) coefficients of the ACP's are determined through a non-linear least-squares (NLLS) fit.

The fit to the crystalline potential is not unique. In fact, any initial guess to the β_i^j 's will lead to a fit. The quality of the fit, however, depends on the quality of the initial guess. For nonself-consistent calculations, the accuracy of the electronic structure calculation is dependent on the accuracy of the crystalline potential fit. The β_i^j 's in the $V_j^g(\mathbf{r})$ term are chosen to be even-tempered (76), so that for each ACP at the j th atomic site in the unit cell

$$\beta_i^j = [\text{RATIO}(j)]^{i-1} \beta_1^j. \quad (2.42)$$

A precise scientific method for determining a reasonable fit to the crystalline potential has not yet been developed (77). The approach taken in this work is as follows. Initially, guesses for the $\text{RATIO}(j)$'s and β_1^j 's were made. The remaining β_i^j 's were then determined from the above equation. During the NLLS fit, though, the even-temperment constraint was not enforced so that the β_i^j 's (including the β_0^j 's of the $V_j^c(\mathbf{r})$ term) were varied independent of each other. As a result of this flexibility, the root-mean-square error approached its optimal value after a few iterations and deviated from this value only slightly during subsequent iterations. However, the consequence of not using the even temperament constraint was that the fit would not converge. The next step was then the select a set of β_i^j 's from one of the iterations and construct the ratios from

$$\text{RATIO}(j) = (\beta_n^j / \beta_1^j)^{-1/(n-1)} \quad (2.43)$$

so that a new set of even-tempered β_i^j 's could be constructed. Using this set as the initial

guesses, a NLLS fit, subject to the even-temperment constraint, was performed until the convergence criteria was met.

The Overlap Matrix Elements

From Eq. (2.18), the elements of the overlap matrix which need to be evaluated are expressed as

$$S_{n_1 \ell_1 m_1, n_2 \ell_2 m_2}(\alpha_{i_1}, \alpha_{i_2}, \mathbf{A}, \mathbf{B}) = \sum_{i_2} \sum_{i_1} d_{n_1 \ell_1 m_1}^{i_1}(\alpha_{i_1}) d_{n_2 \ell_2 m_2}^{i_2}(\alpha_{i_2}) \sum_{\mathbf{v}} \exp\{i\mathbf{k} \cdot \mathbf{R}_{\mathbf{v}}\} \int \chi_{n_1 \ell_1 m_1}^{i_1}(\alpha_{i_1}, \mathbf{r}_A) \chi_{n_2 \ell_2 m_2}^{i_2}(\alpha_{i_2}, \mathbf{r}_B) d\tau. \quad (2.44)$$

Using the factorization of the GTO's, these elements can be written as

$$S_{n_1 \ell_1 m_1, n_2 \ell_2 m_2}(\alpha_{i_1}, \alpha_{i_2}, \mathbf{A}, \mathbf{B}) = \sum_{\mathbf{v}} \exp\{i\mathbf{k} \cdot \mathbf{R}_{\mathbf{v}}\} S_{n_1, n_2}(\alpha_{i_1}, \alpha_{i_2}, \mathbf{A}_x, \mathbf{B}_x) S_{\ell_1, \ell_2}(\alpha_{i_1}, \alpha_{i_2}, \mathbf{A}_y, \mathbf{B}_y) S_{m_1, m_2}(\alpha_{i_1}, \alpha_{i_2}, \mathbf{A}_z, \mathbf{B}_z), \quad (2.45)$$

where the term involving the x-components has the form

$$S_{n_1, n_2}(\alpha_{i_1}, \alpha_{i_2}, \mathbf{A}_x, \mathbf{B}_x) = \int x^{n_1 + n_2} \exp\{-\alpha_{i_1} x_A^2 - \alpha_{i_2} x_B^2\} dx. \quad (2.46)$$

Evaluation of this two-center integral yields

$$S_{n_1, n_2}(\alpha_{i_1}, \alpha_{i_2}, \mathbf{A}_x, \mathbf{B}_x) = \exp\{-H(\mathbf{AB})_x^2\} \sum_{r_1} \binom{n_1}{r_1} (\mathbf{AD})_x^{n_1 - r_1} \sum_{r_2} \binom{n_2}{r_2} (\mathbf{BD})_x^{n_2 - r_2} E_{r_1 + r_2}(\beta), \quad (2.47)$$

where $\beta = \alpha_{i_1} + \alpha_{i_2}$, $H = \alpha_{i_1} \alpha_{i_2} / \beta$, $D_x = (\alpha_{i_1} A_x + \alpha_{i_2} B_x) / \beta$, $(\mathbf{AD})_x = D_x - A_x$, and $(\mathbf{BD})_x = D_x - B_x$. The last term of the product is given by the expression

$$E_n(\beta) = N_n \beta^{-(n+1)/2}, \quad (2.48)$$

where

$$N_n = \begin{cases} 0 & , n = \text{odd} \\ (n-1)!! / 2^{n/2} & , n = \text{even} \\ 1 & , n = \text{zero} \end{cases}$$

(2.49) If the unit cell has rectangular symmetry, then the elements of the overlap matrix can be reduced to the following 3N problems

$$\begin{aligned} S_{n_1 \ell_1 m_1, n_2 \ell_2 m_2}(\alpha_{i_1}, \alpha_{i_2}, \mathbf{A}, \mathbf{B}) = \\ \sum_{i_2} \sum_{i_1} d_{n_1 \ell_1 m_1}^{i_1}(\alpha_{i_1}) d_{n_2 \ell_2 m_2}^{i_2}(\alpha_{i_2}) \left[\sum_{v_1} \exp\{i2\pi k_x v_1\} S_{n_1, n_2}(\alpha_{i_1}, \alpha_{i_2}, A_x, B_x) \right] \\ \times \left[\sum_{v_2} \exp\{i2\pi k_y v_2\} S_{\ell_1, \ell_2}(\alpha_{i_1}, \alpha_{i_2}, A_y, B_y) \right] \left[\sum_{v_3} \exp\{i2\pi k_z v_3\} S_{m_1, m_2}(\alpha_{i_1}, \alpha_{i_2}, A_z, B_z) \right]. \end{aligned} \quad (2.50)$$

The Kinetic Energy Matrix Elements

From Eq. (2.18), the elements of the kinetic energy matrix which need to be evaluated are expressed as

$$\begin{aligned} T_{n_1 \ell_1 m_1, n_2 \ell_2 m_2}(\alpha_{i_1}, \alpha_{i_2}, \mathbf{A}, \mathbf{B}) = \\ -(1/2) \sum_{i_2} \sum_{i_1} d_{n_1 \ell_1 m_1}^{i_1}(\alpha_{i_1}) d_{n_2 \ell_2 m_2}^{i_2}(\alpha_{i_2}) \sum_v \exp\{i\mathbf{k} \cdot \mathbf{R}_v\} \int \chi_{n_1 \ell_1 m_1}^{i_1}(\alpha_{i_1}, \mathbf{r}_A) \nabla^2 \chi_{n_2 \ell_2 m_2}^{i_2}(\alpha_{i_2}, \mathbf{r}_B) d\tau. \end{aligned} \quad (2.51)$$

In similar fashion to the overlap matrix elements, these elements can be factorized and written as

$$\begin{aligned} T_{n_1 \ell_1 m_1, n_2 \ell_2 m_2}(\alpha_{i_1}, \alpha_{i_2}, \mathbf{A}, \mathbf{B}) = -(1/2) \sum_{i_2} \sum_{i_1} d_{n_1 \ell_1 m_1}^{i_1}(\alpha_{i_1}) d_{n_2 \ell_2 m_2}^{i_2}(\alpha_{i_2}) \sum_v \exp\{i\mathbf{k} \cdot \mathbf{R}_v\} \\ \times \left(T_{n_1, n_2}(\alpha_{i_1}, \alpha_{i_2}, A_x, B_x) S_{\ell_1, \ell_2}(\alpha_{i_1}, \alpha_{i_2}, A_y, B_y) S_{m_1, m_2}(\alpha_{i_1}, \alpha_{i_2}, A_z, B_z) \right. \\ \left. + S_{n_1, n_2}(\alpha_{i_1}, \alpha_{i_2}, A_x, B_x) T_{\ell_1, \ell_2}(\alpha_{i_1}, \alpha_{i_2}, A_y, B_y) S_{m_1, m_2}(\alpha_{i_1}, \alpha_{i_2}, A_z, B_z) \right. \\ \left. + S_{n_1, n_2}(\alpha_{i_1}, \alpha_{i_2}, A_x, B_x) S_{\ell_1, \ell_2}(\alpha_{i_1}, \alpha_{i_2}, A_y, B_y) T_{m_1, m_2}(\alpha_{i_1}, \alpha_{i_2}, A_z, B_z) \right). \end{aligned} \quad (2.52)$$

The first term of the first product is expressed as

$$T_{n_1, n_2}(\alpha_{i_1}, \alpha_{i_2}, A_x, B_x) = \int [n_2(n_2 - 1)x^{-2} - 4\alpha_{i_2} x_B n_2 x^{-1} + 2\alpha_{i_2} (2\alpha_{i_2} x_B^2 - 1)] x^{n_1+n_2} \exp\{-\alpha_{i_1} x_A^2 - \alpha_{i_2} x_B^2\} dx \quad (2.53)$$

and the evaluation of this two-center integral yields

$$T_{n_1, n_2}(\alpha_{i_1}, \alpha_{i_2}, A_x, B_x) = n_2(n_2 - 1)S_{n_1, n_2-2}(\alpha_{i_1}, \alpha_{i_2}, A_x, B_x) - 2\alpha_{i_2} (2n_2 + 1)S_{n_1, n_2}(\alpha_{i_1}, \alpha_{i_2}, A_x, B_x) + 4\alpha_{i_2}^2 S_{n_1, n_2+2}(\alpha_{i_1}, \alpha_{i_2}, A_x, B_x). \quad (2.54)$$

A reduction down to a 3N problem also occurs for the kinetic energy matrix elements if the unit cell has rectangular symmetry

$$\begin{aligned} T_{n_1 \ell_1 m_1, n_2 \ell_2 m_2}(\alpha_{i_1}, \alpha_{i_2}, \mathbf{A}, \mathbf{B}) = & - (1/2) \sum_{i_2} \sum_{i_1} d_{n_1 \ell_1 m_1}^{i_1}(\alpha_{i_1}) d_{n_2 \ell_2 m_2}^{i_2}(\alpha_{i_2}) \left(\left[\sum_{v_1} \exp\{i2\pi k_x v_1\} T_{n_1, n_2}(\alpha_{i_1}, \alpha_{i_2}, A_x, B_x) \right] \right. \\ & \times \left[\sum_{v_2} \exp\{i2\pi k_y v_2\} S_{\ell_1, \ell_2}(\alpha_{i_1}, \alpha_{i_2}, A_y, B_y) \right] \left[\sum_{v_3} \exp\{i2\pi k_z v_3\} S_{m_1, m_2}(\alpha_{i_1}, \alpha_{i_2}, A_z, B_z) \right] \\ & + \left[\sum_{v_1} \exp\{i2\pi k_x v_1\} S_{n_1, n_2}(\alpha_{i_1}, \alpha_{i_2}, A_x, B_x) \right] \left[\sum_{v_2} \exp\{i2\pi k_y v_2\} T_{\ell_1, \ell_2}(\alpha_{i_1}, \alpha_{i_2}, A_y, B_y) \right] \\ & \times \left[\sum_{v_3} \exp\{i2\pi k_z v_3\} S_{m_1, m_2}(\alpha_{i_1}, \alpha_{i_2}, A_z, B_z) \right] + \left[\sum_{v_1} \exp\{i2\pi k_x v_1\} S_{n_1, n_2}(\alpha_{i_1}, \alpha_{i_2}, A_x, B_x) \right] \\ & \times \left. \left[\sum_{v_2} \exp\{i2\pi k_y v_2\} S_{\ell_1, \ell_2}(\alpha_{i_1}, \alpha_{i_2}, A_y, B_y) \right] \left[\sum_{v_3} \exp\{i2\pi k_z v_3\} T_{m_1, m_2}(\alpha_{i_1}, \alpha_{i_2}, A_z, B_z) \right] \right). \quad (2.55) \end{aligned}$$

The Potential Energy Matrix Elements

The majority of the computational time needed in the construction of the energy matrix is spent evaluating the elements of the potential energy matrix. While the factorization process does not result in any significant computational time savings for the elements of the overlap and kinetic energy matrices, it does reduce the needed computational time by more than 50% for the potential energy matrix elements. As a result, the required computational time for the construction of the energy matrix is also reduced by more than 50%. From Eqs. (2.18), (2.38),

and (2.40), the elements involving the $V_j^g(\mathbf{r})$ term which need to be evaluated are expressed as

$$V_{n_1 \ell_1 m_1, n_2 \ell_2 m_2}^g(\alpha_{i_1}, \alpha_{i_2}, \beta_{i_3}^{j_3}, \mathbf{A}, \mathbf{B}, \mathbf{C}) = \sum_{i_2} \sum_{i_1} d_{n_1 \ell_1 m_1}^{j_1}(\alpha_{i_1}) d_{n_2 \ell_2 m_2}^{j_2}(\alpha_{i_2}) \sum_{\mathbf{v}} \exp\{i\mathbf{k} \cdot \mathbf{R}_{\mathbf{v}}\} \\ \times \sum_{\mathbf{v}'} \sum_{j_3} \sum_{i_3} \sigma_{i_3}^{j_3} \int \chi_{n_1 \ell_1 m_1}^{j_1}(\alpha_{i_1}, \mathbf{r}_{\mathbf{A}}) \chi_{000}^{j_3}(\beta_{i_3}^{j_3}, \mathbf{r}_{\mathbf{C}}) \chi_{n_2 \ell_2 m_2}^{j_2}(\alpha_{i_2}, \mathbf{r}_{\mathbf{B}}) d\tau, \quad (2.56)$$

where $\mathbf{r}_{\mathbf{C}} = \mathbf{r} - (\mathbf{R}_{\mathbf{v}'} + \mathbf{t}_{j_3}) = \mathbf{r} - \mathbf{C}$. Using the factorization of the GTO's, these elements can be rewritten as

$$V_{n_1 \ell_1 m_1, n_2 \ell_2 m_2}^g(\alpha_{i_1}, \alpha_{i_2}, \beta_{i_3}^{j_3}, \mathbf{A}, \mathbf{B}, \mathbf{C}) = \sum_{i_2} \sum_{i_1} d_{n_1 \ell_1 m_1}^{j_1}(\alpha_{i_1}) d_{n_2 \ell_2 m_2}^{j_2}(\alpha_{i_2}) \sum_{\mathbf{v}} \exp\{i\mathbf{k} \cdot \mathbf{R}_{\mathbf{v}}\} \\ \times \sum_{\mathbf{v}'} \sum_{j_3} \sum_{i_3} \sigma_{i_3}^{j_3} U_{n_1 n_2}^0(\alpha_{i_1}, \alpha_{i_2}, \beta_{i_3}^{j_3}, \mathbf{A}_x, \mathbf{B}_x, \mathbf{C}_x) U_{\ell_1 \ell_2}^0(\alpha_{i_1}, \alpha_{i_2}, \beta_{i_3}^{j_3}, \mathbf{A}_x, \mathbf{B}_x, \mathbf{C}_x) \\ \times U_{m_1 m_2}^0(\alpha_{i_1}, \alpha_{i_2}, \beta_{i_3}^{j_3}, \mathbf{A}_x, \mathbf{B}_x, \mathbf{C}_x). \quad (2.57)$$

The term involving the x-components has the following form

$$U_{n_1 n_2}^0(\alpha_{i_1}, \alpha_{i_2}, \beta_{i_3}^{j_3}, \mathbf{A}_x, \mathbf{B}_x, \mathbf{C}_x) = \int x^{n_1+n_2} \exp\{-\alpha_{i_1} x_A^2 - \alpha_{i_2} x_A^2 - \beta_{i_3}^{j_3} x_C^2\} dx \quad (2.58)$$

and the evaluation of the three-center integral yields

$$U_{n_1 n_2}^0(\alpha_{i_1}, \alpha_{i_2}, \beta_{i_3}^{j_3}, \mathbf{A}_x, \mathbf{B}_x, \mathbf{C}_x) = \exp\{-H(AB)_x^2\} \exp\{-G(CD)_x^2\} \\ \times \sum_{r_1} \binom{n_1}{r_1} (AP)_x^{n_1-r_1} \sum_{r_2} \binom{n_2}{r_2} (BP)_x^{n_2-r_2} E_{r_1+r_2}(\lambda), \quad (2.59)$$

where $\lambda = \alpha_{i_1} + \alpha_{i_2} + \beta_{i_3}^{j_3}$, $P_x = [(\alpha_{i_1} + \alpha_{i_2})D_x + \beta_{i_3}^{j_3}C_x] / \lambda$, and $G = (\alpha_{i_1} + \alpha_{i_2})\beta_{i_3}^{j_3} / \lambda$. For a rectangular unit cell, the matrix elements involving the $V_j^g(\mathbf{r})$ term reduce down to the 3N

problem

$$\begin{aligned}
V_{n_1 \ell_1 m_1 n_2 \ell_2 m_2}^g(\alpha_{i_1}, \alpha_{i_2}, \beta_{i_3}^{j_3}, \mathbf{A}, \mathbf{B}, \mathbf{C}) = \\
\sum_{i_2} \sum_{i_1} d_{n_1 \ell_1 m_1}^{j_1}(\alpha_{i_1}) d_{n_2 \ell_2 m_2}^{j_2}(\alpha_{i_2}) \sum_{j_3} \sum_{i_3} \sigma_{i_3}^{j_3} \left[\sum_{v_1} \sum_{v_1'} \exp\{i2\pi k_x (v_1 + v_1')\} U_{n_1 n_2}^0(\alpha_{i_1}, \alpha_{i_2}, \beta_{i_3}^{j_3}, \mathbf{A}_x, \mathbf{B}_x, \mathbf{C}_x) \right] \\
\times \left[\sum_{v_2} \sum_{v_2'} \exp\{i2\pi k_y (v_2 + v_2')\} U_{\ell_1 \ell_2}^0(\alpha_{i_1}, \alpha_{i_2}, \beta_{i_3}^{j_3}, \mathbf{A}_y, \mathbf{B}_y, \mathbf{C}_y) \right] \\
\times \left[\sum_{v_3} \sum_{v_3'} \exp\{i2\pi k_z (v_3 + v_3')\} U_{m_1 m_2}^0(\alpha_{i_1}, \alpha_{i_2}, \beta_{i_3}^{j_3}, \mathbf{A}_z, \mathbf{B}_z, \mathbf{C}_z) \right]. \quad (2.60)
\end{aligned}$$

From Eqs. (2.18), (2.38), and (2.39), the elements involving the $V_j^c(\mathbf{r})$ term which need to be evaluated are expressed as

$$\begin{aligned}
V_{n_1 \ell_1 m_1 n_2 \ell_2 m_2}^c(\alpha_{i_1}, \alpha_{i_2}, \beta_0^{j_3}, \mathbf{A}, \mathbf{B}, \mathbf{C}) = -\sum_{i_2} \sum_{i_1} d_{n_1 \ell_1 m_1}^{j_1}(\alpha_{i_1}) d_{n_2 \ell_2 m_2}^{j_2}(\alpha_{i_2}) \sum_{\mathbf{v}} \exp\{i\mathbf{k} \cdot \mathbf{R}_{\mathbf{v}}\} \\
\times \sum_{\mathbf{v}'} \sum_{j_3} Z_{j_3} \int \chi_{n_1 \ell_1 m_1}^{j_1}(\alpha_{i_1}, \mathbf{r}_A) [\chi_{000}^{j_3}(\beta_0^{j_3}, \mathbf{r}_C) / r_C] \chi_{n_2 \ell_2 m_2}^{j_2}(\alpha_{i_2}, \mathbf{r}_B) d\tau. \quad (2.61)
\end{aligned}$$

Evaluation of the three-center integral, which cannot be factorized, gives the following expression for these elements

$$\begin{aligned}
V_{n_1 \ell_1 m_1 n_2 \ell_2 m_2}^c(\alpha_{i_1}, \alpha_{i_2}, \beta_0^{j_3}, \mathbf{A}, \mathbf{B}, \mathbf{C}) = -\pi^{-1/2} \sum_{i_2} \sum_{i_1} d_{n_1 \ell_1 m_1}^{j_1}(\alpha_{i_1}) d_{n_2 \ell_2 m_2}^{j_2}(\alpha_{i_2}) \sum_{\mathbf{v}} \exp\{i\mathbf{k} \cdot \mathbf{R}_{\mathbf{v}}\} \\
\times \sum_{\mathbf{v}'} \sum_{j_3} Z_{j_3} \exp\{-H(\mathbf{AB})^2\} \sum_{r_1} \binom{n_1}{r_1} (\mathbf{AB})_x^{n_1-r_1} \sum_{s_1} \binom{\ell_1}{s_1} (\mathbf{AB})_y^{\ell_1-s_1} \sum_{t_1} \binom{\ell_1}{t_1} (\mathbf{AB})_z^{m_1-t_1} \sum_{r'} \binom{n_2+r_1}{r'} N_{r'} \\
\times \sum_{s'} \binom{\ell_2+s_1}{s'} N_{s'} \sum_{t'} \binom{m_2+t_1}{t'} N_{t'} \sum_{r''} \binom{n_2+r_1-r'}{r''} (\mathbf{BC})_x^{n_2+r_1-r'-r''} (\mathbf{CD})_x^{r''} (\alpha_{i_1} + \alpha_{i_2})^{r''} \\
\times \sum_{s''} \binom{\ell_2+s_1-s'}{s''} (\mathbf{BC})_y^{\ell_2+s_1-s'-s''} (\mathbf{CD})_y^{s''} (\alpha_{i_1} + \alpha_{i_2})^{s''} \sum_{t''} \binom{m_2+t_1-t'}{t''} (\mathbf{BC})_z^{m_2+t_1-t'-t''} \\
\times (\mathbf{CD})_z^{r''} (\alpha_{i_1} + \alpha_{i_2})^{t''} \kappa_{(r'+s'+t'+2r''+2s''+2t'')/2}(\alpha_{i_1} + \alpha_{i_2}, \beta_0^{j_3}, \alpha_{i_1} + \alpha_{i_2} + \beta_0^{j_3}, (\mathbf{CD})), \quad (2.62)
\end{aligned}$$

where

$$\kappa_n(\alpha, \beta, \delta, z) = \delta^{-(n+1)} \exp\{-\alpha\beta z^2 / \delta\} \sum_q \binom{n}{q} (-1)^q \Gamma(q+1/2) \gamma^*(q+1/2, \alpha^2 z^2 / \delta) \quad (2.63)$$

and $\gamma^*(a, x)$ is the entire incomplete gamma function

$$\gamma^*(a, x) = (x^{-a} / \Gamma(a)) \int_0^x e^{-t} t^{a-1} dt. \quad (2.64)$$

Density Of States

For N number of basis functions, evaluation of the energy matrix will yield N one-electron energy eigenvalues and wave functions. From Eqs. (2.12) and (2.17), each wave function is expressed as

$$\psi_a(\mathbf{k}, \mathbf{r}) = N^{-1/2} \sum_{j, n\ell m} C_{j,a}^{n\ell m}(\mathbf{k}) \sum_{\nu} d_{n\ell m}^j(\alpha_{\nu}) \sum_{\nu} \exp\{i\mathbf{k} \cdot \mathbf{R}_{\nu}\} \chi_{n\ell m}(\alpha_{\nu}, \mathbf{r}_{\nu}) \quad (2.65)$$

and it is useful to determine the orbital composition (i.e. s, p, d, ...) so as to associate each wave function with a atomic state (i.e. Zn 1s, Zn 2s, ..) or a mixing of atomic states (i.e. Se 4p / S 3p) (78-81). If the expression

$$\psi_{a, n_1 \ell_1 m_1}^{j_1}(\mathbf{k}, \mathbf{r}) = N^{-1/2} C_{j_1, a}^{n_1 \ell_1 m_1}(\mathbf{k}) \sum_{\nu} d_{n_1 \ell_1 m_1}^{j_1}(\alpha_{\nu}) \sum_{\nu} \exp\{i\mathbf{k} \cdot \mathbf{R}_{\nu}\} \chi_{n_1 \ell_1 m_1}(\alpha_{\nu}, \mathbf{r}_{\nu}) \quad (2.66)$$

represents the part of the wave function constructed from the $n_1 \ell_1 m_1$ orbital of the j_1 th atom in the unit cell, then the orbital composition of each wave function is given by

$$\theta_{a, n_1 \ell_1 m_1}^{j_1}(\mathbf{k}) = N^{-1} \sum_{j_2} \sum_{n_2 \ell_2 m_2} C_{j_1, a}^{n_1 \ell_1 m_1}(\mathbf{k}) C_{j_2, a}^{n_2 \ell_2 m_2}(\mathbf{k}) S_{n_1 \ell_1 m_1, n_2 \ell_2 m_2}(\alpha_{j_1}, \alpha_{j_2}, \mathbf{B}, \mathbf{A}). \quad (2.67)$$

The partial density of states (PDOS) for the $n_1 \ell_1 m_1$ orbital of the j_1 th atom is determined from

$$\text{PDOS}_{n_1 \ell_1 m_1}^{j_1}(E) = (\sqrt{2\pi\sigma})^{-1} \sum_{\mathbf{k}} W(\mathbf{k}) \sum_a \exp\{-[E_a(\mathbf{k}) - E]^2 / 2\sigma^2\} \theta_{a, n_1 \ell_1 m_1}^{j_1}(\mathbf{k}), \quad (2.68)$$

where a sum over the k-points in the fundamental wedge of the first Brillouin zone is performed. In this expression, σ is the specified width of the Gaussian function at half maximum and $W(\mathbf{k})$

is a scaling factor used to weight the \mathbf{k} -points. The total density of states (TDOS) is then given by

$$\text{TDOS} = \sum_{j_1} \sum_{n_1 \ell_1 m_1} O_{n_1 \ell_1 m_1}^{j_1}(E) \quad (2.69)$$

and can be directly compared with experimental x-ray and ultraviolet photoemission measurements.

CHAPTER III

BULK ZnSe AND ZnS

Introduction

The electronic structure of bulk ZnSe and ZnS have been studied extensively by both experimental and theoretical methods. Interband transition energies at high symmetry points have been determined through: x-ray photoemission measurements by Chelikowsky *et al* (82) and by Ley *et al* (83,84), ultraviolet photoemission measurements by Eastman *et al* (85), and reflectivity measurements by Theis (86) and Walter *et al* (87,88). Semi-empirical calculations of the electronic band structure of the bulk materials have been performed using: the semi-empirical sp^3 tight-binding method [e.g., Pantelides and Harrison (89) and by Chadi and Cohen (90)]; the semi-empirical sp^3s^* tight-binding method [e.g., Bertho *et al* (91), Ekpenuma and Myles (92), and Vogl *et al* (93)]; the empirical pseudopotential method [e.g., Qteish and Needs (94), Chelikowsky *et al* (82,95), and by Cohen and Bergstresser (96)]; and the KKR method [e.g., Eckelt *et al* (97)]. *ab initio* self-consistent calculations have been performed using the orthogonalized-plane-wave (OPW) method [e.g., Stukel *et al* (98)]; the Hartree-Fock method [e.g., Jaffe *et al* (99)]; the LMTO method [e.g., Christensen *et al* (100)]; the potential-variation mixed-basis (PVMB) method [e.g., Bernard and Zunger (101)]; and the linear combination of Gaussian orbitals (LCGO) method [e.g., Wang and Klein (43,44)]. In addition, nonself-consistent *ab initio* calculations have been performed using the LAPW method [e.g., Martins *et al* (102) and Continenza *et al* (103)]; the pseudopotential plane-wave (PPW) method [e.g., Martins *et al* (102)]; the LCGO method [e.g., Ghahramani *et al* (104)]; and the orthogonalized LCAO (OLCAO) method by Huang and Ching (42). In this chapter, the electronic structure of bulk ZnSe and ZnS as determined from the *ab initio* nonself-consistent FLCAO method by

Marshall and Wilson (105) will be presented. The motivation behind this work was that the existing experimental and theoretical data on the bulk II-VI compounds provided a means to determine the effectiveness of this method.

Except for the Hartree-Fock calculation, all the *ab initio* calculations were performed within the framework of the local density functional approximation (LDA). The PVMB and PPW calculations were made using the Ceperley-Alder exchange-correlation (EC) (38,39) as parameterized by Perdew and Zunger (40), the LAPW calculation using the Hedin-Lundqvist EC (106), and the LCGO calculation of Wang and Klein using the Wigner EC (107). The remaining calculations used one of the three more common approximations: the Slater EC of Eq. (1.5) was used in the FLCAO and OPW calculations, the Kohn-Sham EC of Eq. (1.6) was used in the LMTO calculation, and the $X\alpha$ EC of Eq. (1.7) was used in the LCGO calculation of Ghahramani *et al* and the OLCAO calculation. In the last two calculations, α was used as an adjustable parameter to provide the best fit between the calculated and experimental band gap energies.

The Unit Cell

The zincblende structure, shown in Figure 4, can be viewed as two interpenetrating face-centered cubic lattices displaced from each other by one-quarter of a body diagonal. The two smallest unit cells exhibiting the periodicity of the crystal lattice that can be constructed are the primitive non-rectangular two-atom unit cell and the tetragonal four-atom unit cell. The lattice vectors of the two-atom unit cell, in terms of the x-, y-, and z-coordinates, are

$$\mathbf{A}_1 = (a/2)(1,1,0), \quad \mathbf{A}_2 = (a/2)(0,1,1), \quad \text{and} \quad \mathbf{A}_3 = (a/2)(1,0,1); \quad (3.1)$$

where a is the lattice constant of the crystal. The group-II zinc atom is positioned at the origin and the group-VI selenium or sulfur atom is displaced from the zinc atom by one-quarter of a body diagonal so that

$$\mathbf{t}_1 = (0,0,0) \quad \text{and} \quad \mathbf{t}_2 = (a/4)(1,1,1). \quad (3.2)$$

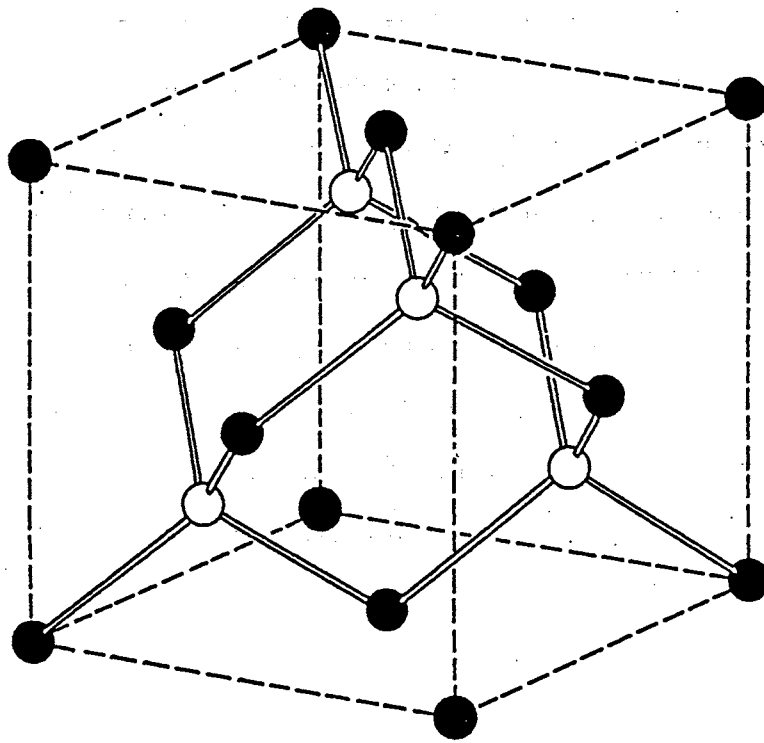


Figure 4. The crystal structure of cubic zincblende compounds such as bulk ZnSe and ZnS.

The corresponding axis vectors of the reciprocal lattice are

$$\mathbf{b}_1 = (2\pi / a)(-1, 1, 1), \quad \mathbf{b}_2 = (2\pi / a)(1, -1, 1), \quad \text{and} \quad \mathbf{b}_3 = (2\pi / a)(1, 1, -1), \quad (3.3)$$

which are just the lattice vectors of a body-centered cubic lattice. The eight planes normal to the reciprocal lattice vectors $(2\pi / a)(\pm 1, \pm 1, \pm 1)$ at their midpoints form an octahedron. The six planes that are the perpendicular bisectors of the reciprocal lattice vectors $(2\pi / a)(\pm 1, 0, 0)$, $(2\pi / a)(0, \pm 1, 0)$, and $(2\pi / a)(0, 0, \pm 1)$, however, cut the corners of the octahedron. The resulting truncated octahedron, shown in Figure 5, forms the first Brillouin zone of the non-rectangular two-atom unit cell.

The lattice vectors for the four-atom tetragonal unit cell, in terms of the x-, y-, and z-coordinates, are

$$\mathbf{A}_1 = (a / 2)(1, 1, 0), \quad \mathbf{A}_2 = (a / 2)(1, -1, 0), \quad \text{and} \quad \mathbf{A}_3 = a(0, 0, 1). \quad (3.4)$$

The zinc atoms are positioned at

$$\mathbf{t}_1 = (0, 0, 0) \quad \text{and} \quad \mathbf{t}_2 = (a / 2)(1, 0, 1) \quad (3.5)$$

and the selenium or sulfur atoms are positioned at

$$\mathbf{t}_3 = (a / 4)(1, 1, 1) \quad \text{and} \quad \mathbf{t}_4 = (a / 4)(1, -1, 3). \quad (3.6)$$

The corresponding axis vectors of the reciprocal lattice are

$$\mathbf{b}_1 = (2\pi / a)(1, 1, 0), \quad \mathbf{b}_2 = (2\pi / a)(1, -1, 0), \quad \text{and} \quad \mathbf{b}_3 = (2\pi / a)(0, 0, 1) \quad (3.7)$$

so that the first Brillouin zone constructed out of the reciprocal lattice vectors also has tetragonal symmetry, as shown in Figure 6. The electronic band structure of the bulk compounds was calculated using the primitive unit cell. For the calculation of the total density of states, however, the tetragonal unit cell was used because of the simpler Brillouin zone.

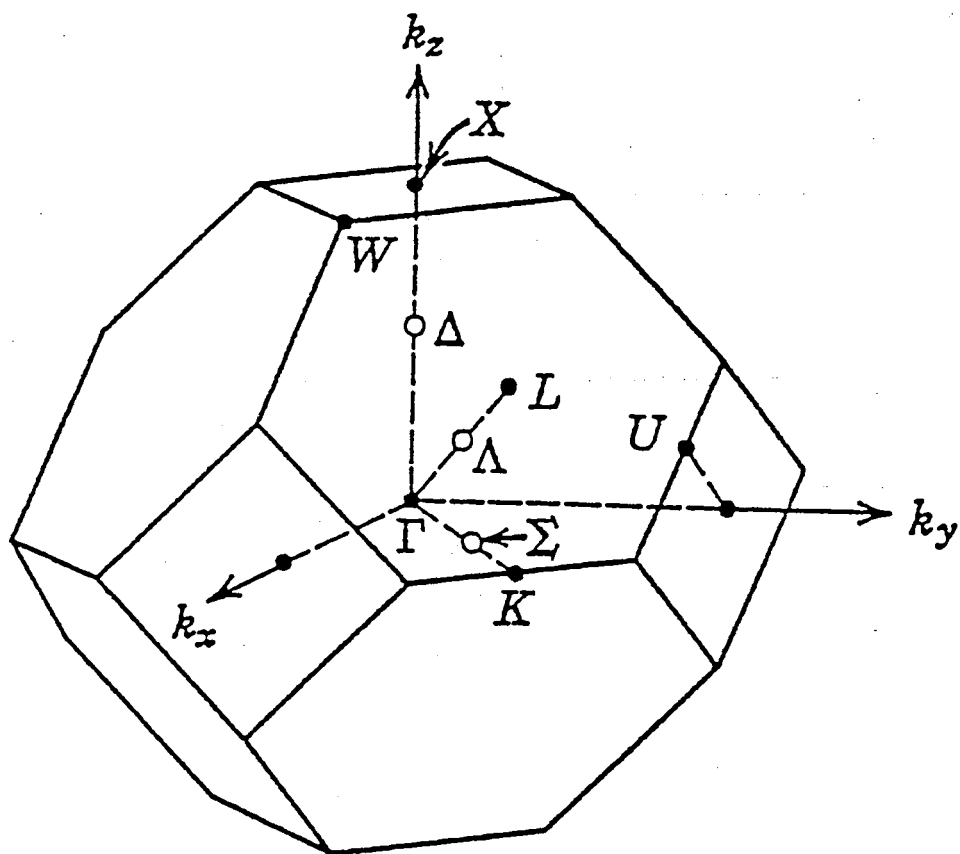


Figure 5. The first Brillouin zone of the face-centered cubic lattice showing the symmetry points.

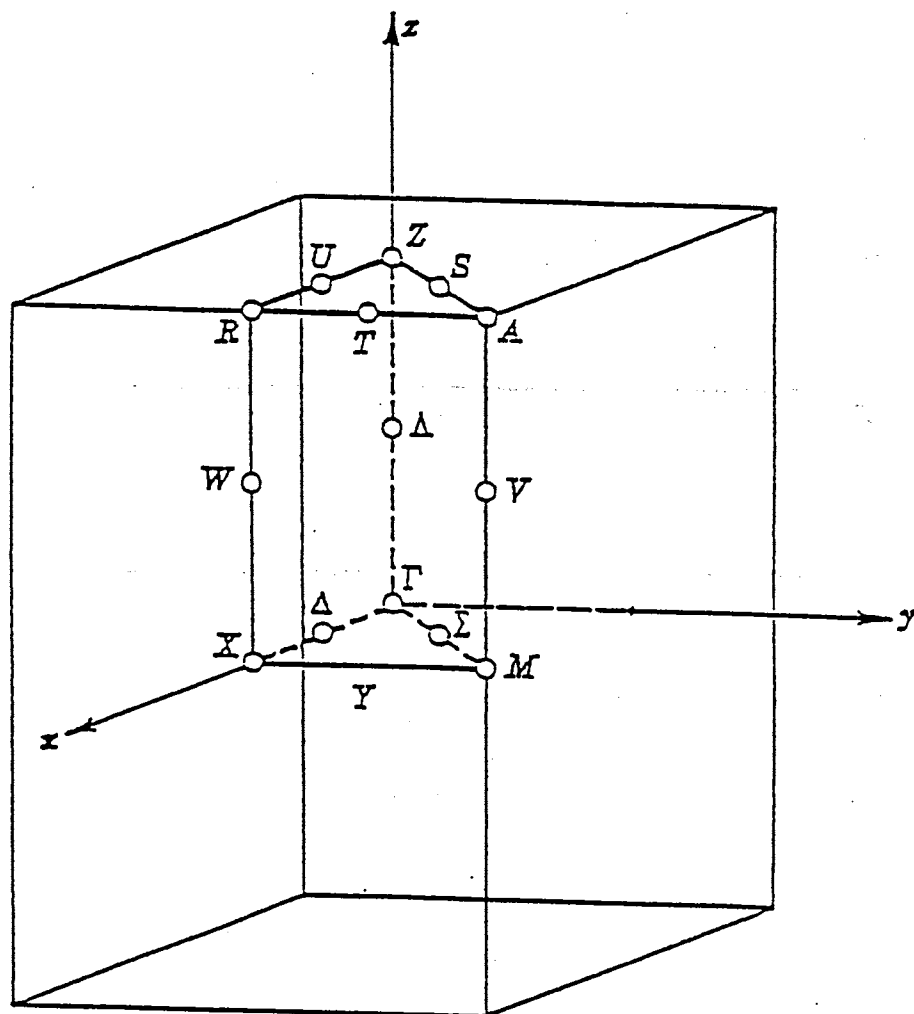


Figure 6. The first Brillouin zone of the tetragonal lattice showing the symmetry points and the irreducible wedge used to determine the density of states.

The Crystalline Potential

The numerical calculation of the crystalline potential and the subsequent fit to the analytical expression in Eq. (2.37) was performed using the procedure discussed in the previous chapter with the exchange parameter set to unity. During the calculations of the self-consistent spherically-symmetric atomic charge densities, the Latter cutoff potential in Eq. (2.35) was not used as a correction to the Herman-Skillman potential for large values of the radius. Furthermore, it was assumed that the Zn atom was in the first excited state ($3d^{10}4s4p$) while the ground state configuration was used for the Se ($4s^24p^4$) and S ($3s^23p^4$) atoms. During the numerical calculation of the crystalline potential, the specified grid for both bulk compounds consisted of four directions for each type of atom in the unit cell: i) the direction directly towards a nearest neighbor, ii) the direction directly opposite from a nearest neighbor, iii) the direction directly towards a next nearest neighbor, and iv) the direction directly opposite from a next nearest neighbor. For the fit of the crystalline potential to the analytic expression, eleven non-linear coefficients were used for each unique atomic-centered potential (ACP). Larger fits were performed, but none showed any significant improvement over the smaller fit. Furthermore, the computational time needed to perform a potential fit increased with the size of the fit. The linear and non-linear coefficients of the ACP's for bulk ZnSe and ZnS are listed in Table I. In Figure 7, the difference between the numeric and analytic crystalline potentials for bulk ZnSe along the nearest neighbor bonding direction is shown. As can be seen from this figure, the largest discrepancy occurs in the region close to the nuclei and should have no impact on the valence and conduction states.

TABLE I
 COEFFICIENTS FOR THE ANALYTIC ATOMIC-CENTERED
 POTENTIALS OF BULK ZnSe AND ZnS
 (values are in atomic units)

Bulk ZnSe				Bulk ZnS			
Zinc ACP				Zinc ACP		Sulfur ACP	
β_0	2685.0700			β_0	2162.7500		
β_1	0.0805989	σ_1	-0.2616660	β_1	0.0613623	σ_1	0.2643280
β_2	0.2644960	σ_2	-0.7784020	β_2	0.2023960	σ_2	-0.8859110
β_3	0.8679790	σ_3	-3.9147400	β_3	0.6675780	σ_3	-3.0402900
β_4	2.8483900	σ_4	-15.647500	β_4	2.2019200	σ_4	-7.4765600
β_5	9.3473700	σ_5	-45.246800	β_5	7.2627800	σ_5	-22.307300
β_6	30.674600	σ_6	-91.883300	β_6	23.955400	σ_6	-43.721700
β_7	100.66300	σ_7	-193.01000	β_7	79.013800	σ_7	-95.690700
β_8	330.33900	σ_8	-347.56800	β_8	260.61700	σ_8	-166.66100
β_9	1084.5000	σ_9	-679.26600	β_9	859.61400	σ_9	-327.90600
β_{10}	3557.4500	σ_{10}	930.48400	β_{10}	2835.3300	σ_{10}	437.73900

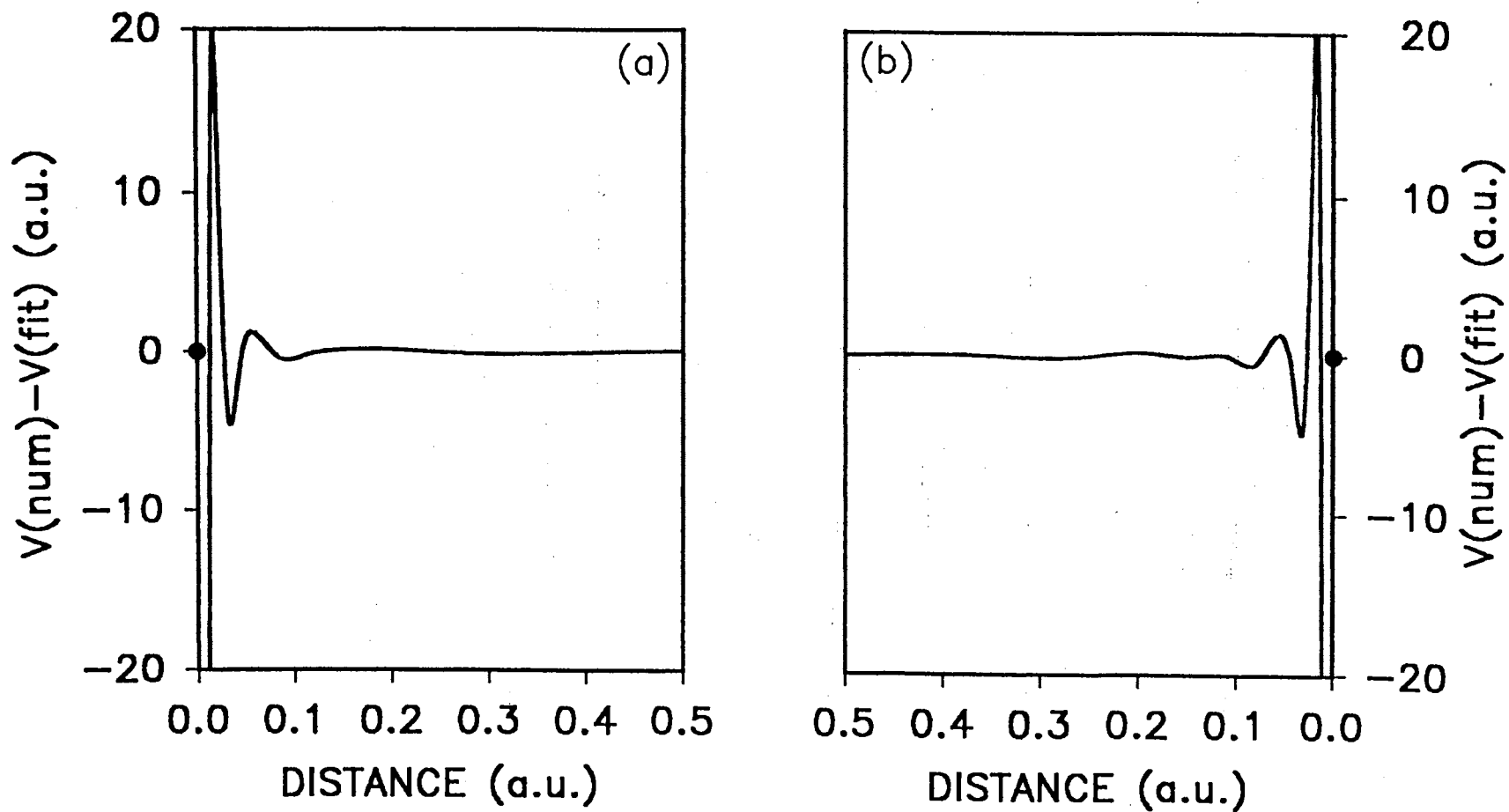


Figure 7. The difference between the numeric and analytic crystalline potentials of bulk ZnSe for (a) the direction from a Zn atom towards a nearest neighbor Se atom and (b) the direction from a Se atom towards a nearest neighbor Zn atom.

The Basis

For the bulk calculations, uncontracted atomic Gaussian basis sets constructed for use in *ab initio* molecular calculations were used for Zn (108), Se (72), and S (109). Because the ACP's behave much like the atomic potentials in the region close to the nucleus, the core states of the bulk materials are expected to be very similar to the atomic core states of Zn, Se, and S (i.e. the bulk compound core energies are expected to be approximately equal to the atomic core energies). Contractions were then performed on the s- and p-GTO's of Zn and Se to construct the atomic-like Zn and Se 1s, 2s, 2p, 3s, and 3p core basis functions of ZnSe. Similarly, contractions were performed on the s- and p-GTO's of Zn and S to construct the atomic-like Zn and S 1s, 2s, 2p, and 3s core basis functions and the Zn 3p core basis function of ZnS. No orthogonality conditions were placed on these contractions. The contraction procedure used in this work is straightforward. The basis was initially left uncontracted so that each basis function was constructed from a single GTO, which was not normalized. A electronic structure calculation was then performed at the Γ -point, where the direct band gap is located. The only non-negligible $C_j^{n\ell m}$'s were those corresponding to the core GTO's for the $n\ell m$ orbital of the j th atom. As a result, the one-electron wave function could be approximated as

$$\psi(\Gamma, \mathbf{r}) = \sum_i C_{j\text{-core}}^{n\ell m}(\alpha_i, \Gamma) x^n y^\ell z^m \exp\{-\alpha_i r^2\}. \quad (3.8)$$

In general, such wave functions will not be normalized so that

$$|\psi(\Gamma, \mathbf{r})|^2 = N^2 = \sum_i \sum_{i'} C_{j\text{-core}}^{n\ell m}(\alpha_i, \Gamma) C_{j\text{-core}}^{n\ell m}(\alpha_{i'}, \Gamma) n_{i,i'} \quad (3.9)$$

where

$$n_{i,p} = \int x^{2n} y^{2\ell} z^{2m} \exp\{-(\alpha_i + \alpha_p)r^2\} dr$$

$$= \frac{\pi^{3/2} (2n-1)!!(2\ell-1)!!(2m-1)!!}{2^{n+\ell+m} (\alpha_i + \alpha_p)^{n+\ell+m+3/2}} \quad (3.10)$$

The constraint on the above equation is that $n + \ell + m = 0$ for an s-state, $n + \ell + m = 1$ for a p-state, and $n + \ell + m = 2$ for a d-state. The normalized expansion coefficients of Eq. (2.15) were then determined from

$$d_{j\text{-core}}^{n,\ell,m}(\alpha_i) = C_{j\text{-core}}^{n,\ell,m}(\alpha_i, \Gamma) / N. \quad (3.11)$$

The valence states of the bulk compounds, on the other hand, are not expected to be similar to the atomic valence states. Thus, these states were represented by the atomic-like basis functions augmented by several uncontracted diffuse GTO's from the atomic bases.

Electronic Band Structure Results

A common technique used to reduce the complexity and computational time of an electronic band structure calculation is the removal of the most diffuse GTO's from the basis. To test the validity of such an approximation, the most diffuse Zn s-GTO was removed from both bases. The resulting electronic band structure showed a good representation of the core and valence states. Excluding the lowest conduction band, however, overall accuracy was lost with the conduction states as their energies were several eV too high. Returning the diffuse Zn s-GTO to the bases, the calculations were repeated. The resulting electronic band structure showed that the valence states deviated from the previous results by only a few hundredths of an eV. While the conduction states showed improvement, the energies were still a few eV higher than expected. To attain a good representation of the conduction states, both bases were augmented with a diffuse Zn p-GTO (0.15000). Contractions were performed to generate the atomic-like core basis functions, which were then augmented with uncontracted diffuse GTO's (including the additional Zn p-GTO) to bring the basis size to 102 basis functions for

ZnSe and 72 basis functions for ZnS. The expansion and exponential coefficients of the ZnSe and ZnS bases are shown in Tables II and III, respectively.

As was expected, the core energies of the bulk compounds were roughly equal to the non-relativistic Herman-Skillman atomic core energies, as shown in Table IV, and showed no dispersion throughout the first Brillouin zone. The resulting electronic band structure and TDOS in the region near the forbidden band gap for bulk ZnSe and ZnS are shown in Figures 8 and 9, respectively. In Table V, the calculated one-electron energy eigenvalues at high symmetry points are compared with those determined using the basis with the diffuse Zn s-GTO removed and with experimental results. Tables VI and VII compares the results of these bulk calculations with those from the OLCAO, LCGO, PVMB, and OPW calculations. In both compounds, as assumed, the resulting band gap was direct at the Γ -point and the band gap energy was underestimated (which is well known to occur for calculations using the LDA). Furthermore, the expected degeneracies were also found. Since relativistic effects were not considered, the valence band maximum has a three-fold degeneracy, consisting of the heavy-hole, light-hole, and split-off states. Through an orbital composition analysis (discussed in the previous chapter) at high symmetry points, each of the bulk bands was found to have a dominant atomic-like characteristic even though a considerable amount of dispersion is present. The lowest valence band had a Se 4s/S 3s character, while the character of the three upper valence bands was Se 4p/S 3p. The character of the middle (shaded) valence bands was found to be Zn 3d. The conduction bands are all associated with cation states, the lowest being the Zn 4s in character and the other three being Zn 4p in character. The FLCAO results, as would be expected, are very similar to the OLCAO results. Significant differences, though, are present in comparison to the LCGO, PVMB, and OPW results. In general, the FLCAO upper valence bands and conduction bands lie higher by a few tenths of an eV to a few eV than the corresponding bands from the three self-consistent methods. Self-consistent calculations using the LDA, however, are known to underestimate the excited states (98,101,43). It is interesting

TABLE II
 GAUSSIAN ORBITAL EXPONENTS AND
 EXPANSION COEFFICIENTS FOR ZnSe

Orbital Exponents
 (The * indicates the uncontracted GTO was included in the basis.)

Zinc			Selenium		
s	p	d	s	p	d
316336.0	2213.180	58.40840*	257900.0	1724.000	94.03000*
48561.00	527.0500	16.44920*	39020.00	400.3000	26.79000*
11157.40	172.2930	5.575700*	8960.000	125.1000	9.336000*
3205.010	66.08140	1.884410*	2550.000	45.49000	3.383000*
1068.580	27.68630	0.572305*	846.3000	18.00000	1.145000*
396.3940	12.18410		313.3000	6.077000	
159.8060	4.987960		122.1000	2.213000*	
68.58900	2.057910*		34.76000	0.483400*	
23.70810	0.798609*		14.97000	0.144100*	
10.03720	0.150000*		4.468000		
2.810430			1.921000*		
1.069640*			0.363100*		
0.146951*			0.139800*		
0.051142*					

Normalized Expansion Coefficients for Zinc

1s	2s	3s	2p	3p
0.0003315150	0.0001146520	0.0000386745	0.0026542100	0.0010175000
0.0024902400	0.0008647530	0.0002916420	0.0215714000	0.0083105100
0.0138657000	0.0048328700	0.0016322600	0.0973725000	0.0388881000
0.0496034000	0.0177495000	0.0060057700	0.2745500000	0.1146320000
0.1502580000	0.0572064000	0.0195458000	0.4332770000	0.1992350000
0.3277610000	0.1447040000	0.0502221000	0.3093240000	0.0715788000
0.4027610000	0.2484310000	0.0909294000	0.0531497000	-0.3722980000
0.1917340000	0.1119630000	0.0473626000	-0.0036266600	-0.5596500000
0.0090885600	-0.6481480000	-0.4490930000	0.0011673500	-0.2163940000
0.0054852500	-0.5619130000	-0.2770920000	-0.0002790390	-0.0057798800
0.0010254900	0.0490370000	0.8615480000		
0.0005508890	0.0295533000	0.3933460000		
0.0000350833	0.0020400900	-0.0070902600		
-0.0000110129	-0.0006371470	0.0016737400		

TABLE II (Continued)

Normalized Expansion Coefficients For Selenium

1s	2s	3s	2p	3p
0.0005812860	0.0002184240	0.0000727890	0.0065203000	0.0026024200
0.0045321000	0.0017158400	0.0005726160	0.0520774000	0.0217285000
0.0241359000	0.0091758900	0.0030617300	0.2219460000	0.0945521000
0.0853849000	0.0340503000	0.0114424000	0.4660100000	0.2269160000
0.2403270000	0.1046640000	0.0355219000	0.3872410000	0.1091120000
0.4184410000	0.2362050000	0.0832663000	0.0589240000	-0.5215840000
0.3291160000	0.2419680000	0.0918720000	-0.0078183000	-0.5730170000
0.0226247000	-0.5699870000	-0.3228500000	0.0024842100	-0.0635806000
0.0408826000	-0.6676630000	-0.4787990000	-0.0014942300	0.0227469000
0.0196870000	0.0572640000	0.6573720000		
0.0142881000	0.0527009000	0.6347100000		
0.0009897850	0.0039692200	-0.0031279700		
-0.0005148870	-0.0021031600	0.0235703000		

TABLE III
GAUSSIAN ORBITAL EXPONENTS AND
EXPANSION COEFFICIENTS FOR ZnS

Orbital Exponents (The * indicates the uncontracted GTO was included in the basis.)					
Zinc			Sulfur		
s	p	d	s	p	
316336.0	2213.180	58.40840*	93413.40	495.0400	
48561.00	527.0500	16.44920*	13961.70	117.2200	
11157.40	172.2930	5.575700*	3169.900	37.50700	
3205.010	66.08140	1.884410*	902.4600	13.91000	
1068.580	27.68630	0.572305*	297.1600	5.504500	
396.3940	12.18410		108.7020	2.243300*	
159.8060	4.987960		43.15500	0.762000*	
68.58900	2.057910*		18.10800	0.291900*	
23.70810	0.798609*		5.570500	0.102900*	
10.03720	0.150000*		2.142700*		
2.810430			0.434000*		
1.069640*			0.157000*		
0.146951*					
0.051142*					

Normalized Expansion Coefficients for Zinc				
1s	2s	3s	2p	3p
0.0003311230	0.0001144890	0.0000387390	0.0026590800	0.0010187700
0.0024899900	0.0008645430	0.0002924200	0.0215468000	0.0083023100
0.0138188000	0.0048150000	0.0016313900	0.0974525000	0.0388924000
0.0495283000	0.0177235000	0.0060138400	0.2743320000	0.1145870000
0.1503520000	0.0571977000	0.0196074000	0.4334950000	0.1991480000
0.3275050000	0.1446800000	0.0503414000	0.3092520000	0.0715188000
0.4031970000	0.2482630000	0.0912518000	0.0531478000	-0.3715290000
0.1916770000	0.1124400000	0.0477154000	-0.0036424900	-0.5609420000
0.0091261100	-0.6485460000	-0.4451390000	0.0011939400	-0.2154500000
0.0050298700	-0.5615810000	-0.2891170000	-0.0003260560	-0.0060854900
0.0008824940	0.0490143000	0.8647330000		
0.0004535640	0.0290523000	0.3941710000		
0.0000304471	0.0021536300	-0.0077087800		
-0.0000008687	-0.0006132650	0.0017094500		

TABLE III (Continued)

Normalized Expansion Coefficients For Sulfur			
1s	2s	3s	2p
0.0003068540	0.0000859144	0.0000271755	0.0032458600
0.0026413400	0.0007316560	0.0002327230	0.0262257000
0.0128642000	0.0036513400	0.0011528600	0.1109340000
0.0494774000	0.0140021000	0.0044814800	0.2950570000
0.1537130000	0.0477208000	0.0151133000	0.4406130000
0.3330030000	0.1143490000	0.0375912000	0.2946850000
0.4068210000	0.2076270000	0.0678176000	0.0494938000
0.1847850000	0.0849885000	0.0341973000	-0.0115004000
0.0100362000	-0.5485170000	-0.2639840000	0.0095360000
-0.0020249400	-0.5660600000	-0.3634900000	
0.0008270740	-0.0589305000	0.6889850000	
-0.0007620360	0.0372908000	0.5011550000	

TABLE IV
 CALCULATED ATOMIC CORE-LIKE ENERGIES
 OF BULK ZnSe AND ZnS AT THE BAND EDGE

(All values are in electron volts.)

Atomic Core State	N-R H-S Atomic Core Energy ^a	Bulk ZnSe Atomic Core-Like Energy
Se 1s	-12415.973	-12494.491
Zn 1s	-9502.4268	-9558.1201
Se 2s	-1596.0148	-1601.0376
Se 2p	-1441.4937	-1438.6264
Zn 2s	-1158.1393	-1161.9482
Zn 2p	-1027.9590	-1026.5067
Se 3s	-218.69555	-217.26852
Se 3p	-164.06282	-161.39507
Zn 3s	-133.24160	-132.60383
Zn 3p	-90.625513	-89.359357

Atomic Core State	N-R H-S Atomic Core Energy ^a	Bulk ZnS Atomic Core-Like Energy
Zn 1s	-9502.4268	-9547.8509
S 1s	-2447.4929	-2442.9994
Zn 2s	-1158.1393	-1153.6490
Zn 2p	-1027.9590	-1018.3718
S 2s	-224.63176	-214.67964
S 2p	-171.81404	-161.27821
Zn 3s	-133.24160	-124.37271
Zn 3p	-90.625513	-81.149213

^a Reference (74).

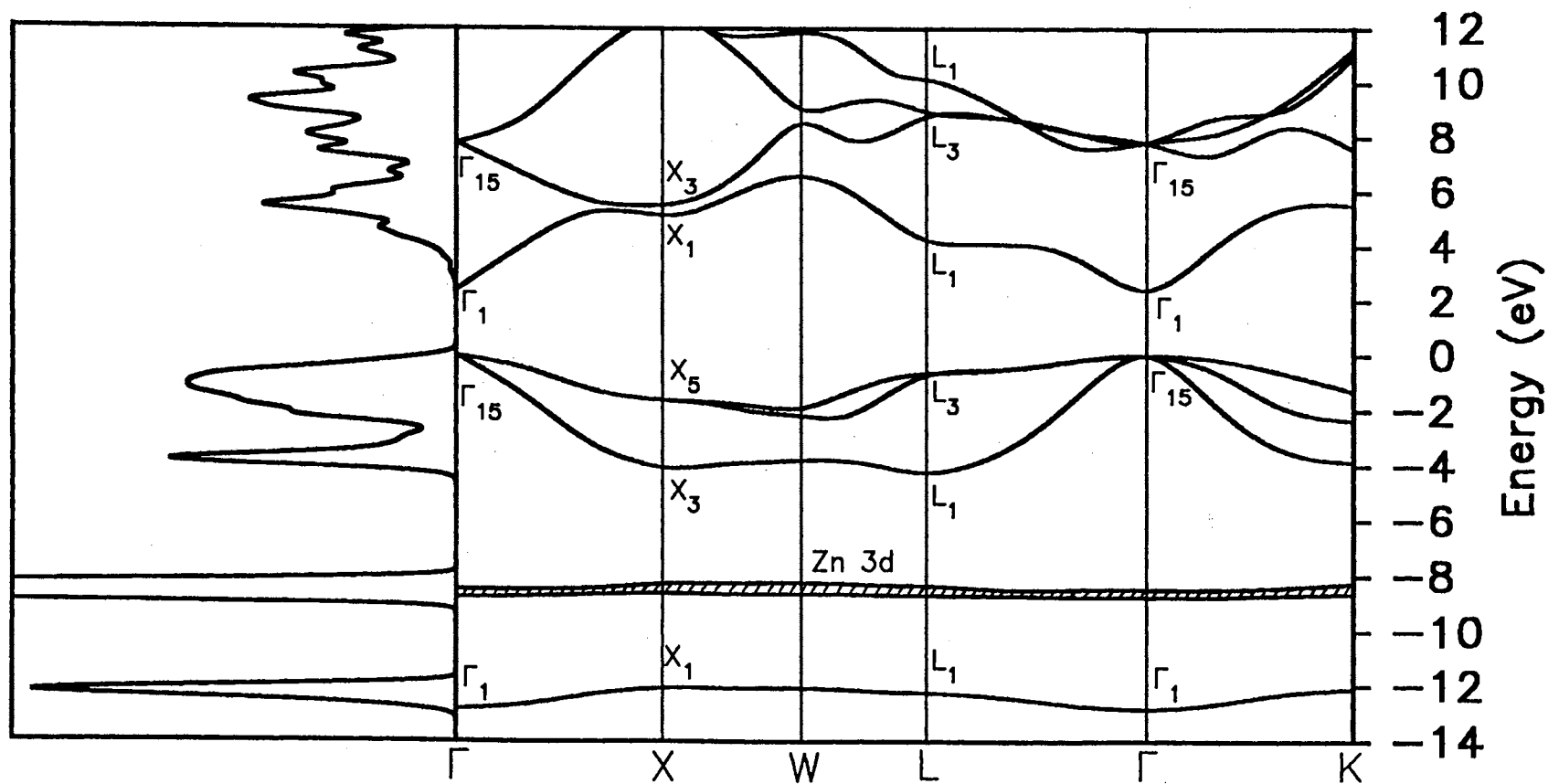


Figure 8. The electronic band structure and total density of states of bulk ZnSe. The resulting band gap is direct and the valence band maximum is three-fold degenerate.

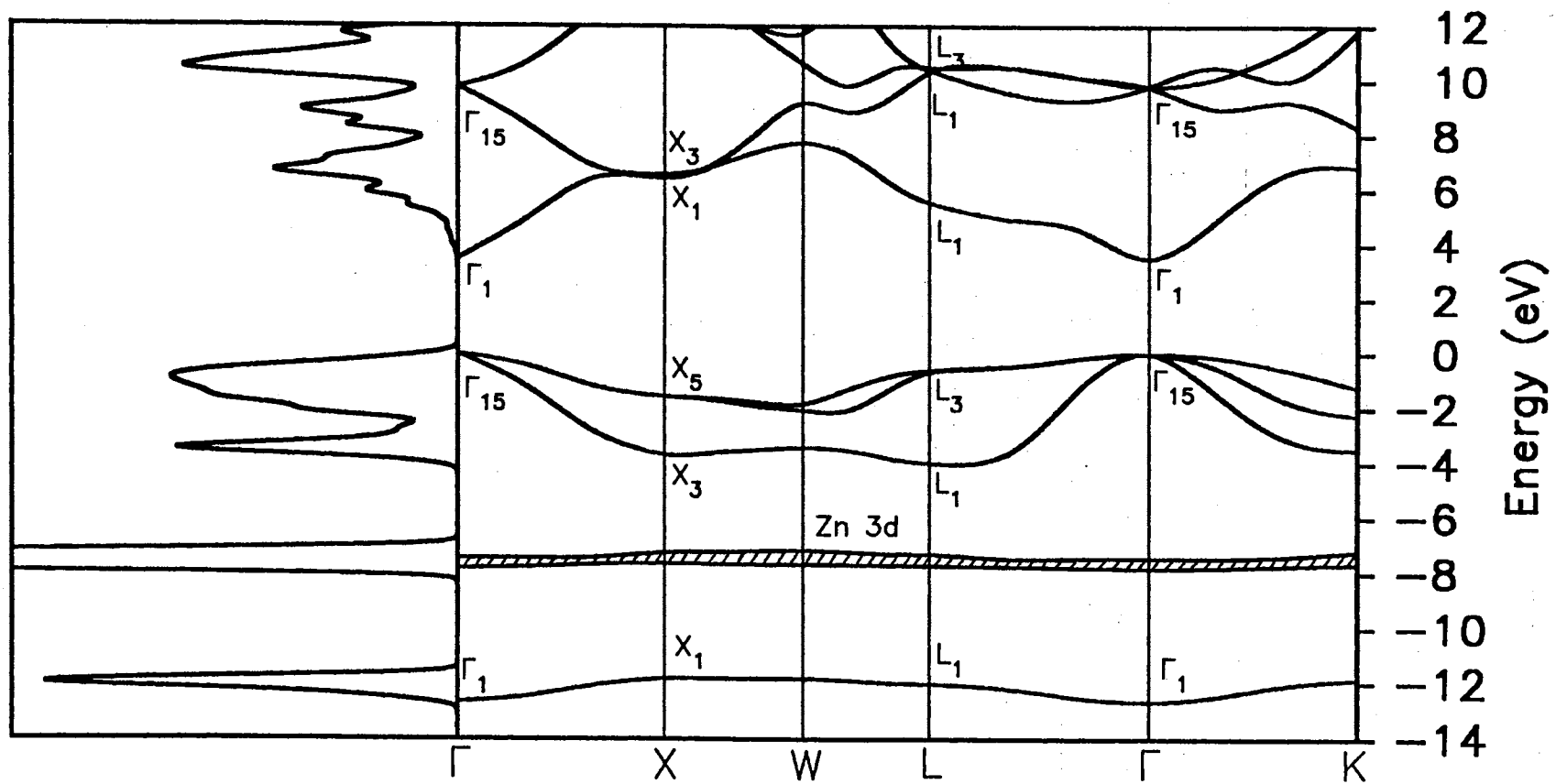


Figure 9. The electronic band structure and total density of states of bulk ZnS. The resulting band gap is direct and the valence band maximum is three-fold degenerate.

TABLE V
CALCULATED ENERGIES AT HIGH SYMMETRY
POINTS FOR BULK ZnSe AND ZnS

(All values are in electron volts and measured with
respect to the valence band maximum.)

Symmetry Point	ZnSe			ZnS		
	FLCAO diff. Zn s- GTO removed	FLCAO diff. Zn p- GTO added	Expt.	FLCAO diff. Zn s- GTO removed	FLCAO diff. Zn p- GTO added	Expt.
G1v	-12.90	-12.83	-15.2(6) ^a	-12.70	-12.66	-13.5(4) ^a
G15v(d)	-8.83	-8.76		-7.86	-7.82	
G12v(d)	-8.55	-8.48		-7.49	-7.45	
G15v	0.00	0.00		0.00	0.00	
G1c	2.56	2.41	2.82 ^b	3.69	3.51	3.85 ^b
G15c	15.60	7.81	7.80 ^{c,d}	20.14	9.79	
G1c		11.93			14.35	
X1v	-12.14	-12.08	-12.5(4) ^a	-11.88	-11.84	-12.0(3) ^a
X3v	-4.10	-4.05	-5.6(3) ^a or -5.3(3) ^e	-3.72	-3.67	-5.5(2) ^a
X5v	-1.53	-1.61	-2.1(3) ^a	-1.49	-1.56	-2.5(3) ^a
X1c	5.19	5.17		6.55	6.44	
X3c	14.14	5.54		12.32	6.58	
X1c		12.28			12.33	
L1v	-12.33	-12.26	-13.1(3) ^a	-12.09	-12.04	-12.4(3) ^a
L1v	-4.23	-4.21		-3.97	-4.00	
L3v	-0.55	-0.62	-1.3(3) ^a or -0.7(2) ^e	-0.53	-0.59	-1.4(4) ^a
L1c	4.15	4.16		5.50	5.44	
L3c	12.89	8.88		10.52	10.47	
L3v → L1c		4.78	4.91 ^b		6.03	5.81 ^b
X5v → X1c		6.78	6.00 ^c		8.00	6.6 ^b

^a Reference (83).

^b Reference (86).

^c Reference (88).

^d Reference (87).

^e Reference (85).

TABLE VI
CALCULATED ENERGIES AT HIGH SYMMETRY
POINTS FOR BULK ZnSe

(All values are in electron volts and measured with respect to the valence band maximum.)

Symmetry Point	FLCAO	OLCAO ^a	LCGO ^b	PVMBC ^c	OPW ^d
G1v	-12.83	-12.37	-12.67	-12.86	-11.82
G15v(d)	-8.76		-6.7	-7.86	-12.6
G12v(d)	-8.48		-6.7	-7.50	
G15v	0.00	0.00	0.00	0.00	0.00
G1c	2.41	2.83	1.83	1.45	2.94
G15c	7.81	7.38	5.86	5.77	6.66
G1c	11.93			9.79	
X1v	-12.08	-10.94	-11.55	-11.79	-10.48
X3v	-4.05	-4.38	-4.69	-4.82	-4.31
X5v	-1.61	-1.79	-2.16	-2.20	-1.65
X1c	5.17	4.42	3.18	2.88	4.19
X3c	5.54	6.10	3.64	3.47	4.49
X1c	12.28		10.85	10.58	
L1v	-12.26	-11.31	-11.83	-12.06	-10.84
L1v	-4.21	-4.67	-5.15	-5.21	-4.40
L3v	-0.62	-0.66	-0.85	-0.87	-0.64
L1c	4.16	4.23	2.91	2.63	3.79
L3c	8.88	8.72	6.70	6.36	7.31
L3v → L1c	4.78	4.89	3.76	3.50	4.43
X5v → X1c	6.78	6.21	5.34	5.08	5.84

^a Reference (42).

^b Reference (43, 44).

^c Reference (101).

^d Reference (98).

TABLE VII
CALCULATED ENERGIES AT HIGH SYMMETRY
POINTS FOR BULK ZnS

(All values are in electron volts and measured with
respect to the valence band maximum.)

Symmetry Point	FLCAO	OLCAO ^a	LCGO ^b	PVMB ^c	OPW ^d
G1v	-12.66	-12.27	-12.89	-13.06	-11.77
G15v(d)	-7.82		-6.4	-7.65	-14.1
G12v(d)	-7.45		-6.4	-7.27	
G15v	0.00	0.00	0.00	0.00	0.00
G1c	3.51	3.81	2.26	1.96	3.77
G15c	9.79	9.22	7.04	6.45	7.99
G1c	14.35			11.59	
X1v	-11.84	-10.80	-11.67	-11.88	-10.29
X3v	-3.67	-3.95	-4.49	-7.61	-3.93
X5v	-1.56	-1.57	-2.19	-2.30	-1.61
X1c	6.44	5.76	3.61	3.18	5.01
X3c	6.58	7.61	4.58	4.08	5.95
X1c	12.33		10.92	10.70	
L1v	-12.04	-11.18	-11.97	-12.17	-10.66
L1v	-4.00	-4.25	-5.20	-5.38	-4.20
L3v	-0.59	-0.56	-0.84	-0.94	-0.61
L1c	5.44	5.64	3.65	3.24	4.96
L3c	10.47	10.60	7.51	6.96	8.62
L3v → L1c	6.03	6.20	4.49	4.18	5.57
X5v → X1c	8.00	7.33	5.80	5.48	6.62

^a Reference (42).

^b Reference (43,44).

^c Reference (101).

^d Reference (98).

to note that some disparity also exists in the experimental data. Photoemission spectroscopy measurements on ZnSe (83,85), for example, differ by 0.6 eV for the L_{3v} state.

The TDOS for both bulk compounds were determined by using a sampling of the weighted k -points in 1/16 of the irreducible wedge of the first Brillouin zone shown in Figure 6 and was smoothed by a Gaussian function having a width of 0.15 eV at half maximum. Fifteen k -points were selected from each of the top, middle, and bottom triangular planes of the irreducible wedge. The scaling factors used to weight the symmetry points used in the calculations are listed in Table VIII. The resulting TDOS are in excellent agreement with those from other theoretical studies and the energy distribution curves from the x-ray and ultraviolet photoemission measurements. Thus, the *ab initio* nonself-consistent FLCAO method has been shown to be an effective tool in the determination of the electronic structure of bulk semiconductor compounds.

TABLE VIII
SCALING FACTOR OF THE k -POINTS
IN THE IRREDUCIBLE WEDGE

Top and Bottom Planes		Middle Plane	
k -Point	Weight	k -Point	Weight
Z or G	1/16	L	1/8
U or D	1/4	W	1/4
R or X	1/8	V	1/8
T or Y	1/4		
A or M	1/16		
S or S	1/4		

CHAPTER IV

THE $(\text{ZnSe})_m(\text{ZnS})_n$ SLS's

Introduction

Experimental studies on the $(\text{ZnSe})_m(\text{ZnS})_n$ SLS's have generally been confined to those having medium- to long-periods due to the difficulty in maintaining precise control over the number of monolayers during the growth process. For the long-period SLS's, a fluctuation in the number of monolayers would have a negligible impact on the electronic properties. A fluctuation in the number of monolayers for a short-period SLS, however, would lead to a non-uniformity of the electronic properties throughout the crystal superlattice. Theoretical calculations, on the other hand, have generally been limited to the short-period SLS's. The reason for this is that as the number of atoms in the unit cell becomes large, so to does the size of the energy matrix which needs to be diagonalized. Even for semi-empirical methods, where only the first few nearest neighbor interactions are considered and parameters are fitted to photoemission and reflectivity data from the bulk compounds, the size of the energy matrix presents an imposing problem. Thus, the difficulty in gaining an understanding of the nature of the $(\text{ZnSe})_m(\text{ZnS})_n$ SLS's has been the lack of corresponding experimental and theoretical results.

Present semi-empirical electronic structure studies consist of sp^3s^* tight-binding calculations by Bertho *et al* (91,110), Quiroga *et al* (111,112), and Wu *et al* (113). The work of Bertho *et al* involved the determination of the band offsets for ZnSe strained to ZnS and ZnS strained to ZnSe. For both configurations, the superlattice was determined to be type-I having a conduction band offset that was a small fraction of the average valence band offset ($\Delta E_C=38$ meV, $\Delta E_V=616$ meV for ZnSe strained to ZnS and $\Delta E_C=12$ meV, $\Delta E_V=640$ meV for ZnS

strained to ZnSe). The heavy- and light-hole states were determined to be localized in the ZnSe monolayers, while the lowest conduction state was delocalized all along the structure. The work of Quiroga *et al* involved the determination of the direct band gap energy and valence band offset for free-standing short- to long-period $(\text{ZnSe})_m(\text{ZnS})_{12}$ SLS's. For the short-period SLS's, the entire energy matrix was diagonalized. The medium- to long-period SLS's, however, required the use of the more approximate perturbative SETB method of Tejedor *et al* (114-116). Furthermore, all calculations were performed under the assumption of a vanishing conduction band offset. The results indicated a valence band offset near 1.0 eV and a localization of the heavy- and light-hole states in the ZnSe monolayers. The lowest conduction state was determined to be delocalized with roughly constant probability all along the structure. The resulting band gap energies converged to a value near 2.70 eV, which is less than the band gap of bulk ZnSe. The interpretation of the last two results is difficult, due to the assumed vanishing conduction band offset. Without any confinement, even a shallow well, it is hard to envision a possible localization of the lowest conduction state. A SLS band gap energy less than that of bulk ZnSe would indicate a transition from a type-I to a type-II superlattice, but such classifications only have meaning when the conduction band offset is non-vanishing. The work of Wu *et al* involved the determination of the direct band gap energy of the short-period $(\text{ZnSe})_m(\text{ZnS})_m$ SLS's for $m \leq 7$, where the SLS's were considered to be: grown on a GaAs substrate, grown on a GaP substrate, and free-standing. Assumed in these calculations was that the valence band offset remained constant at 0.82 eV. The resulting values suggested a transition from a type-I to type-II superlattice for the free-standing and GaP substrate cases with a further increase in the number of monolayers.

While semi-empirical calculations may offer insightful information on the $(\text{ZnSe})_m(\text{ZnS})_n$ SLS's, the accuracy of the results are restricted by: the consideration of only the first few nearest neighbor interactions, the treatment of the Zn 3d states as part of the core, and the fitting of the SLS parameters to experimental data of the bulk compounds. In the last case, such fitting cannot accurately describe the interface region. Thus, an accurate theoretical

description of the electronic structure for these SLS's can only be obtained from *ab initio* calculations. Present published *ab initio* calculations on the electronic band structure of the (001) short-period $(\text{ZnSe})_m(\text{ZnS})_m$ SLS's have been performed by Bernard and Zunger (101) for $m=1$ using the self-consistent PVMB method (117), Nakayama (118) for $m=1, 2,$ and 3 using a self-consistent pseudopotential (SCP) method (119), and by Marshall and Wilson (105) for $m=1$ using the nonself-consistent FLCAO method. The work of Bernard and Zunger was for the free-standing pseudobinary alloy Zn_2SeS , which goes to the $(\text{ZnSe})_1(\text{ZnS})_1$ SLS in the crystal limit. From the results, the following approximate correspondence relations at high symmetry points were shown to exist between the electronic band structures of the $(\text{ZnSe})_1(\text{ZnS})_1$ SLS (primitive tetragonal unit cell) and the bulk materials (primitive non-rectangular FCC unit cell):

$$\bar{\Gamma} \leftrightarrow \Gamma + X_z, \quad \bar{M} \leftrightarrow X_x + X_y, \quad \bar{R} \leftrightarrow L + L, \quad \text{and} \quad \bar{A} \leftrightarrow W + W, \quad (4.1)$$

where the states of the SLS are denoted by the bar. The correspondence relations are only approximate as the expected degeneracies from such foldings are removed due to: the anions in the SLS consist of both Se and S atoms and the reduction from cubic to tetragonal symmetry. In the work of Nakayama, both free-standing SLS's and SLS's grown on a GaAs substrate were considered. In both cases, the heavy- and light-hole states were determined to be more localized in the ZnSe monolayers, while the lowest conduction state showed no such localization. Furthermore, Nakayama suggested that the localization of the heavy- and light-hole states would become more distinct as the number of monolayers was increased. The valence band offset of the $(\text{ZnSe})_3(\text{ZnS})_3$ SLS was determined to be 0.746 for the free-standing case and 0.706 eV for the GaAs substrate case. In addition, the valence band offsets have been determined by Christensen *et al* (100,120,121) for $m=7$ using the frozen-potential approach (122) and by Qteish and Needs (94) using the model-solid theory of Van de Walle and Martin (123,124). In both studies, three configurations were considered: ZnSe strained to ZnS, ZnS strained to ZnSe, and a free-standing SLS. In the work of Christensen *et al*, an

electronic structure calculation was performed using the *ab initio* self-consistent LMTO method optimized for zincblende structures (125) to determine the self-consistent crystalline potential, which is constructed from an expansion of ACP's, at the band edge (i.e. the Γ -point). Primitive non-rectangular two-atom unit cells were then constructed from the lattice parameters of the middle strained ZnSe and ZnS monolayers. An electronic structure calculation at the band edge was then determined for each of the bulk-like compounds to determine the absolute energy of the VBM. In each case, the crystalline potential was constructed from ACP's taken from the middle strained monolayers. The resulting valence band offsets of the three configurations, determined from the expression

$$\Delta E_v^{\text{SLS}} = E_{\text{VBM}}^{\text{strained ZnS}} - E_{\text{VBM}}^{\text{strained ZnSe}}, \quad (4.2)$$

were: 0.24 eV for ZnSe strained to ZnS, 0.65 eV for ZnS strained to ZnSe, and 0.54 eV for the free-standing SLS. In the work of Qteish and Needs, an electronic structure calculation was performed using a SCP method (126) to determine the self-consistent crystalline potential at high symmetry points. From the crystalline potential, the average potentials \bar{V}_{ZnSe} and \bar{V}_{ZnS} were determined for, respectively, the ZnSe and ZnS monolayers. An electronic structure calculation, equivalent to those of Christensen *et al*, were then performed for each bulk-like compound to determine the energy of the VBM with respect to the average potential. The resulting valence band offsets of the three configurations, determined from the expression

$$\Delta E_v^{\text{SLS}} = [E_{\text{VBM}}^{\text{strained ZnS}} - E_{\text{VBM}}^{\text{strained ZnSe}}] + [\bar{V}_{\text{ZnS}} - \bar{V}_{\text{ZnSe}}], \quad (4.3)$$

were: 0.52 eV for ZnS strained to ZnSe, 0.90 eV for ZnSe strained to ZnS, and 0.72 eV for the free-standing SLS. In principle, Eq. (4.2) and (4.3) are equivalent and should yield equivalent values for the valence band offsets. The reason for the large discrepancy between values is a much debated issue and centers on the importance of the Zn 3d states, which were treated as fully relaxed states in the LMTO calculations. The present *ab initio* calculations, restricted to the short-period $(\text{ZnSe})_m(\text{ZnS})_m$ SLS's, offer only a limited understanding of the electronic structure of these SLS's. For $m \leq 3$, the band gap was determined to be direct, the heavy- and

light-holes more localized in the ZnSe monolayers, and the lowest conduction state delocalized. However, the band gap energy as a function of the number of monolayers is still unknown. Whether the localization of the heavy- and light-hole states becomes more distinct, as suggested by Nakayama, and in which monolayers of ZnSe this localization occurs has yet to be determined. In addition, a further study of the lowest conduction is needed to determine if localization occurs, which is required for an efficient blue LED, as the number of monolayers is increased. Such studies using *ab initio* self-consistent calculations would be difficult due to the number of iterations (~5) necessary to reach self-consistency. Coupled with an increasing size of the energy matrix, such calculations would require a impractical amount of computational time. Thus, *ab initio* nonself-consistent calculations offer an attractive alternative. The *ab initio* nonself-consistent FLCAO method was shown in the previous chapter to yield one-electron energy eigenvalues for bulk ZnSe and ZnS which were in good agreement with those from self-consistent calculations and experimental studies. Thus, it is assumed that this agreement will also carry over to the $(\text{ZnSe})_m(\text{ZnS})_n$ SLS's.

Elastic Strain

The elastic strain acts to deform the crystal superlattice structure by distorting the nearest-neighbor bond lengths and angles from their bulk values. The hydrostatic contribution modifies the electronic band structure, which has a direct effect on the size of the band gap and could induce a transition from a direct band gap to a indirect one. The uniaxial contribution breaks the three-fold degeneracy (heavy-hole, light-hole, and split-off states) of the valence band maximum (VBM) found in both bulk ZnSe and ZnS. The strained ZnSe monolayers experience a biaxial compression, where the compressive hydrostatic contribution is expected to cause a band gap opening and the breaking of the three-fold degeneracy by the tensile uniaxial contribution is expected to leave the heavy-hole state as the VBM. The strained ZnS monolayers experience the opposite from the elastic strain, a biaxial tension, so that the tensile hydrostatic contribution is expected to cause a band gap lowering and the breaking of the three-

fold degeneracy by the compressive uniaxial contribution is expected to leave the light-hole state as the VBM (91).

As a result of the presence of elastic strain in the superlattice structure, each set of m, n values requires a determination of the superlattice constants: the lattice constant perpendicular to the (001) growth direction and the interatomic distances parallel to the growth direction. The lattice constant perpendicular to the growth direction a_{xy} is common to both of the constituent compounds and will assume a value between the bulk lattice constants. A much used approximation for a_{xy} is the linear expression

$$a_{xy} = \frac{ma_{\text{ZnSe}} + na_{\text{ZnS}}}{m + n} \quad (4.4)$$

where it can be seen that a_{xy} will approach the bulk lattice constant of one compound if the number of monolayers of that compound is much larger than the other. However, the only possibility of a_{xy} being equal to the bulk value is for the strain to be broken. Along the growth direction, there will be m number of interatomic distances $d_{\text{Zn-Se}} [i]$ between nearest-neighbors for the ZnSe monolayers and n number of interatomic distances $d_{\text{Zn-S}} [j]$ between nearest-neighbors for the ZnS monolayers, as is shown in Figure 10. In general, the interatomic distances are expected to vary only for the first few monolayers and then converge to some constant value, which is not equal to the bulk value, in the middle layers. As with a_{xy} , $d_{\text{Zn-Se}} [i]$ or $d_{\text{Zn-S}} [j]$ can only equal the bulk value if the elastic strain is broken.

As with most *ab initio* calculations on SLS's, the lattice constants of the $(\text{ZnSe})_m(\text{ZnS})_n$ SLS's were determined in this work through use of the Valence Force Field (VFF) (127) or Keating model (128,229), where the deformation energy is given by

$$U_d = \sum_{\langle \ell, m \rangle} \frac{3}{8d_{\ell m}^2} \alpha_{\ell m} (\mathbf{r}_{\ell m} \cdot \mathbf{r}_{\ell m} - d_{\ell m}^2)^2 + \sum_{\langle \ell, m, n \rangle} \frac{3}{8d_{\ell mn}^2} \beta_{\ell mn} \left(\mathbf{r}_{\ell m} \cdot \mathbf{r}_{mn} + \frac{d_{\ell mn}^2}{3} \right)^2 \quad (4.5)$$

In this expression: the sums are over the four nearest-neighbors of the ℓ th atom, $d'_{\ell m}$ is the equilibrium bulk nearest-neighbor interatomic distance (2.454 Å for ZnSe and 2.342 Å for

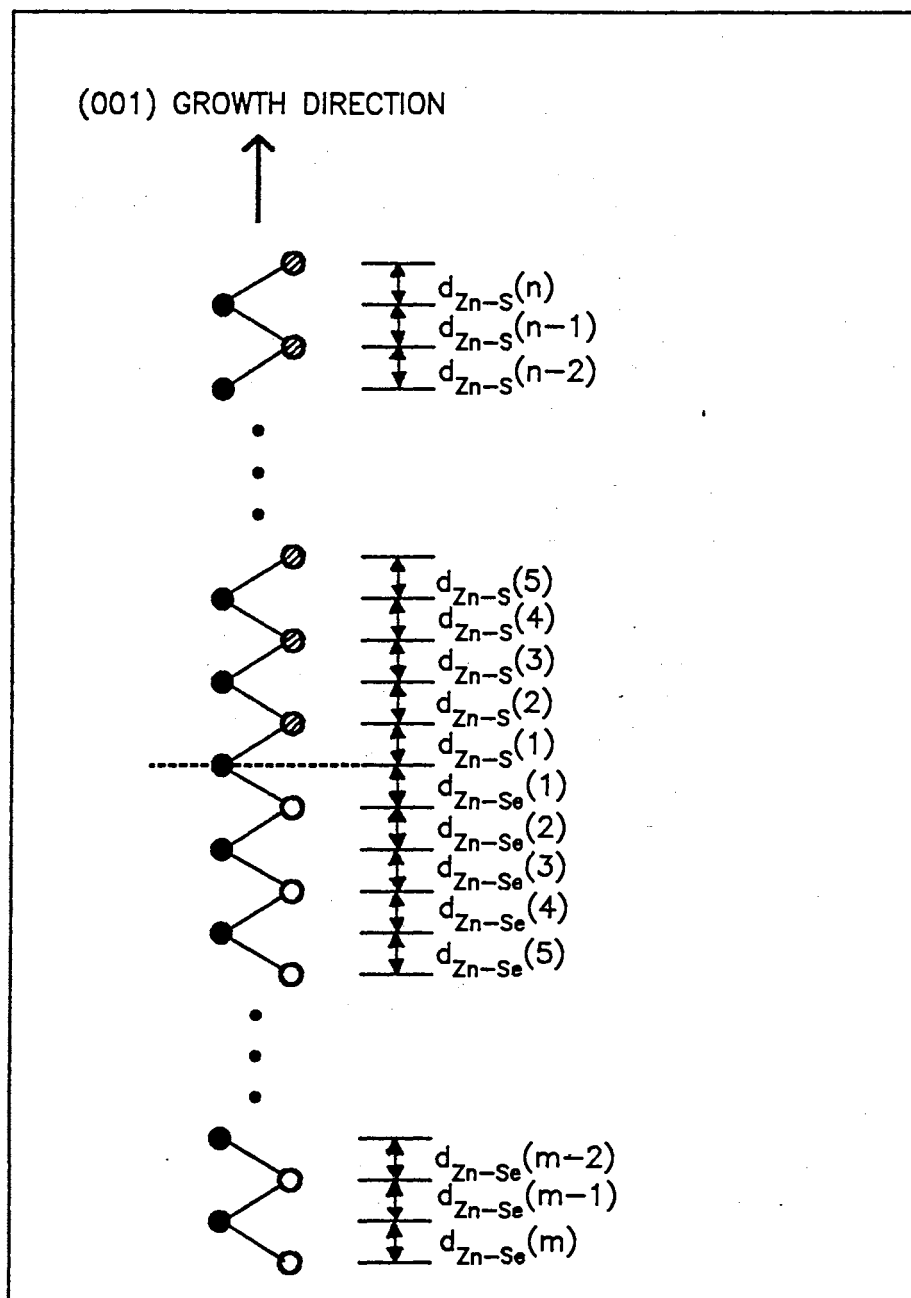


Figure 10. The $m+n$ unique interatomic distances along the (001) growth direction for the $(\text{ZnSe})_m(\text{ZnS})_n$ SLS.

ZnS), $\alpha_{\ell m}$ is the bulk bond-stretching force constant (35.24 N/m for ZnSe and 44.92 N/m for ZnS), and $\beta_{\ell m}$ is the bulk bond-bending force constant (4.23 N/m for ZnSe and 4.78 N/m for ZnS). The stable superlattice structure is then obtained by determining the set of vectors $\mathbf{r}_{\ell m}$ connecting the ℓ th and m th nearest-neighbor atoms in the SLS that give the minimum deformation energy. If it is assumed, as was suggested by Nakayama, that the expressions

$$d'_{\text{Zn-Se-S}}^2 \approx d'_{\text{ZnSe}} \cdot d'_{\text{ZnS}} \quad \text{and} \quad \beta_{\text{Zn-Se-S}} \approx (\beta_{\text{ZnSe}} + \beta_{\text{ZnS}}) / 2 \quad (4.6)$$

adequately describe the parameters at the interface, then the expression for the deformation energy can be rewritten as

$$\begin{aligned} U_d = & \frac{3\alpha_{\text{ZnSe}}}{d'^2_{\text{ZnSe}}} \sum_{i=1}^m (a_{xy}^2 + d'_{\text{Zn-Se}}[i] - d'_{\text{ZnSe}})^2 + \frac{3\alpha_{\text{ZnS}}}{d'^2_{\text{ZnS}}} \sum_{j=1}^n (a_{xy}^2 + d'_{\text{Zn-S}}[j] - d'_{\text{ZnS}})^2 \\ & + \frac{3\beta_{\text{ZnSe}}}{d'^2_{\text{ZnSe}}} \sum_{i=1}^m (-a_{xy}^2 / 2 + d'_{\text{Zn-Se}}[i] + d'_{\text{ZnSe}} / 3)^2 + \frac{3\beta_{\text{ZnS}}}{d'^2_{\text{ZnS}}} \sum_{j=1}^n (-a_{xy}^2 / 2 + d'_{\text{Zn-S}}[j] + d'_{\text{ZnS}} / 3)^2 \\ & + \frac{6\beta_{\text{ZnSe}}}{d'^2_{\text{ZnSe}}} \sum_{i=1}^{m-1} (-d'_{\text{Zn-Se}}[i]d'_{\text{Zn-Se}}[i+1] + d'_{\text{ZnSe}} / 3)^2 \\ & + \frac{6\beta_{\text{ZnS}}}{d'^2_{\text{ZnS}}} \sum_{j=1}^{n-1} (-d'_{\text{Zn-S}}[j]d'_{\text{Zn-S}}[j+1] + d'_{\text{ZnS}} / 3)^2 \\ & + \frac{3\beta_{\text{ZnSe}}}{d'^2_{\text{ZnSe}}} (-d'_{\text{Zn-Se}}[m] + d'_{\text{ZnSe}} / 3)^2 + \frac{3\beta_{\text{ZnS}}}{d'^2_{\text{ZnS}}} (-d'_{\text{Zn-S}}[n] + d'_{\text{ZnS}} / 3)^2 \\ & + \frac{3(\beta_{\text{ZnSe}} + \beta_{\text{ZnS}})}{d'_{\text{ZnSe}} d'_{\text{ZnS}}} (-d'_{\text{Zn-Se}}[1]d'_{\text{Zn-S}}[1] + d'_{\text{ZnSe}} d'_{\text{ZnS}} / 3)^2. \end{aligned} \quad (4.7)$$

A substrate, assuming its thickness is much greater than the thickness of either compound, can easily be incorporated into this expression by setting a_{xy} equal to the lattice constant of the substrate. This would allow for one variable to be eliminated from the above expression, resulting in a reduction of computational time needed for the calculation. In this work, however,

the SLS's were considered to be free-standing. The values of the lattice constant perpendicular to the growth direction and the interatomic distances along the growth direction for the $(\text{ZnSe})_m(\text{ZnS})_n$ SLS's for $m=1, 2$, and $m \geq 3$ and the $(\text{ZnSe})_5(\text{ZnS})_n$ SLS's for $n=5$ and 9 are given in Table IX. The values are in excellent agreement with those determined by Nakayama and Bernard and Zunger using the VFF model.

The *ab initio* calculations on the electronic structure of the $(\text{ZnSe})_m(\text{ZnS})_n$ SLS's presented in this thesis were performed using a primitive tetragonal unit cell, where each monolayer was represented by a single cation (Zn atom) and a single anion (Se or S atom). To maintain the periodicity of the crystal superlattice structure required the unit cell to be constructed from one period of the SLS (containing two interfaces) if $m+n$ was even and two periods of the SLS (containing three interfaces) if $m+n$ was odd. To keep the size of the energy matrix and the amount of required CPU time for its diagonalization within practical limits, only SLS's in which $m+n$ was even were considered. For $m, n \geq 4$, seven unique atomic configurations were considered: Zn at the interfaces, Zn between Se layers, Zn between S layers, Se next to the Zn interface layer, Se between Zn layers in which neither Zn layer was the interface, S next to the Zn interface layer, and S between Zn layers. Such distinctions were made for the purpose of identifying the localization of states to a particular layer through a orbital composition analysis. The primitive lattice vectors of the unit cell are given by

$$\mathbf{A}_1 = (a_{xy} / 2)(1, 1, 0), \quad \mathbf{A}_2 = (a_{xy} / 2)(1, -1, 0), \quad \text{and} \quad \mathbf{A}_3 = a_z(0, 0, 1), \quad (4.8)$$

where

$$a_z = 2 \left(\sum_{i=1}^m d_{\text{Zn-Se}} [i] + \sum_{j=1}^n d_{\text{Zn-S}} [j] \right). \quad (4.9)$$

The positions of the atoms contained within the unit cell structure are dependent on the nature of the m, n values. For m, n both odd, the atomic positions are: the two Zn atoms representing the interfaces are located at

$$\mathbf{t}_{11} = (0, 0, 0) \quad \text{and} \quad \mathbf{t}_{12} = (a_{xy} / 2, a_{xy} / 2, 2D_{\text{Zn-Se}}); \quad (4.10)$$

TABLE IX
LATTICE CONSTANTS FOR THE
(ZnSe)_m(ZnS)_n SLS's

(ZnSe) ₁ (ZnS) ₁ SLS	
Lattice Constant	Value (a.u.)
axy	5.2200
dZn-Se(1)	2.7701
dZn-S(1)	2.4721
(ZnSe) ₂ (ZnS) ₂	
Lattice Constant	Value (a.u.)
axy	5.2196
dZn-Se(2)	2.7620
dZn-Se(1)	2.7707
dZn-S(1)	2.4721
dZn-S(2)	2.4795
(ZnSe) _m (ZnS) _m for m ≥ 3	
Lattice Constant	Value (a.u.)
axy	5.2194
dZn-Se(m ≥ 3)	2.7626
dZn-Se(2)	2.7620
dZn-Se(1)	2.7709
dZn-S(1)	2.4721
dZn-S(2)	2.4797
dZn-S(m ≥ 3)	2.4795

TABLE IX (Continued)

(ZnSe) ₅ (ZnS) ₇ SLS	
Lattice Constant	Value (a.u.)
a _{xy}	5.1996
d _{Zn-Se(m ≥ 3)}	2.7747
d _{Zn-Se(2)}	2.7741
d _{Zn-Se(1)}	2.7830
d _{Zn-S(1)}	2.4863
d _{Zn-S(2)}	2.4939
d _{Zn-S(n ≥ 3)}	2.4935

(ZnSe) ₅ (ZnS) ₉ SLS	
Lattice Constant	Value (a.u.)
a _{xy}	5.1859
d _{Zn-Se(m ≥ 3)}	2.7828
d _{Zn-Se(2)}	2.7824
d _{Zn-Se(1)}	2.7911
d _{Zn-S(1)}	2.4959
d _{Zn-S(2)}	2.5033
d _{Zn-S(n ≥ 3)}	2.5031

the $m-1$ Zn atoms between the Se layers are located at

$$\begin{aligned} \mathbf{t}_{2,1} &= (a_{xy} / 2, a_{xy} / 2, \sum_{i=1}^2 d_{Zn-Se} [i]), \quad \mathbf{t}_{2,2} = (0, 0, \sum_{i=1}^4 d_{Zn-Se} [i]), \quad \dots, \\ \text{and } \mathbf{t}_{2,m-1} &= (0, 0, D_{Zn-Se} + \sum_{i=3}^m d_{Zn-Se} [i]); \end{aligned} \quad (4.11)$$

the $n-1$ Zn atoms between the S layers are located at

$$\begin{aligned} \mathbf{t}_{3,1} &= (0, 0, 2D_{Zn-Se} + \sum_{j=1}^2 d_{Zn-S} [j]), \quad \mathbf{t}_{3,2} = (a_{xy} / 2, a_{xy} / 2, 2D_{Zn-S} + \sum_{j=1}^4 d_{Zn-S} [j]), \quad \dots, \\ \text{and } \mathbf{t}_{3,n-1} &= (a_{xy} / 2, a_{xy} / 2, 2D_{Zn-Se} + D_{Zn-S} + \sum_{j=3}^n d_{Zn-S} [j]); \end{aligned} \quad (4.12)$$

the two Se atoms representing the Se layers next to the interfaces are located at

$$\begin{aligned} \mathbf{t}_{4,1} &= (a_{xy} / 4, a_{xy} / 4, d_{Zn-Se} [1]) \quad \text{and} \\ \mathbf{t}_{4,2} &= (a_{xy} / 4, a_{xy} / 4, D_{Zn-Se} + \sum_{i=2}^m d_{Zn-Se} [i]); \end{aligned} \quad (4.13)$$

the $m-2$ Se atoms between Zn layers are located at

$$\begin{aligned} \mathbf{t}_{5,1} &= (a_{xy} / 4, -a_{xy} / 4, \sum_{i=1}^3 d_{Zn-Se} [i]), \quad \mathbf{t}_{5,2} = (a_{xy} / 4, a_{xy} / 4, \sum_{i=1}^5 d_{Zn-Se} [i]), \quad \dots, \\ \text{and } \mathbf{t}_{5,m-1} &= (a_{xy} / 4, -a_{xy} / 4, D_{Zn-Se} + \sum_{i=4}^m d_{Zn-Se} [i]); \end{aligned} \quad (4.14)$$

the two S atoms representing the S layers next to the interfaces are located at

$$\begin{aligned} \mathbf{t}_{6,1} &= (a_{xy} / 4, -a_{xy} / 4, 2D_{Zn-Se} + d_{Zn-S} [1]) \quad \text{and} \\ \mathbf{t}_{6,2} &= (a_{xy} / 4, -a_{xy} / 4, 2D_{Zn-Se} + D_{Zn-S} + \sum_{j=2}^n d_{Zn-S} [j]); \end{aligned} \quad (4.15)$$

and the $n-2$ S atoms between Zn layers are located at

$$\begin{aligned} \mathbf{t}_{7,1} &= (a_{xy} / 4, a_{xy} / 4, 2D_{Zn-Se} + \sum_{j=1}^3 d_{Zn-S} [j]), \quad \mathbf{t}_{7,2} = (a_{xy} / 4, -a_{xy} / 4, 2D_{Zn-Se} + \sum_{j=1}^5 d_{Zn-S} [j]), \quad \dots, \\ \text{and } \mathbf{t}_{7,n-1} &= (a_{xy} / 4, a_{xy} / 4, 2D_{Zn-Se} + D_{Zn-S} + \sum_{j=4}^n d_{Zn-S} [j]). \end{aligned} \quad (4.16)$$

For m, n both even, the atomic positions are: the two Zn atoms representing the interfaces are

located at

$$\mathbf{t}_{1,1} = (0, 0, 0) \text{ and } \mathbf{t}_{1,2} = (0, 0, 2D_{\text{Zn-Se}}); \quad (4.17)$$

the $m-1$ Zn atoms between the Se layers are located at

$$\begin{aligned} \mathbf{t}_{2,1} &= (a_{xy} / 2, a_{xy} / 2, \sum_{i=1}^2 d_{\text{Zn-Se}} [i]), \quad \mathbf{t}_{2,2} = (0, 0, \sum_{i=1}^4 d_{\text{Zn-Se}} [i]), \quad \dots, \\ \text{and } \mathbf{t}_{2,m-1} &= (a_{xy} / 2, a_{xy} / 2, D_{\text{Zn-Se}} + \sum_{i=3}^m d_{\text{Zn-Se}} [i]); \end{aligned} \quad (4.18)$$

the $n-1$ Zn atoms between the S layers are located at

$$\begin{aligned} \mathbf{t}_{3,1} &= (a_{xy} / 2, a_{xy} / 2, 2D_{\text{Zn-Se}} + \sum_{j=1}^2 d_{\text{Zn-S}} [j]), \quad \mathbf{t}_{3,2} = (0, 0, 2D_{\text{Zn-S}} + \sum_{j=1}^4 d_{\text{Zn-S}} [j]), \quad \dots, \\ \text{and } \mathbf{t}_{3,n-1} &= (a_{xy} / 2, a_{xy} / 2, 2D_{\text{Zn-Se}} + D_{\text{Zn-S}} + \sum_{j=3}^n d_{\text{Zn-S}} [j]); \end{aligned} \quad (4.19)$$

the two Se atoms representing the Se layers next to the interfaces are located at

$$\begin{aligned} \mathbf{t}_{4,1} &= (a_{xy} / 4, a_{xy} / 4, d_{\text{Zn-Se}} [1]) \text{ and} \\ \mathbf{t}_{4,2} &= (a_{xy} / 4, -a_{xy} / 4, D_{\text{Zn-Se}} + \sum_{i=2}^m d_{\text{Zn-Se}} [i]); \end{aligned} \quad (4.20)$$

the $m-2$ Se atoms between Zn layers are located at

$$\begin{aligned} \mathbf{t}_{5,1} &= (a_{xy} / 4, -a_{xy} / 4, \sum_{i=1}^3 d_{\text{Zn-Se}} [i]), \quad \mathbf{t}_{5,2} = (a_{xy} / 4, a_{xy} / 4, \sum_{i=1}^5 d_{\text{Zn-Se}} [i]), \quad \dots, \\ \text{and } \mathbf{t}_{5,m-1} &= (a_{xy} / 4, a_{xy} / 4, D_{\text{Zn-Se}} + \sum_{i=4}^m d_{\text{Zn-Se}} [i]); \end{aligned} \quad (4.21)$$

the two S atoms representing the S layers next to the interfaces are located at

$$\begin{aligned} \mathbf{t}_{6,1} &= (a_{xy} / 4, a_{xy} / 4, 2D_{\text{Zn-Se}} + d_{\text{Zn-S}} [1]) \text{ and} \\ \mathbf{t}_{6,2} &= (a_{xy} / 4, -a_{xy} / 4, 2D_{\text{Zn-Se}} + D_{\text{Zn-S}} + \sum_{j=2}^n d_{\text{Zn-S}} [j]); \end{aligned} \quad (4.22)$$

and the $n-2$ S atoms between Zn layers are located at

$$\mathbf{t}_{7,1} = (a_{xy} / 4, -a_{xy} / 4, 2D_{\text{Zn-Se}} + \sum_{j=1}^3 d_{\text{Zn-S}} [j]), \quad \mathbf{t}_{7,2} = (a_{xy} / 4, a_{xy} / 4, 2D_{\text{Zn-Se}} + \sum_{j=1}^5 d_{\text{Zn-S}} [j]), \quad \dots,$$

$$\text{and } \mathbf{t}_{7,n-1} = (a_{xy} / 4, a_{xy} / 4, 2D_{\text{Zn-Se}} + D_{\text{Zn-S}} + \sum_{j=4}^n d_{\text{Zn-S}} [j]). \quad (4.23)$$

In the above expressions,

$$D_{\text{Zn-Se}} = \sum_{i=1}^m d_{\text{Zn-Se}} [i] \quad \text{and} \quad D_{\text{Zn-S}} = \sum_{j=1}^n d_{\text{Zn-S}} [j] \quad (4.24)$$

so that $2D_{\text{Zn-Se}}$ and $2D_{\text{Zn-S}}$ represent, respectively, the thickness of the ZnSe and ZnS compounds used in the construction of the SLS.

Electronic Band Structure And Density Of States

An immediate problem presented to *ab initio* LCAO electronic structure calculations of the $(\text{ZnSe})_m(\text{ZnS})_n$ SLS's is the treatment of the crystalline potential. Because the elastic strain is a function of the number of monolayers, every change in the m, n values requires a redetermination of the crystalline potential or crystalline charge density. This is paramount for the ultra short-period SLS's, where each monolayer will have interactions with the interface. In their study on bulk semiconductor compounds, Huang and Ching (42) suggested that the bulk crystalline potentials could be used directly in the SLS calculations. This is possible for self-consistent calculations, where the corrections to the crystalline potential to account for the charge transfer at the interface will be made during the iterations towards self-consistency. For nonself-consistent calculations, though, it is necessary to include the effects of the interface in the initial crystalline potential. On the other hand, it would impractical to generate a non-linear least-squares fit to the crystalline potential for each set of m, n values. Instead, the non-linear coefficients from the ACP's of the bulk fits were held frozen and only the linear coefficients were adjusted to describe the change in the crystalline potential brought about by the interface. For the $(\text{ZnSe})_1(\text{ZnS})_1$ SLS, two potential fits were performed. The first fit used the non-linear

coefficients from the ACP's at the Zn sites in ZnS for the non-linear coefficients of the ACP's at the Zn interfacial sites, while the second fit used the non-linear coefficients from the ACP's at the Zn sites in ZnSe. The latter fit gave a better root-mean-square error and was chosen to represent the SLS crystalline potential. For all other fits to the crystalline potential of the $(\text{ZnSe})_m(\text{ZnS})_n$ SLS's, the non-linear coefficients for the ACP's at the Zn interfacial sites were also selected from the ACP's at the Zn site in ZnSe. For $m, n = 2$ and 3 , the linear coefficients were determined for five unique ACP's located at the: Zn sites at the interface, Zn sites between Se layers, Zn sites between S layers, Se sites, and S sites. For $m, n \geq 4$, the ACP's located at the Se and S sites were further categorized as either Se and S sites next to or away from the interfaces, resulting in a total of seven unique ACP's. The adjusted linear coefficients from these fits are listed in Table X. In all of the fits, more weight was given to the monolayers adjacent to the interfaces than the middle monolayers.

The bases used in the bulk ZnSe and ZnS calculations were transferred directly over for use in the SLS calculations, as was first suggested by Huang and Ching. The justification for using the bulk core-like basis functions is straightforward. While the SLS lattice constant perpendicular to the growth directions and the nearest-neighbor interatomic distances parallel to the growth direction are changed significantly from their bulk values (<4%), the nearest-neighbor bond lengths in going from the bulk materials to the SLS's change only slightly (<1%). Thus, there will not be any new significant overlap contributions from there being nearby orbitals present.

The density of states of the SLS's were determined by using a sampling of the weighted k -points in 1/16 of the irreducible wedge of the first Brillouin zone shown in Figure 6 and was smoothed by a Gaussian function having a width of 0.15 eV at half maximum. For $m, n \leq 3$, fifteen k -points were selected from each of the top, middle, and bottom triangular planes of the irreducible wedge. As the number of monolayers in the unit cell increases, the axis vector $\mathbf{b}_3 = 2\pi / a_z$ of the reciprocal lattice decreases. For $m, n \geq 3$, no dispersion of the

TABLE X
ADJUSTED LINEAR COEFFICIENTS FOR THE
ACP'S OF THE $(\text{ZnSe})_m(\text{ZnS})_n$ SLS's

m,n = 1				
	Zinc	Selenium	Sulfur	
	-0.3344130	0.0071650	0.0462053	
	-0.7216690	-1.0512100	-0.7873360	
	-3.9561800	-3.9062600	-3.1684000	
	-15.620200	-13.873800	-7.2926100	
	-45.270300	-46.791200	-22.592100	
	-91.853900	-101.53600	-43.260000	
	-193.05400	-215.54500	-96.446700	
	-347.49700	-401.38800	-165.41300	
	-679.37100	-770.33800	-329.76800	
	930.59500	1078.3800	439.67800	
m,n = 2				
Zinc at the Interfaces	Zinc Between Se Layers	Zinc Between S Layers	Selenium	Sulfur
-0.3221730	-0.3408550	-0.3678810	0.0089678	0.0027071
-0.7560420	-0.7017750	-0.8456580	-1.0678300	-0.7372270
-3.8650900	-3.9876400	-4.5144700	-3.8803300	-3.2529300
-15.783200	-15.568200	-17.083700	-13.933100	-7.1644000
-44.997400	-45.358800	-47.044000	-46.680700	-22.794700
-92.308500	-91.705000	-94.094800	-101.72800	-42.927600
-192.30100	-193.30200	-194.61200	-215.21900	-96.996700
-348.72100	-347.09500	-347.84000	-401.92600	-164.51900
-677.54500	-679.97100	-666.13400	-769.51800	-331.10600
928.66200	931.23100	939.03100	1077.4900	441.10300

TABLE X (Continued)

m,n = 3				
Zinc at the Interfaces	Zinc Between Se Layers	Zinc Between S Layers	Selenium	Sulfur
-0.3078030	-0.3164280	-0.3941050	0.0044281	0.0043127
-0.7542780	-0.7037690	-0.7963200	-1.0789200	-0.7603780
-3.8666100	-4.0748000	-4.6675600	-3.8507800	-3.2339600
-15.828300	-15.308500	-16.698500	-13.963500	-7.1234900
-44.881400	-45.868700	-47.775600	-46.647300	-22.915000
-92.523200	-90.817400	-92.836400	-101.77500	-42.700700
-191.93400	-194.79200	-196.70600	-215.14600	-97.385400
-349.32000	-344.66900	-344.46000	-402.04400	-163.88200
-676.65000	-683.59400	-671.11900	-769.33900	-332.06300
927.71300	935.06800	944.21300	1077.2900	442.12200

TABLE X (Continued)

m,n = 4

Zinc at the Interfaces	Zinc Between Se Layers	Zinc Between S Layers	Selenium Next to the Interfaces	Selenium Away from the Interfaces	Sulfur Next to the Interfaces	Sulfur Away from the Interfaces
-0.3222370	-0.3297470	-0.3810150	0.0013412	0.0039731	0.0086201	-0.0097228
-0.7363060	-0.7015570	-0.8152750	-1.0591800	-1.0748400	-0.7519210	-0.7395890
-3.9121300	-4.0067600	-4.5801200	-3.8850000	-3.8456900	-3.2028200	-3.2651600
-15.711400	-15.522200	-16.943300	-13.924900	-13.983100	-7.2619900	-7.0893100
-45.112200	-45.450500	-47.301000	-46.715400	-46.619800	-22.639000	-22.915000
-92.117800	-91.541500	-93.655300	-101.64900	-101.81100	-43.176300	-42.618700
-192.61700	-193.57900	-195.34300	-215.36400	-215.07800	-96.589700	-97.528000
-348.20700	-346.64300	-346.66100	-401.68200	-402.28100	-165.17900	-163.62600
-678.31200	-680.64700	-667.87300	-769.89200	-768.84900	-330.12000	-332.54300
929.47400	931.94600	940.83800	1077.8900	1076.7500	440.05300	442.34000

TABLE X (Continued)

m,n = 5

Zinc at the Interfaces	Zinc Between Se Layers	Zinc Between S Layers		Selenium Next to the Interfaces	Selenium Away from the Interfaces	Sulfur Next to the Interfaces	Sulfur Away from the Interfaces
-0.3271870	-0.3490500	-0.3623780		0.0086176	0.0015526	0.0007790	-0.0141629
-0.7104090	-0.6870940	-0.8564440		-1.0646300	-1.0510200	-0.7415370	-0.7416350
-3.9749300	-4.0751600	-4.5572200		-3.8739500	-3.9332400	-3.2344300	-3.2829000
-15.594300	-15.318700	-16.882400		-13.949100	-13.799350	-7.1877000	-7.0348200
-45.308900	-45.846700	-47.469100		-46.651400	-46.978600	-22.764000	-23.071100
-91.791800	-90.856400	-93.345000		-101.77800	-101.17600	-42.974100	-42.437900
-193.15700	-194.72600	-195.86800		-215.13600	-216.14900	-96.921500	-97.838900
-347.33200	-344.77600	-345.81000		-402.06200	-400.65000	-164.64100	-163.09600
-679.61800	-683.43400	-669.13000		-769.31000	-771.19300	-330.92400	-333.43200
930.85600	934.89800	942.14600		1077.2600	1079.3100	440.90900	443.00700

TABLE X (Continued)

m,n = 6

Zinc at the Interfaces	Zinc Between Se Layers	Zinc Between S Layers	Selenium Next to the Interfaces	Selenium Away from the Interfaces	Sulfur Next to the Interfaces	Sulfur Away from the Interfaces
-0.3073020	-0.3236390	-0.3347490	-0.0044120	0.0014836	-0.0099557	-0.0241135
-0.7268170	-0.7140880	-0.8991340	-1.0687800	-1.0612600	-0.7470580	-0.7511170
-3.9473700	-4.0366600	-4.4843300	-3.8556700	-3.9039000	-3.2185100	-3.2674900
-15.645100	-15.382400	-17.005400	-13.985400	-13.843300	-7.2155400	-7.0401400
-45.226800	-45.740700	-47.264900	-46.667000	-46.978600	-22.726200	-23.093000
-91.924500	-91.032900	-93.683300	-101.70000	-101.16300	-43.028200	-42.414600
-192.93900	-194.43300	-195.31100	-215.23200	-216.08600	-96.836600	-97.886000
-347.68400	-345.25100	-346.70700	-401.91400	-400.75900	-164.77700	-162.93500
-679.09300	-682.72500	-667.80800	-769.53200	-771.04300	-330.72200	-333.74300
930.30000	934.14700	940.77200	1077.5000	1079.1500	440.69400	443.36600

TABLE X (Continued)

m,n = 7

Zinc at the Interfaces	Zinc Between Se Layers	Zinc Between S Layers		Selenium Next to the Interfaces	Selenium Away from the Interfaces	Sulfur Next to the Interfaces	Sulfur Away from the Interfaces
-0.3269910	-0.3494250	-0.3620110		0.0087442	0.0156404	0.0003724	-0.0138847
-0.7104290	-0.6862870	-0.8580000		-1.0648900	-1.0512200	-0.7409320	-0.7427640
-3.9749800	-4.0766200	-4.5550400		-3.8725400	-3.9313900	-3.2354000	-3.2813900
-15.594100	-15.316400	-16.885400		-13.959900	-13.805500	-7.1860500	-7.0370000
-45.309300	-45.850400	-47.464800		-46.696500	-47.022200	-22.766800	-23.067600
-91.791100	-90.850400	-93.351900		-101.66200	-101.06200	-42.969400	-42.443700
-193.15800	-194.73600	-195.85700		-215.29000	-216.30000	-96.929300	-97.829300
-347.33000	-344.76000	-345.82800		-401.82100	-400.41600	-164.62800	-163.11100
-679.62000	-683.45800	-669.10400		-769.67400	-771.54300	-330.94300	-333.40900
930.85900	934.92300	942.11800		1077.6500	1079.6900	440.92900	442.98200

TABLE X (Continued)

m=5, n=7

Zinc at the Interfaces	Zinc Between Se Layers	Zinc Between S Layers		Selenium Next to the Interfaces	Selenium Away from the Interfaces	Sulfur Next to the Interfaces	Sulfur Away from the Interfaces
-0.3264350	-0.3495320	-0.3629840		0.0094640	0.0165995	0.0007031	-0.0129227
-0.7110510	-0.6878080	-0.8553400		-1.0649700	-1.0493500	-0.7411800	-0.7436380
-3.9733800	-4.0695500	-4.5581200		-3.8732000	-3.9387800	-3.2339100	-3.2789800
-15.598500	-15.333700	-16.885000		-13.958600	-13.789300	-7.1890400	-7.0407100
-45.301100	-45.818800	-47.462700		-46.698900	-47.051500	-22.761700	-23.061400
-91.805000	-90.904200	-93.356600		-101.65800	-101.01500	-42.978000	-42.457600
-193.13400	-194.64600	-195.84800		-215.29700	-216.36900	-96.914900	-97.796300
-347.36700	-344.90500	-345.84100		-401.80900	-400.34300	-164.65200	-163.20700
-679.56400	-683.24100	-669.08400		-769.69100	-771.72800	-330.90800	-333.03100
930.80000	934.69300	942.09800		1077.6700	1080.0400	440.89200	442.16800

TABLE X (Continued)

m=5, n=9

Zinc at the Interfaces	Zinc Between Se Layers	Zinc Between S Layers		Selenium Next to the Interfaces	Selenium Away from the Interfaces	Sulfur Next to the Interfaces	Sulfur Away from the Interfaces
-0.3075430	-0.3267660	-0.3377590		-0.0021283	0.0046577	-0.0094160	-0.0210336
-0.7249670	-0.7113120	-0.8931550		-1.0687200	-1.0582500	-0.7471920	-0.7563950
-3.9507200	-4.0353100	-4.4943300		-3.8573600	-3.9158900	-3.2182800	-3.2574000
-15.641600	-15.393900	-16.995900		-13.981500	-13.814900	-7.2102200	-7.0524800
-45.232400	-45.716900	-47.276500		-46.674700	-47.032200	-22.740500	-23.076000
-91.914700	-91.074800	-93.665700		-101.68600	-101.08200	-43.001500	-42.443300
-192.95500	-194.36300	-195.33900		-215.25600	-216.21100	-96.882000	-97.834700
-347.65700	-345.36600	-346.66100		-401.87500	-400.55000	-164.70200	-163.05900
-679.13200	-682.55400	-667.87500		-769.59200	-771.56000	-330.83400	-333.31400
930.34200	933.96600	940.84200		1077.5700	1079.9700	440.81300	443.05700

energy bands was observed along the directions parallel to \mathbf{b}_3 . Thus, only the \mathbf{k} -points from the middle plane were needed for a determination of the density of states. The scaling factors used to weight the symmetry points in the irreducible wedge are listed in Table VIII.

The core energies of the $(\text{ZnSe})_1(\text{ZnS})_1$ SLS were roughly equivalent to the non-relativistic Herman-Skillman atomic core energies, as shown in Table XI, and showed no significant dispersion throughout the first Brillouin zone. The electronic band structure and total density of states (TDOS) near the forbidden band gap region for the $(\text{ZnSe})_1(\text{ZnS})_1$ SLS are shown in Figure 11 and the partial density of states (PDOS) is shown in Figure 12. Of the four correspondence relations in Eq. (4.1), the easiest one to visualize is the $\bar{\Gamma} \leftrightarrow \Gamma + X_z$. The Γ_{1v} and X_{1v} states map into the two $\bar{\Gamma}_{1v}$ states. From an orbital composition analysis (OCA), the lower of the two states is S 3s in nature, while the other is Se 4s in nature. For the upper valence states, associated with the Se 4p and S 3p states through an OCA, this folding produces four SLS states from the three zincblende states. The three-fold degenerate Γ_{15v} state is broken by the elastic strain into a two-fold degenerate $\bar{\Gamma}_{5v}$ state consisting of the heavy-hole and split-off states and a $\bar{\Gamma}_{4v}$ light-hole state. The heavy-hole and split-off states remain degenerate due to the non-relativistic nature of the FLCAO calculations. The spin-orbit splitting energy determined by Shionoya (130) can, however, be used to break this degeneracy so that the heavy-hole state assumes the role of valence band maximum. Through an OCA, the $\bar{\Gamma}_{5v}$ state was found to be localized in the Se layer, while the $\bar{\Gamma}_{4v}$ state was delocalized with roughly equivalent probability in the Se and S layers. The two-fold degenerate X_{5v} state corresponds to a two-fold degenerate $\bar{\Gamma}_{5v}$ state and the X_{3v} state corresponds to a $\bar{\Gamma}_{4v}$ state. The two lowest conduction states, associated with the Zn 4s states through an OCA, produced by this folding are $\bar{\Gamma}_{1c}$ states. The lowest in energy corresponds to the Γ_{1c} state (which remains the conduction band minimum) and the other to the X_{1c} state. The next four lowest conduction states, associated with the Zn 4p states through an OCA, correspond to the X_{3c} state and the

TABLE XI
 CALCULATED ATOMIC CORE-LIKE ENERGIES
 OF THE $(\text{ZnSe})_1(\text{ZnS})_1$ SLS

(All values are in electron volts.)

Atomic Core State	N-R H-S Atomic Core Energy ^a	$(\text{ZnSe})_1(\text{ZnS})_1$ SLS Atomic Core-Like Energy
Se 1s	-12415.97	-12496.62
Zn 1s	-9502.43	-9560.81
S 1s	-2447.49	-2453.69
Se 2s	-1596.01	-1603.34
Se 2p	-1441.49	-1441.11
Zn 2s	-1158.14	-1164.67
Zn 2p	-1027.96	-1029.23
S 2s	-224.63	-225.55
Se 3s	-218.70	-219.71
S 2p	-171.81	-172.14(1)
Se 3p	-164.06	-163.89(1)
Zn 3s	-133.24	-135.33
Zn 3p	-90.63	-92.09(1)

^a Reference (74)

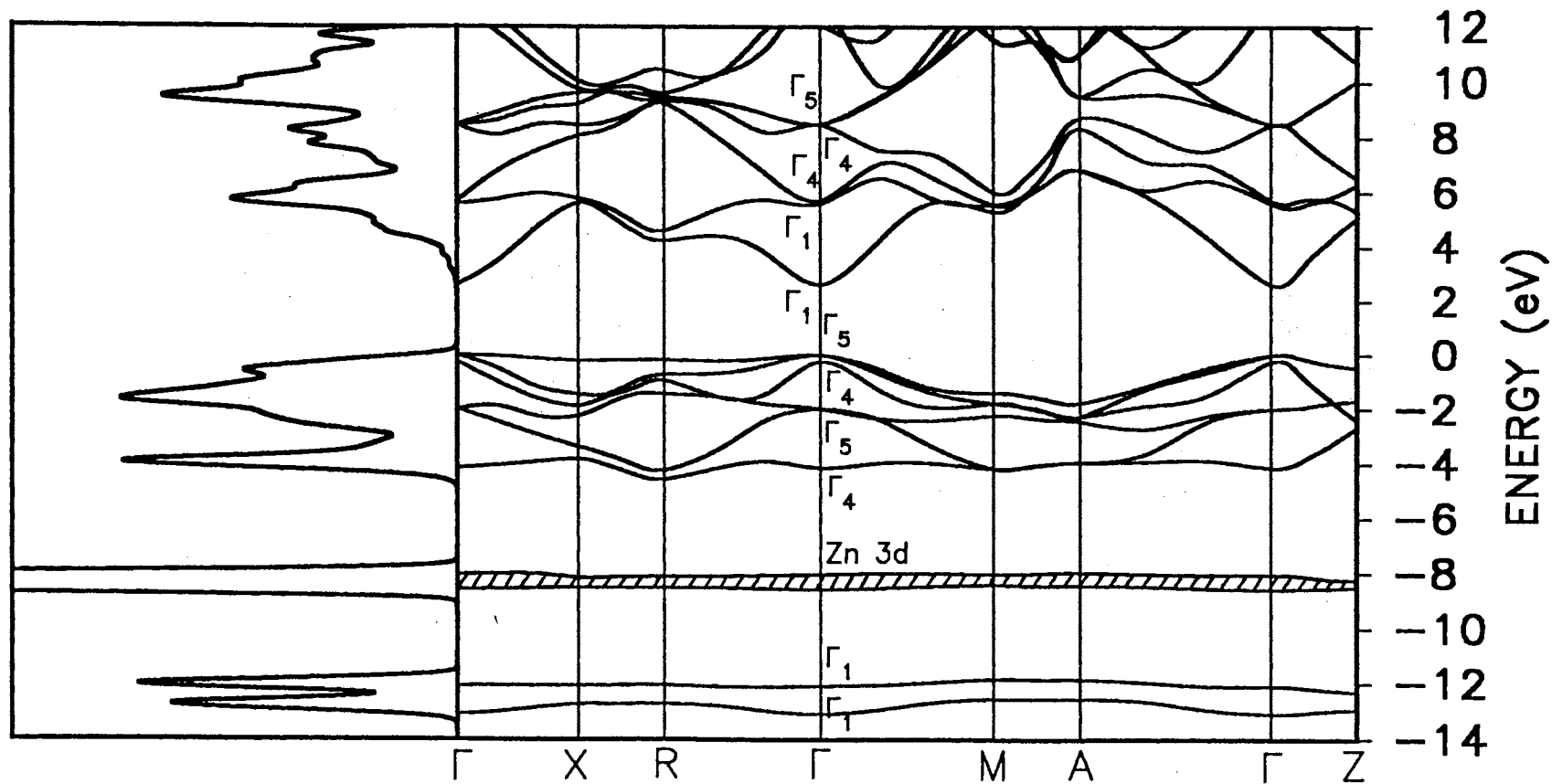


Figure 11. The electronic band structure and total density of states of the $(\text{ZnSe})_1(\text{ZnS})_1$ SLS. The band gap remained direct and the three-fold degenerate bulk valence band maximum is broken by the strain into a two-fold degenerate state consisting of the heavy-hole and split-off states and a non-degenerate light-hole state.

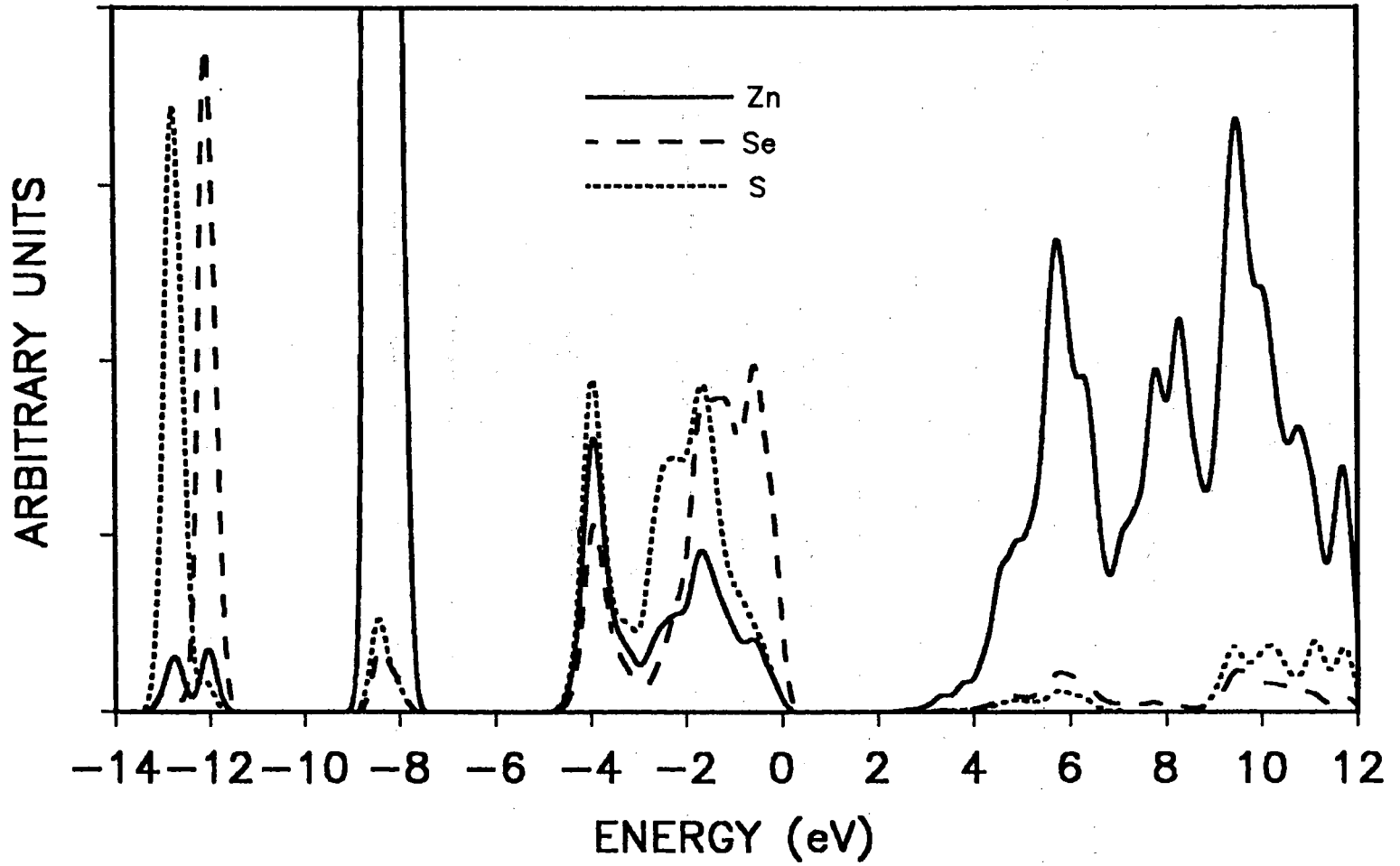


Figure 12. The average partial density of states for the Zn, Se, and S atoms in the $(\text{ZnSe})_1(\text{ZnSe})_1$ SLS.

three-fold degenerate Γ_{15c} state. The X_{3c} state corresponds to one of the two $\bar{\Gamma}_{4c}$ states (the one which is lower in energy) and the Γ_{15c} state is broken into the other $\bar{\Gamma}_{4c}$ state and a two-fold degenerate $\bar{\Gamma}_{5c}$ state. Table XII lists the calculated energies for the $(\text{ZnSe})_1(\text{ZnS})_1$ SLS at the Γ -point, along with the results of Bernard and Zunger and of Nakayama. Where degeneracies are broken, the representation in the zincblende structure is given followed by the new representation in the SLS structure. The values inside the parentheses indicate the degeneracies. While it appears that the Zn 3d X_{3v} and X_{5v} states are degenerate and the $\bar{\Gamma}_{1v}$, $\bar{\Gamma}_{3v}$, and X_{4v} states are degenerate, this is not the case. Instead, they are only near degeneracies. The disparity between the calculated energy values from the FLCAO and PVMB methods is the same as was seen for the bulk compounds. From the PDOS, it can be seen that the two lower valence bands have a dominant anion character: the lower being S 3s in character and the upper being the Se 4s character. For the upper valence bands, the localization of the heavy-hole state in the Se layer is also clearly observed, so that it can be associated with a Se 4p state. The light-hole state and the remaining upper valence states are a mix between Se 4p and S 3p states, with an additional contribution from the Zn 4s state. The Zn 4s contribution is strongest for the lowest of these bands. The lower conduction bands are clearly seen to be dominant Zn 4s and 4p states.

The difference in energy between the light-hole and heavy-states at the band edge as a function of the number of monolayers is shown in Figure 13. In all cases, the heavy-hole state lies above the light-hole state indicating that the (001) free-standing $(\text{ZnSe})_m(\text{ZnS})_n$ SLS's are strained-induced heavy-hole gap heterostructures. For $m,n=2$ and 3, the energy separation between the two states follow an upward trend (solid curve). The localization of the heavy-hole state in the Se layers becomes more distinct, while the light-hole state is found to more localized in the Se layers (55% Se 4p and 39% S 3p at the $\bar{\Gamma}$ -point for $m,n=3$). The Zn 4s conduction states receives contributions from all three types of Zn atoms in the unit cell. For

TABLE XII
 CALCULATED ENERGIES AT THE $\bar{\Gamma}$ -POINT
 FOR THE $(\text{ZnSe})_1(\text{ZnS})_1$ SLS

(All values are in electron volts and measured with respect
 to the top of the valence band maximum.)

Symmetry Point	FLCAO	PVMB ^a	SCP ^b
Se 4s / S 3s states			
Γ_{1v} (1)	-13.10	-13.01	-11.6
X_{1v} (1)	-12.09	-11.85	-10.3
Zn 3d states			
$\Gamma_{15v} \rightarrow \bar{\Gamma}_{4v}$ (1)	-8.57	-7.78	
$\Gamma_{15v} \rightarrow \bar{\Gamma}_{5v}$ (2)	-8.56	-7.78	
X_{3v} (1)	-8.38	-7.65	
X_{5v} (2)	-8.38	-7.53	
$\Gamma_{12v} \rightarrow \bar{\Gamma}_{1v}$ (1)	-8.23	-7.40	
$\Gamma_{12v} \rightarrow \bar{\Gamma}_{3v}$ (1)	-8.23	-7.40	
X_{4v} (1)	-8.23	-7.33	
X_{1v} (1)	-8.02	-7.12	
Upper Valence Bands			
X_{3v} (1)	-4.14	-4.84	-3.8
X_{5v} (2)	-1.99	-2.33	-1.8
$\Gamma_{15v} \rightarrow \bar{\Gamma}_{4v}$ (1)	-0.24	-0.06	-0.15
$\Gamma_{15v} \rightarrow \bar{\Gamma}_{5v}$ (2)	0.00	0.00	0.00
Conduction Bands			
Γ_{1c} (1)	2.63	1.61	2.5
X_{1c} (1)	5.62	3.06	3.4
X_{3c} (1)	5.72	3.70	4.1
$\Gamma_{15c} \rightarrow \bar{\Gamma}_{4c}$ (1)	8.47	6.08	6.6
$\Gamma_{15c} \rightarrow \bar{\Gamma}_{5c}$ (2)	8.50	6.07	6.6

^a Reference (101).

^b Reference (118).

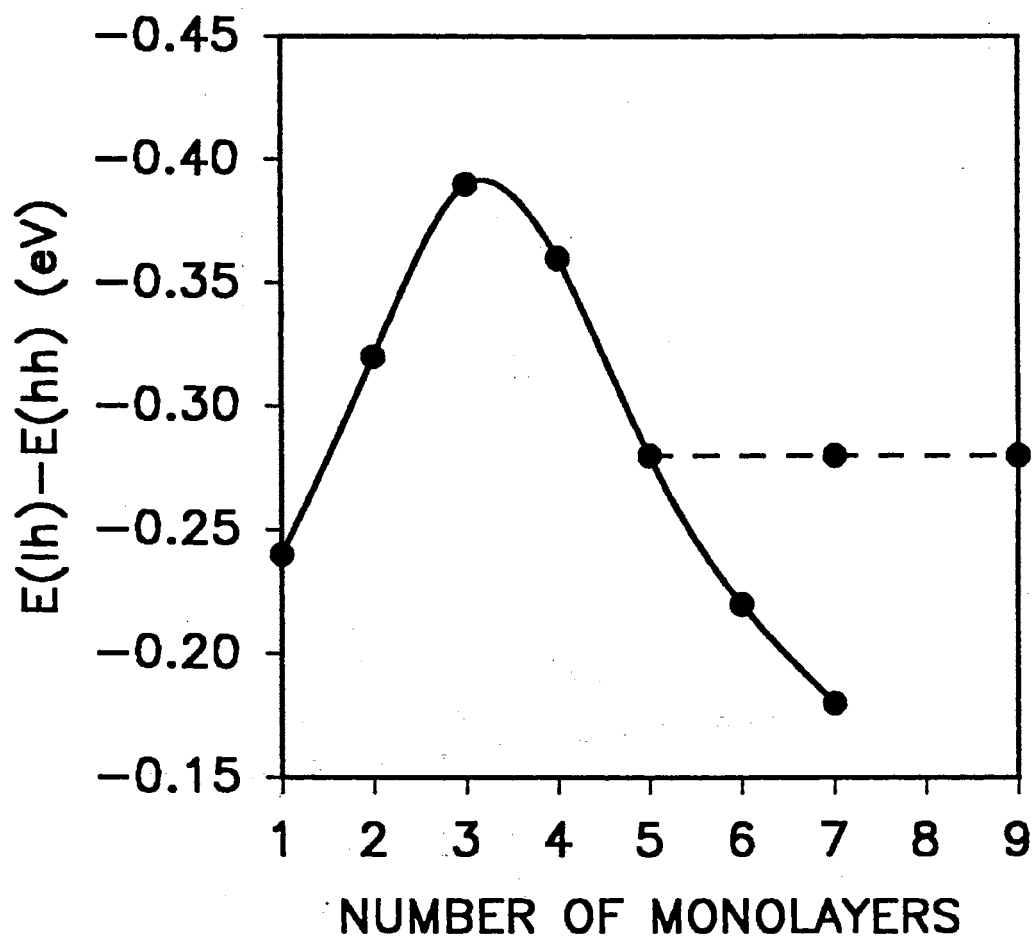


Figure 13. The difference in energy between the light-hole and heavy-hole states at the band edge as a function of the number of monolayers. The solid curve represents the $(ZnSe)_m(ZnS)_m$ SLS's and the dashed line represents the $(ZnSe)_5(ZnS)_n$ SLS's.

$m, n=3$, the contributions at the $\bar{\Gamma}$ -point to the lowest conduction state are roughly equivalent (33% from Zn at the interfaces, 27% from Zn between Se layers, and 34% from Zn between S layers) so that this state is delocalized all along the structure. For $m, n \geq 4$, the energy separation between the two states follows a downward trend (solid curve). Through a OCA, it was seen that both the heavy- and light-hole states are localized in the Se layers. The strongest contributions to the heavy-hole state are from the middle Se layers, while the contribution from the Se layer next to the interface is insignificant. Thus, the heavy-hole state is said to be localized deep within the ZnSe monolayers. The light-hole state, on the other hand, receives its strongest contributions from the first few layers near the interface and receives a negligible contribution from the middle Se layers. The lowest conduction state, however, remains delocalized all along the structure, receiving a roughly equivalent contribution from all of the Zn layers in the structure. The strongest contributions are from the middle Zn layers between S layers and the weakest contributions are from the middle Zn layers between the Se layers. When the number of ZnSe monolayers was frozen at $m=5$ and the number of ZnS monolayers was increased ($n=5, 7, \text{ and } 9$), the energy separation between the light- and heavy-hole states remained constant (dashed line). The localization of the two states in the Se layers showed no dependency on the number of ZnS monolayers. In all three cases, the strongest contributions to the heavy-hole state are approximately 28% from the middle ZnSe monolayer, 22% from each of the adjacent ZnSe monolayers, and 10% from each of the ZnSe monolayers at the interface. The strongest contributions to the light-hole state are approximately 25% from each of the ZnSe monolayers at the interface and 18% from each of the adjacent ZnSe monolayers. The light-hole state received no contribution from the middle ZnSe monolayer. In addition, the lowest conduction state remains delocalized, receiving its strongest contributions from the middle ZnS monolayers ($\sim 10\%$) and its weakest contributions from the middle ZnSe monolayers ($\sim 6\%$). The average PDOS of the $(\text{ZnSe})_7(\text{ZnS})_7$ SLS and the $(\text{ZnSe})_5(\text{ZnS})_9$ SLS for the seven types of atoms in the unit cell are shown in Figures 14-16 and 17-19, where the delocalization of the lowest conduction state throughout the Zn layers is clearly seen. The

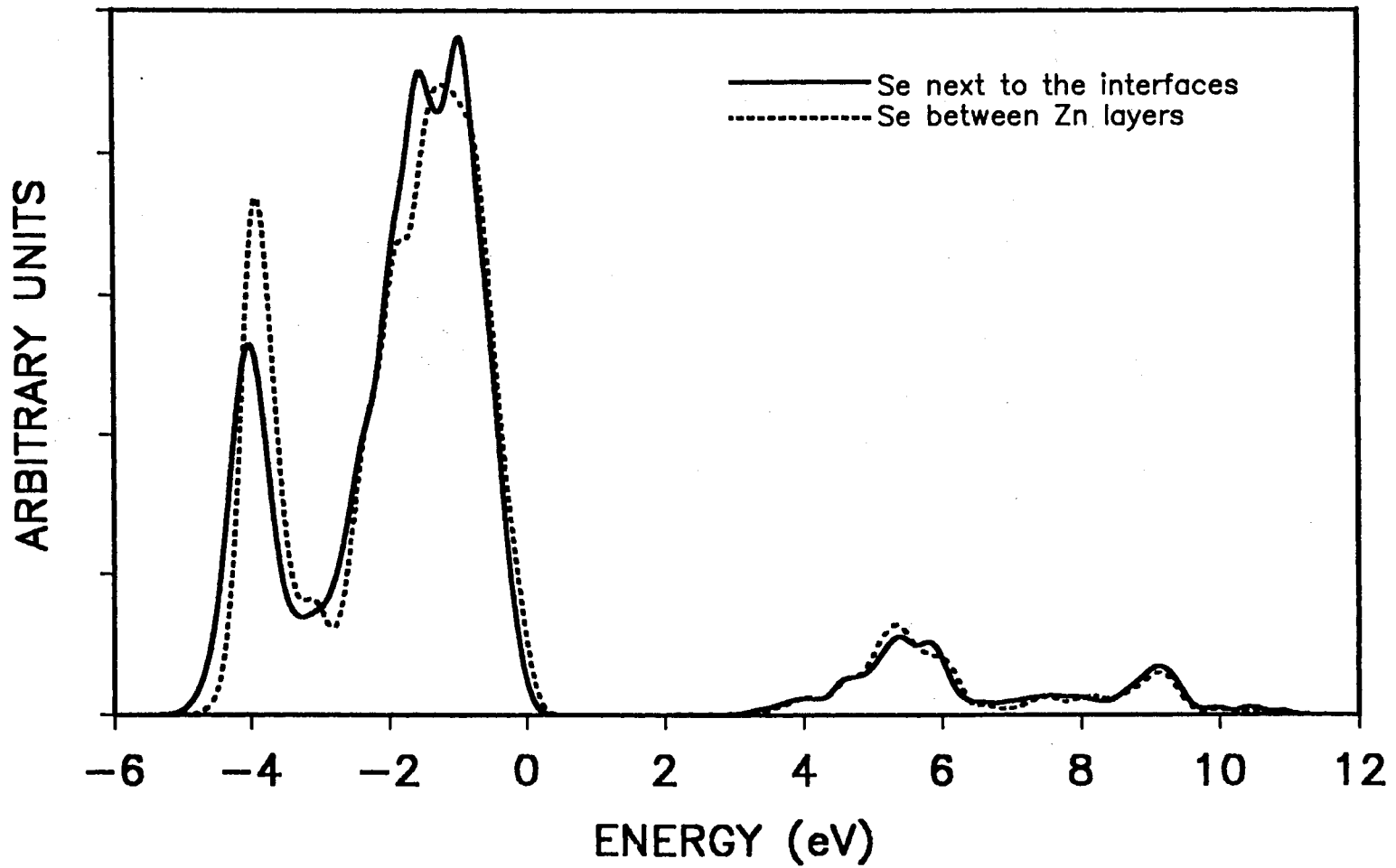


Figure 14. The average partial density of states for the two classifications of Se atoms in the $(\text{ZnSe})_7(\text{ZnS})_7$ SLS.

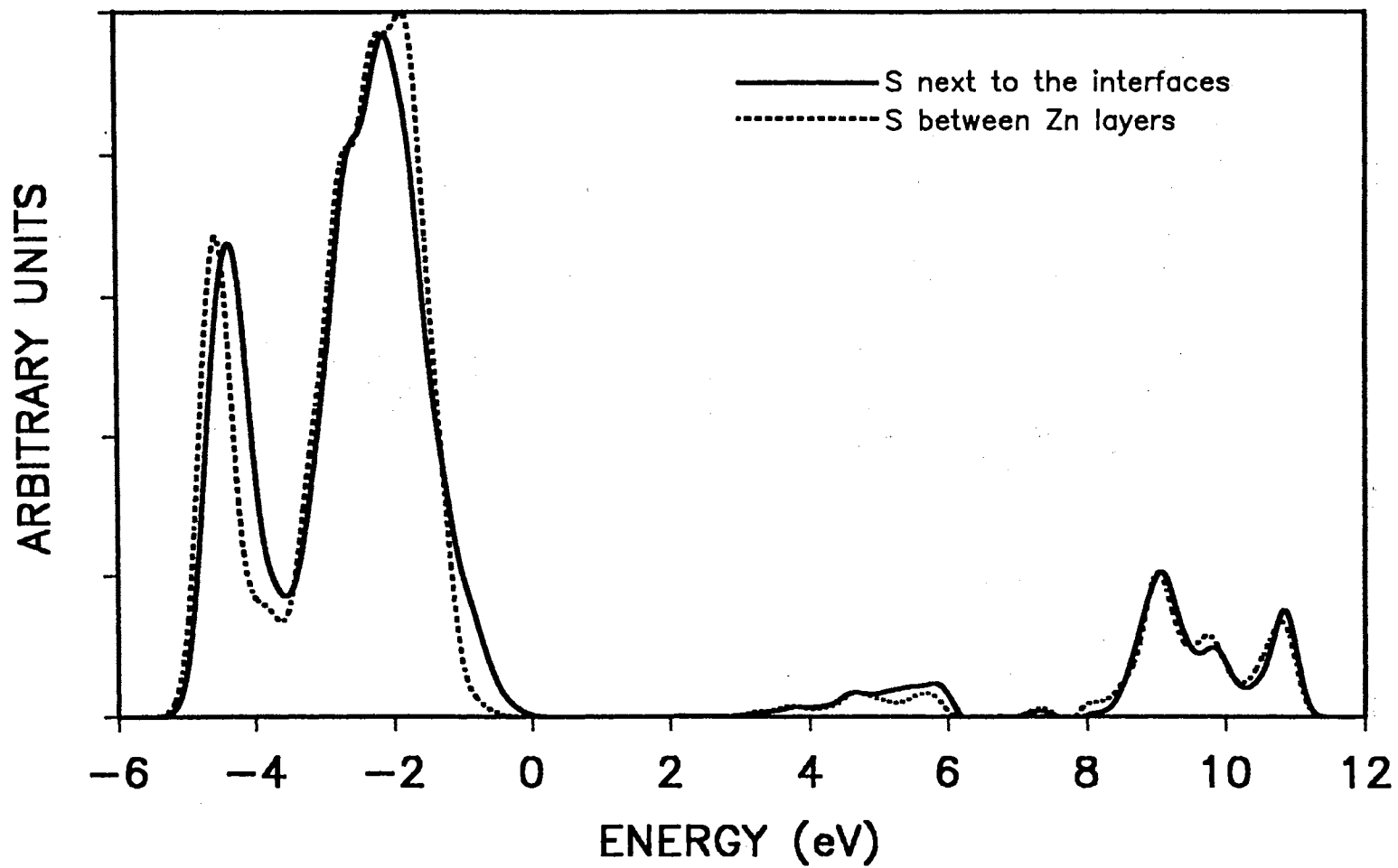


Figure 15. The average partial density of states for the two classifications of S atoms in the $(\text{ZnSe})_7(\text{ZnS})_7$ SLS.

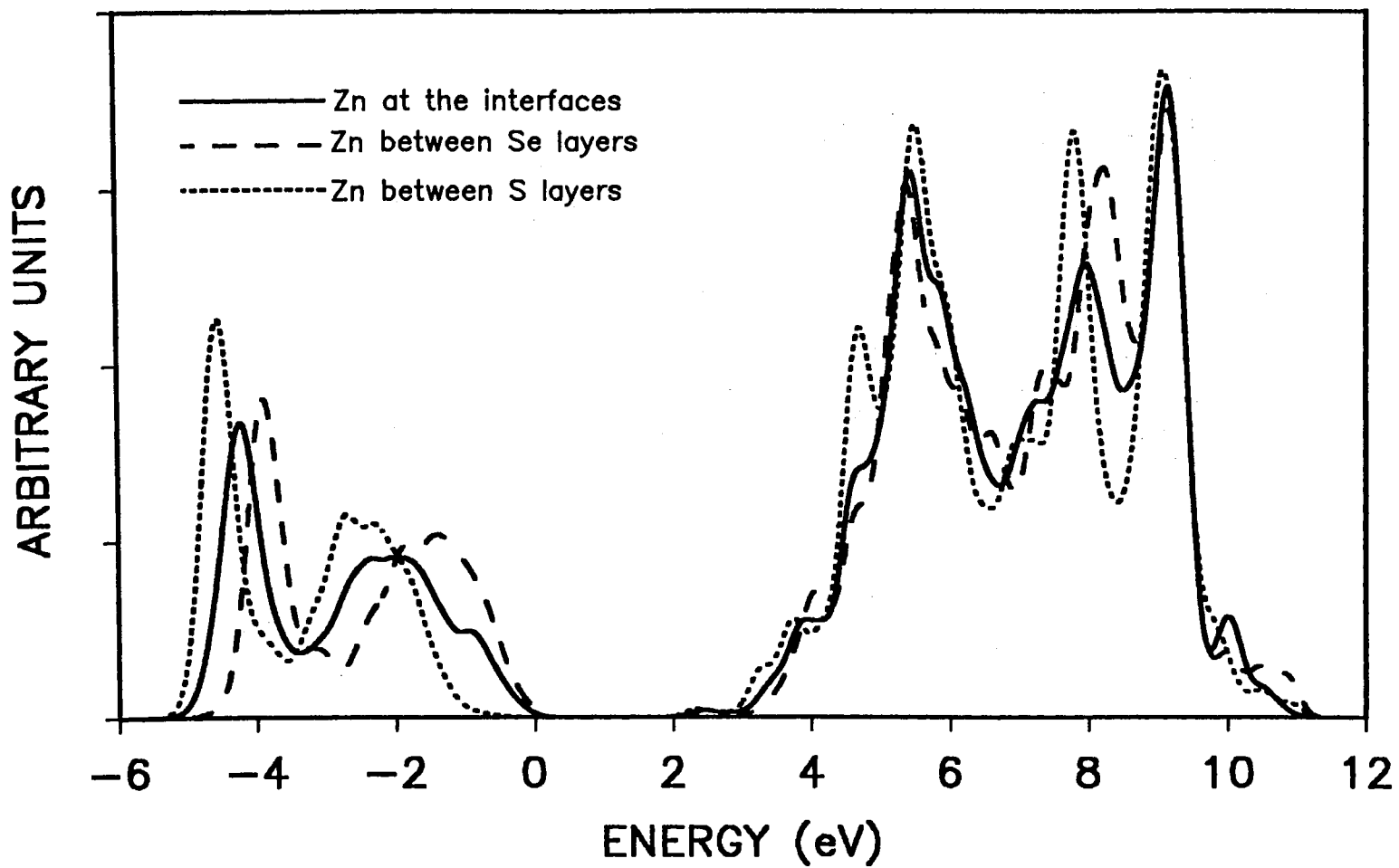


Figure 16. The average partial density of states for the three classifications of Zn atoms in the $(\text{ZnSe})_7(\text{ZnS})_7$ SLS.

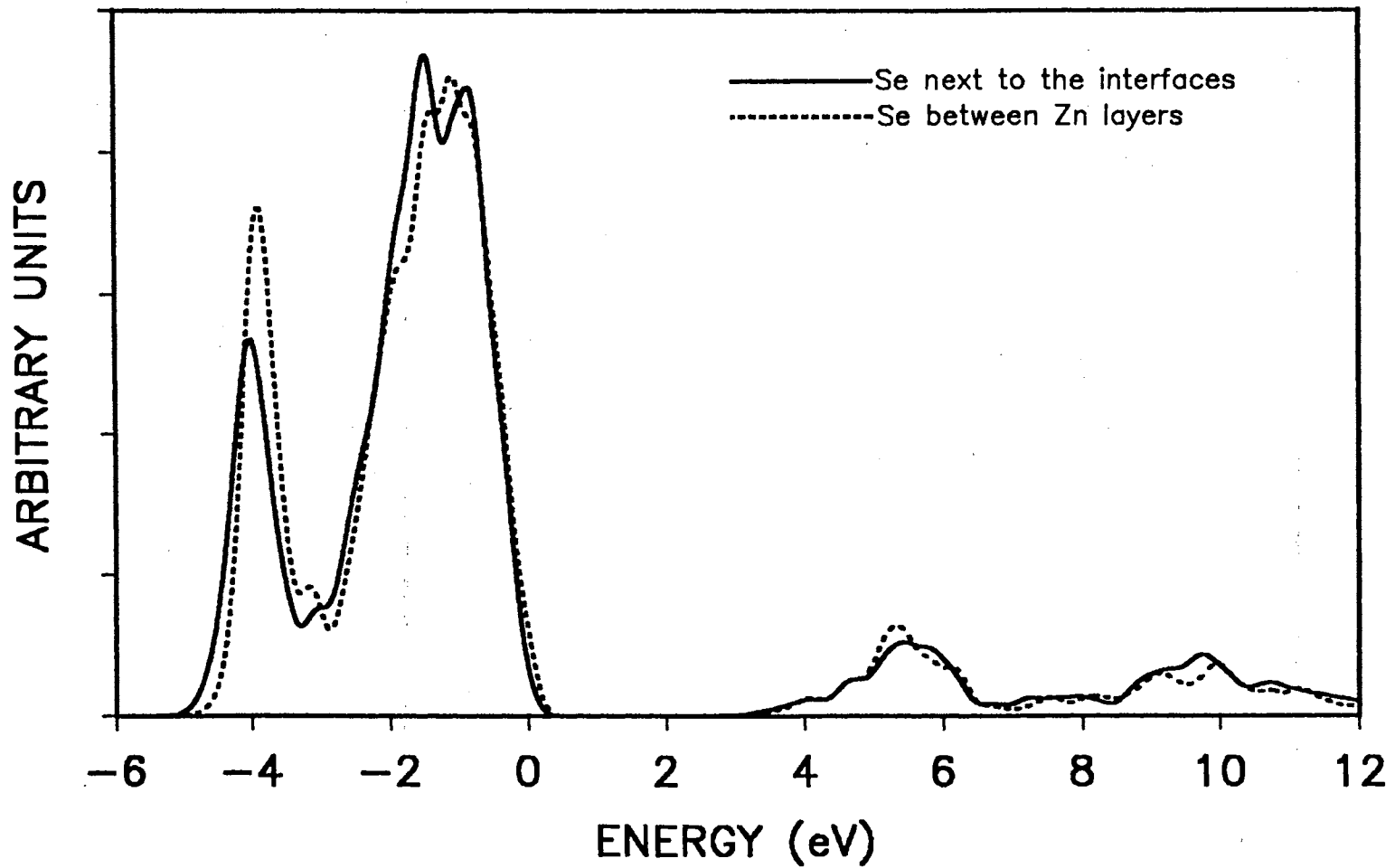


Figure 17. The average partial density of states for the two classifications of Se atoms in the $(\text{ZnSe})_5(\text{ZnS})_9$ SLS.

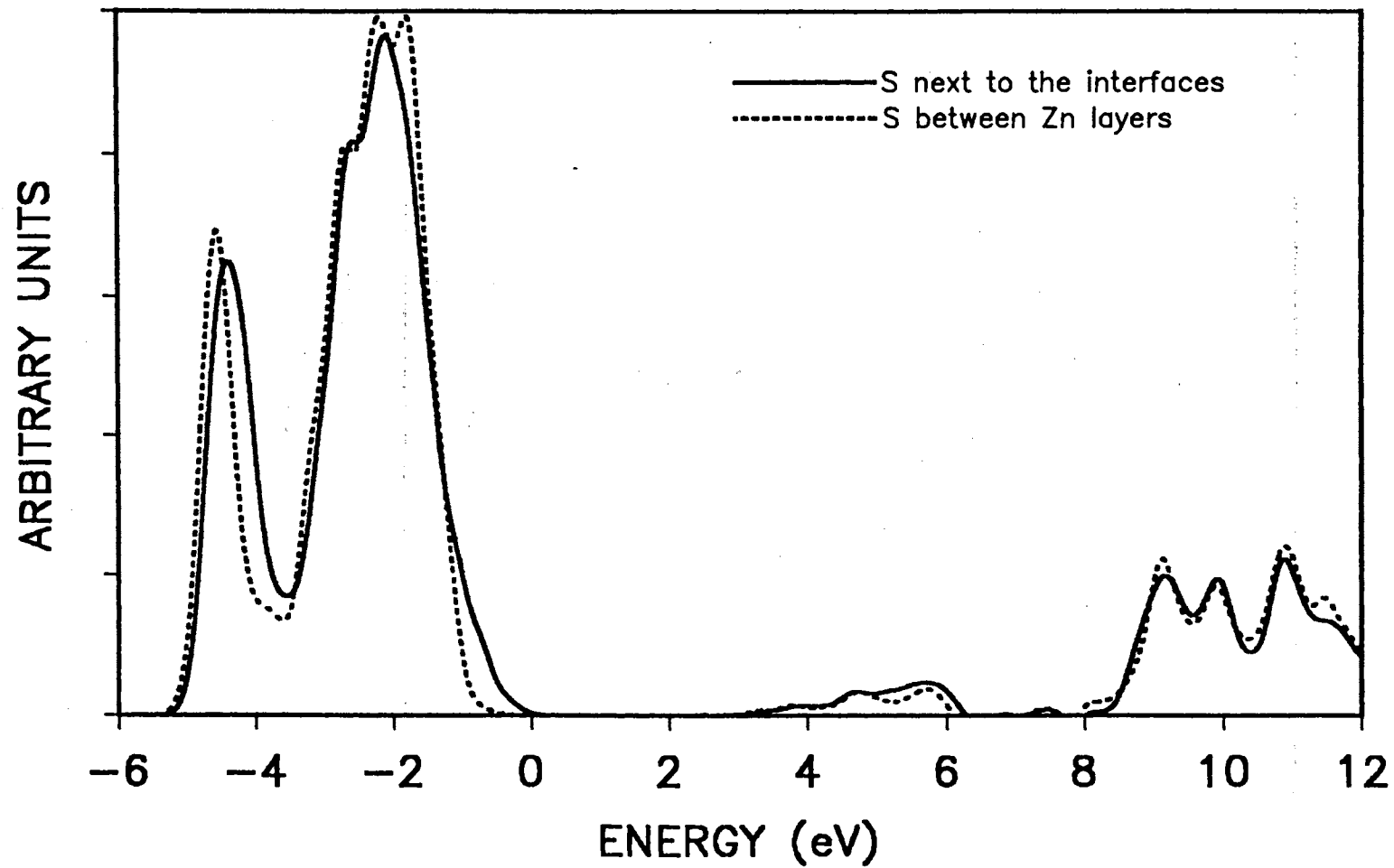


Figure 18. The average partial density of states for the two classifications of S atoms in the $(\text{ZnSe})_5(\text{ZnS})_9$ SLS.

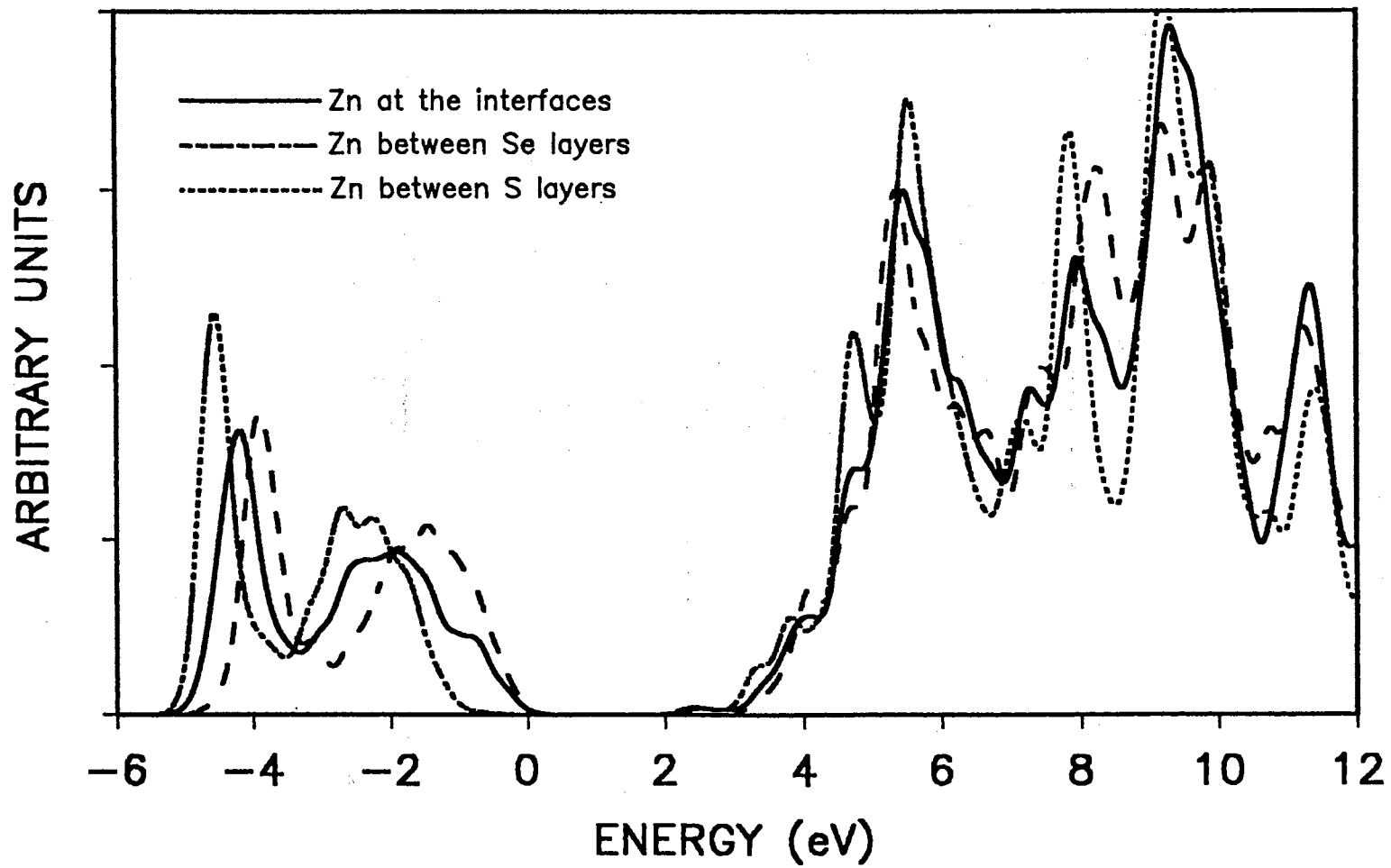


Figure 19. The average partial density of states for the three classifications of Zn atoms in the $(\text{ZnSe})_5(\text{ZnS})_9$ SLS.

localization of the heavy- and light-hole states in the Se layers is clearly seen by overlapping the average PDOS of the Zn, Se, and S atoms, as is shown in Figures 20 and 21 for the two SLS's. In both cases, the valence band offset is estimated to be roughly 1.0 eV. These results suggest a large valence band offset offering a strong confinement of the holes in the ZnSe quantum wells and a small conduction band offset offering a weak confinement of the electrons.

The band gaps determined from these electronic structure calculations remained direct, as was assumed. The band gap energy of the $(\text{ZnSe})_m(\text{ZnS})_m$ SLS's follows a downward trend as the number of monolayers is increased, as shown in Figure 22, similar to the one found in the semi-empirical calculations of Wu *et al.* For $m=1$, the band gap energy was determined to be 2.63 eV, which is approximately two tenths of an eV higher than the calculated band gap energy of bulk ZnSe (short dashed line). For $m=4$, the band gap energy was equal to that of bulk ZnSe. With a further increase in the number of monolayers, the band gap energy continued its downward trend and showed no signs of leveling off. This behavior supports the conclusion of Kawakami *et al.* (15) that there is a transition from a type-I to a type-II superlattice for certain combinations of the $\{m,n\}$ values. These results, however, are insufficient to confirm such a transition because of the nature of the nonself-consistent calculations and the known error in the bulk band gaps. For $m \geq 3$, the calculated band gap energy for m =odd is roughly equal to the subsequent m =even value. Thus, the band gap energy appears to have a step-like dependency with the number of monolayers. A smooth curve can be obtained, however, by considering only the m =odd (solid curve) or m =even values for the number of monolayers.

An attractive feature assumed of the $(\text{ZnSe})_m(\text{ZnS})_n$ SLS's is the ability to manipulate the band gap energy through the set of $\{m,n\}$ values. To lower the band gap energy would require, it is believed, an increase in the number of ZnSe monolayers. An increase in the number of ZnS monolayers should then have the opposite effect, an increase in the band gap energy. This effect was studied through the electronic structure calculations of the $(\text{ZnSe})_5(\text{ZnS})_n$ SLS's for $n=5, 7, \text{ and } 9$ (long dashed curve) in an effort to bring the band gap

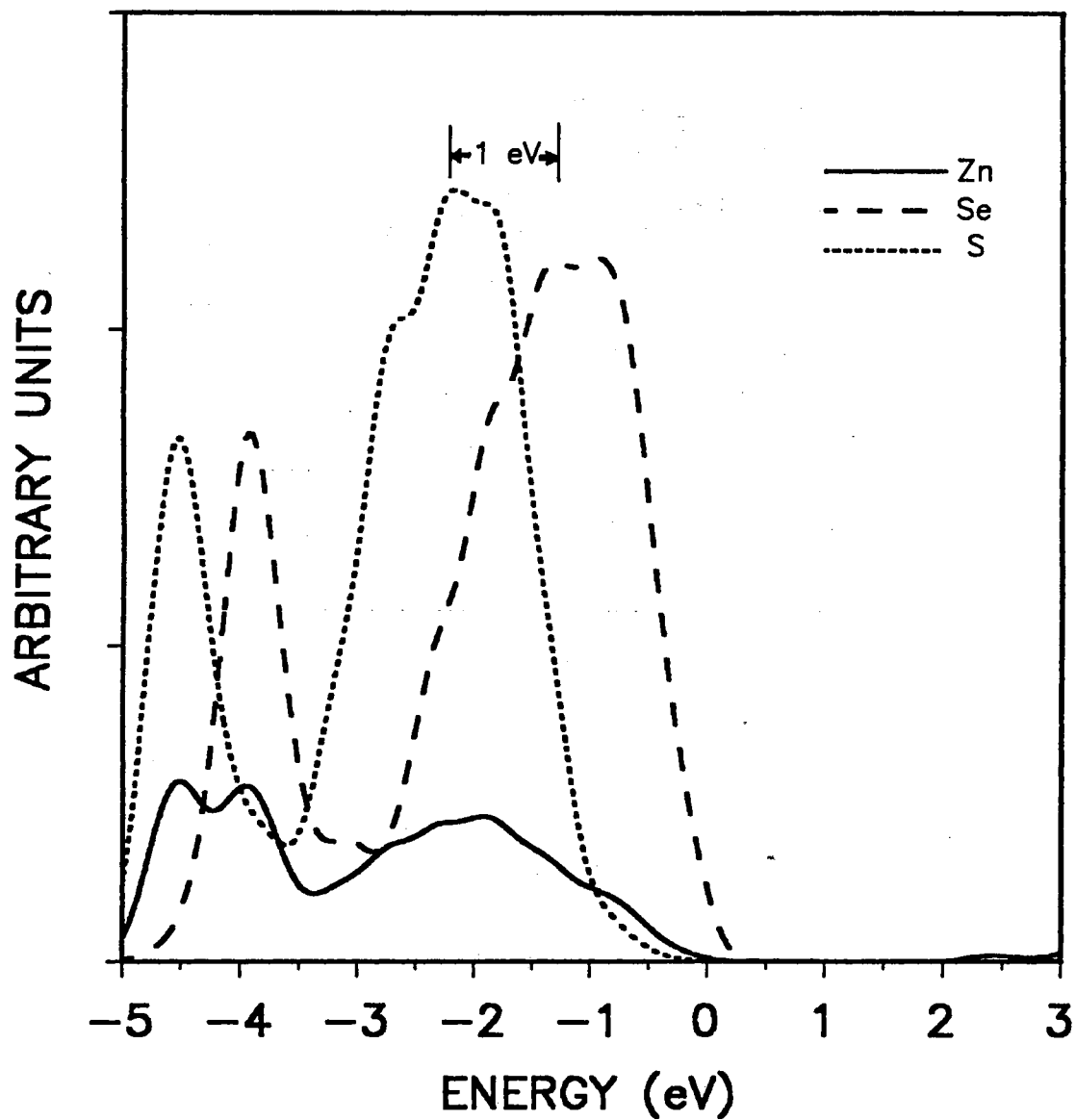


Figure 20. The partial density of states for the Zn, Se, and S atoms in the $(\text{ZnSe})_7(\text{ZnS})_7$ SLS showing the localization of the heavy- and light-hole states in the Se layers. The valence band offset was estimated to be 1.0 eV.

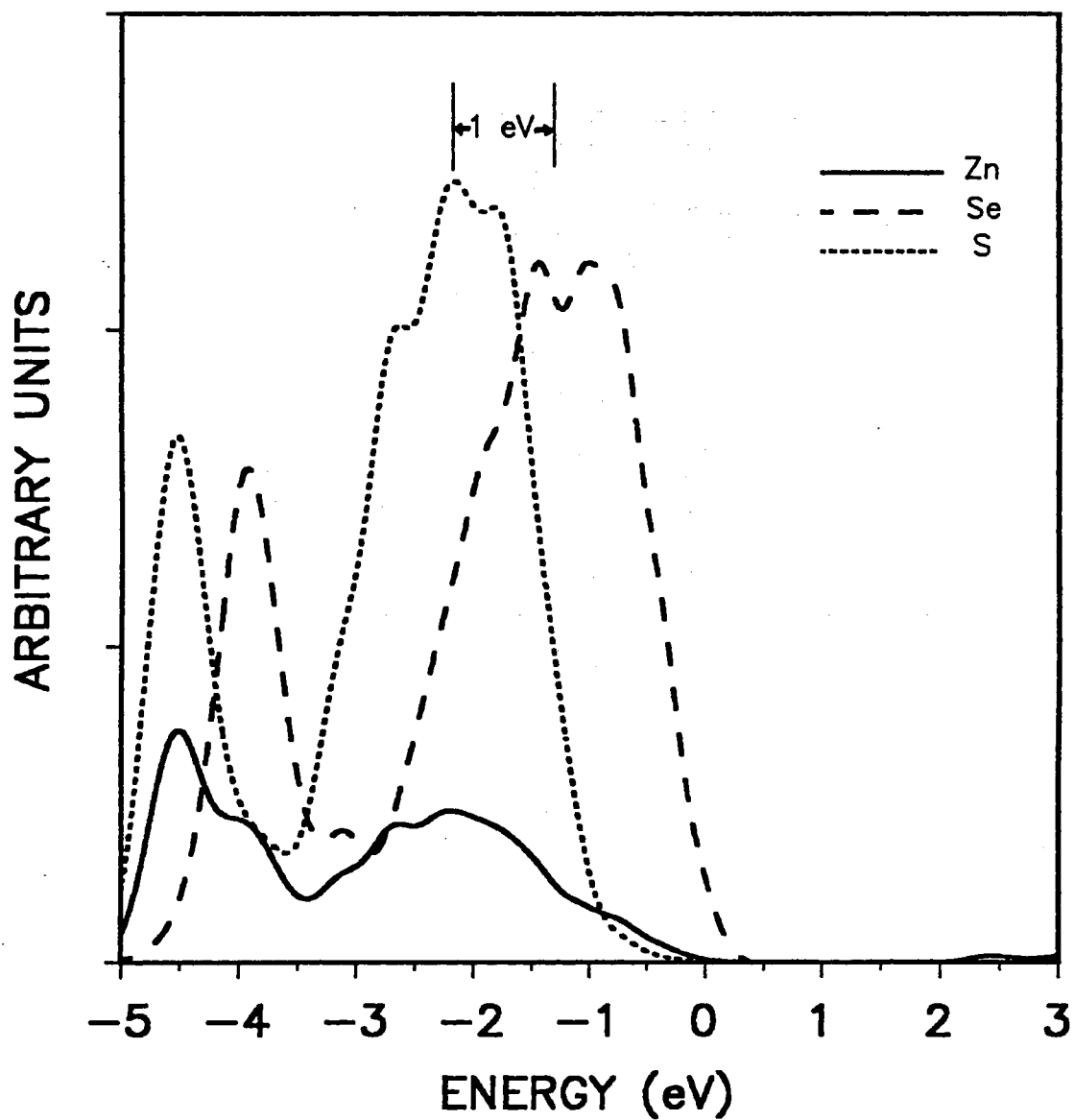


Figure 21. The partial density of states for the Zn, Se, and S atoms in the $(\text{ZnSe})_5(\text{ZnS})_9$ SLS showing the localization of the heavy- and light-hole states in the Se layers. The valence band offset was estimated to be 1.0 eV.

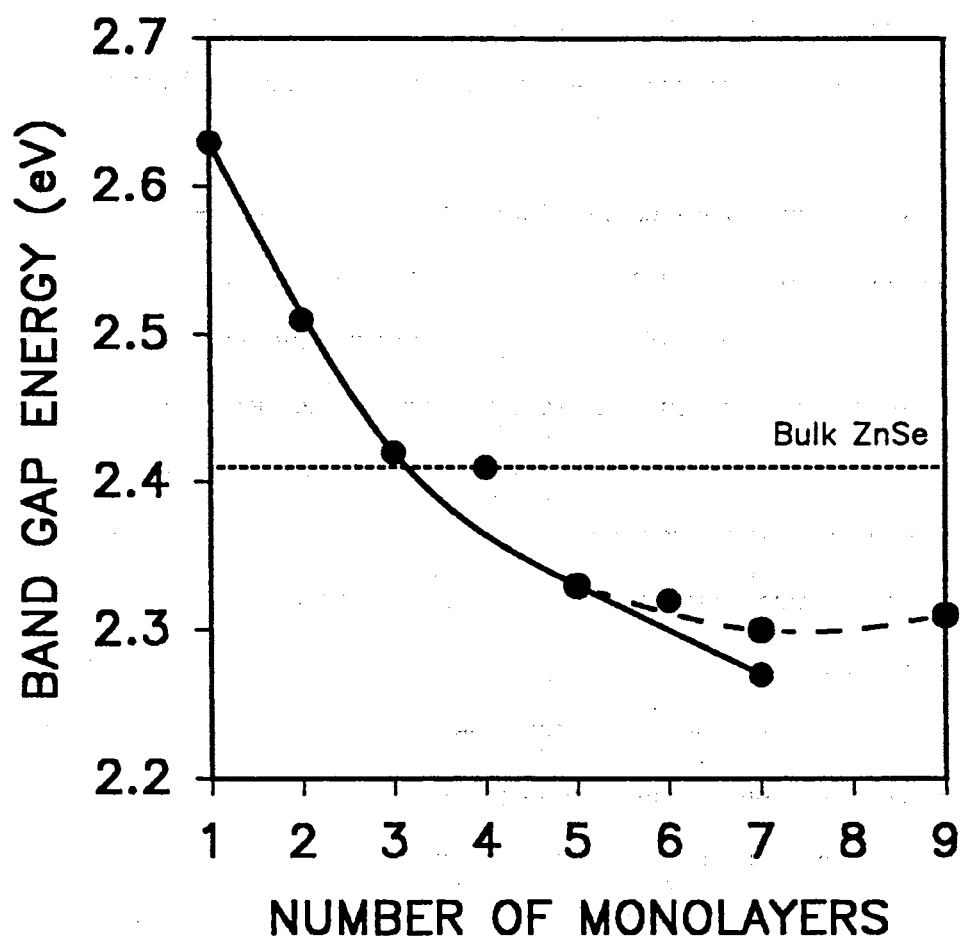


Figure 22. The band gap energy for the $(\text{ZnSe})_m(\text{ZnS})_n$ SLS's. For both $m, n = \text{odd}$ (solid curve) and $m, n = \text{even}$, the band gap energy follows a steady downward trend and drops below the bulk ZnSe value (short dashed line). For $m=5$ and $n=5, 7,$ and 9 (long dashed curve), the band gap energy levels off.

energy back above the bulk ZnSe value. The calculated energy was 2.33 eV for $n=5$ and decreased to 2.30 eV for $n=7$. For $n=9$, however, the energy showed a small increase to 2.31 eV. This result suggests if not an upward trend, then at least a leveling off of the band gap energy.

Band Offsets

The monolayers used to construct a SLS are generally considered to be either part of the strained bulk-like region or the interfacial region. The bulk-like region is effectively isolated from the interfaces and is expected to have characteristics which are similar to those of the corresponding bulk compound. The interfacial region, on the other hand, has a much more complex behavior due to the charge redistribution and possible dislocations found at the interfaces. The band offsets can then be expressed as the sum of the bulk-like and interfacial contributions

$$\Delta E_{\text{offset}} = \Delta E_{\text{offset}}^{\text{bulk-like}} + \Delta E_{\text{offset}}^{\text{interfacial}} \quad (4.25)$$

In this work, the heterostructures were assumed to be free of dislocations and the strain has been accounted for through the VFF model. In nonself-consistent calculations, though, it is not possible to account for the charge redistribution. In their study of common-anion SLS's, however, Wei and Zunger (131) have shown that the contribution to the valence band offset from the interfacial region is small and can be ignored. Furthermore, they have proposed that their core-level model can be applied to common-cation SLS's as long as the superlattice is sufficiently large. In the core-level model, the valence band offset is expressed as

$$\Delta E_{\text{VBO}} = (E_{\alpha}^{\text{ZnS}} - E_{\alpha}^{\text{ZnSe}}) - (\epsilon_{\alpha}^{\text{ZnS}} - \epsilon_{\alpha}^{\text{ZnSe}}), \quad (4.26)$$

where α denotes a atomic-like cation core state at the band edge, $E_{\alpha}^{\text{ZnS}} - E_{\alpha}^{\text{ZnSe}}$ the apparent chemical shift (ACS) and $\epsilon_{\alpha}^{\text{ZnS}} - \epsilon_{\alpha}^{\text{ZnSe}}$ the true chemical shift (TCS). The ACS, given in Table XIII for each of the cation core states, was determined from the bulk compound calculations of the previous chapter. The TCS, given in Table XIV for each of the cation core states, was determined from the $(\text{ZnSe})_7(\text{ZnS})_7$ SLS calculation. The average values, discarding the Zn 1s

TABLE XIII

THE APPARENT CHEMICAL SHIFT FOR
THE ATOMIC-LIKE Zn CORE STATES

(All values are in electron volts and measured with respect
to the corresponding bulk valence band maximum.)

α	E_{α}^{ZnS}	E_{α}^{ZnSe}	$E_{\alpha}^{\text{ZnS}} - E_{\alpha}^{\text{ZnSe}}$
Zn 1s	-9547.62	-9550.69	3.07
Zn 2s	-1153.42	-1154.52	1.10
Zn 2p	-1018.14	-1019.08	0.94
Zn 3s	-124.14	-125.18	1.04
Zn 3p	-80.92	-81.93	1.01

TABLE XIV

THE TRUE CHEMICAL SHIFT FOR THE
ATOMIC-LIKE Zn CORE STATES

(All values are in electron volts and are measured with respect to a material independent reference.)

α	$\epsilon_{\alpha}^{\text{ZnS}}$	$\epsilon_{\alpha}^{\text{ZnSe}}$	$\epsilon_{\alpha}^{\text{ZnS}} - \epsilon_{\alpha}^{\text{ZnSe}}$
Zn 1s	-9558.41	-9559.57	1.16
Zn 2s	-1164.46	-1164.49	0.03
Zn 2p	-1029.24	-1029.19	-0.05
Zn 3s	-135.27	-135.18	-0.09
Zn 3p	-92.09	-92.02	-0.07

results, are 1.02 eV for the ACS and -0.04 for the TCS. The resulting valence band offset has a value of 1.06 eV and suggests a strong confinement of the holes in the ZnSe quantum wells.

Using the core-level model notation, the conduction band offset can be expressed as

$$\Delta E_{\text{CBO}} = (E_{\alpha}^{\text{ZnS}} - E_{\alpha}^{\text{ZnSe}}) - (E_{\text{g}}^{\text{ZnS}} - E_{\text{g}}^{\text{ZnSe}}) - (\epsilon_{\alpha}^{\text{ZnS}} - \epsilon_{\alpha}^{\text{ZnSe}}), \quad (4.27)$$

where E_{α}^{ZnS} and E_{α}^{ZnSe} are the calculated bulk compound band gap energies (3.51 eV for ZnS and 2.41 eV for ZnSe). The resulting conduction band offset has a value of -0.04 eV and suggests a negligible confinement of the electrons in the ZnS quantum wells. Both offset values are in excellent agreement with the estimated offsets from the partial density of states calculations.

The valence band offset determined from the core-level model, however, is roughly twice the size of the one calculated by Christensen *et al* even though the Zn 3d states were treated as fully relaxed states in both the FLCAO and LMTO calculations. To determine if this discrepancy occurs as a result of differences between the *ab initio* methods or the offset models, the valence and conduction band offsets for the $(\text{ZnSe})_m(\text{ZnS})_m$ SLS's for $m \geq 3$ and the $(\text{ZnSe})_5(\text{ZnS})_n$ SLS's for $n=10, 15, \text{ and } 20$ have been calculated using the frozen-potential model. Primitive non-rectangular two-atom unit cells were constructed for bulk-like ZnSe and ZnS using the lattice parameters from the middle monolayers of the SLS's, which are given in Tables IX and XV. Electronic structure calculations at the band edge were then performed on the bulk-like compounds to determine the absolute energy of the upper valence and CBM states. For both bulk-like compounds, the strain split the three-fold degenerate VBM found in the true bulk compounds into a two-fold degenerate (heavy-hole and split-off) state and a light-hole state. The degenerate state was at the higher energy for bulk-like ZnSe (-10.01 eV to -10.26 eV), while the light-hole state had the higher energy for bulk-like ZnS (-10.95 eV to -11.13 eV). In all cases, there was a strain induced lowering of the band gap energy for both bulk-like compounds (~0.05 eV for ZnSe and ~0.30 eV for ZnS). Such a lowering is expected for bulk-like ZnS, but not for bulk-like ZnSe. The valence band offset is then expressed as the energy

TABLE XV
LATTICE PARAMETERS FOR THE BULK-LIKE
ELECTRONIC STRUCTURE CALCULATIONS

(All values are in atomic units.)

{m,n}	a_{xy}	d_{Zn-Se} (middle)	d_{Zn-S} (middle)
5,10	5.1805	2.7862	2.5069
5,15	5.1621	2.7972	2.5197
5,20	5.1514	2.8117	2.5271

difference of the bulk-like ZnS light-hole state and the bulk-like ZnSe heavy-hole state

$$\Delta E_{\text{VBO}} = E_{\text{rh}}^{\text{bulk-like ZnS}} - E_{\text{hh}}^{\text{bulk-like ZnSe}} \quad (4.28)$$

and the conduction band offset is expressed as the energy difference of the bulk-like conduction band minimums

$$\Delta E_{\text{CBO}} = E_{\text{CBM}}^{\text{bulk-like ZnS}} - E_{\text{CBM}}^{\text{bulk-like ZnSe}} \quad (4.29)$$

Similar to the core-level model, the band offsets determined from the frozen-potential model do not receive any contribution from the interfacial region. The resulting band offsets are listed in Table XVI and show little dependency on the number of ZnS monolayers. The band offsets are in excellent agreement with those determined using the core-level model and those estimated from the density of states. Thus, the discrepancy in the values presented in this work and those from the work of Christensen *et al* result from the differences between the *ab initio* FLCAO and LMTO methods. This discrepancy, however, is not the result of the FLCAO calculations being nonself-consistent. The electronic structure of bulk ZnSe and ZnS determined by this method has already been shown to be in good agreement with other *ab initio* calculations and with photoemission and reflectivity measurements. This agreement is also expected to be present in the bulk-like calculations of the frozen-potential model.

The results of this band offset study indicate a large valence band offset (~1.0 eV), which suggests a strong confinement of the holes in the ZnSe quantum wells. This confinement is in excellent agreement with the results of the electronic band structure calculations, where the heavy- and light-hole states were determined to be localized in the ZnSe monolayers. The near vanishing conduction band offset (~-0.1eV) suggests a weak confinement of the electrons. The negative value would indicate a type-II superlattice, where the ZnS monolayers would act as a quantum well to the electrons. This result is also in agreement with the electronic band structure calculations, where the lowest conduction state was determined to be roughly delocalized all along the structure. Through an OCA, the middle Zn layers between S layers was found to give the strongest contribution to this state. This

TABLE XVI
THE CALCULATED BAND OFFSETS OF
THE $(\text{ZnSe})_m(\text{ZnS})_n$ SLS's

(All values are in electron volts.)

m,n	ΔE_{VBO}	ΔE_{CBO}
m,n \neq 3	0.94	-0.16
5,10	1.02	-0.16
5,15	1.05	-0.15
5,20	1.07	-0.14

analysis could be interpreted as indicating the ZnS monolayers do serve as quantum wells to the electrons, but only offer a weak confinement. Due to the nature of nonself-consistent calculations and the small value of the conduction band offset, however, the results suggest that the $(\text{ZnSe})_m(\text{ZnS})_n$ SLS's do not form either a type-I or type-II superlattice.

CHAPTER V

CONCLUSIONS

The FLCAO Method

The strength of the FLCAO method is that for unit cells having some form of rectangular symmetry the factorization of the energy matrix elements into x-, y-, and z-components effectively reduces a N^3 problem down to a $3N$ one. The computational time saved using this factorization technique can easily be seen in Table XVI, which compares the needed time for the evaluation of the kinetic energy and overlap matrix elements and the potential energy matrix elements of the bulk compounds (primitive non-rectangular unit cell) and the ultra short-period SLS's (primitive rectangular unit cell). The computational time needed for the evaluation of the kinetic energy and overlap matrix elements is roughly proportional to the number of basis functions, irrespective of the unit cell's symmetry. Thus, the factorization technique offers no significant time savings for these elements. However, the computational burden has always been with the evaluation of the potential energy matrix elements and it is with these elements that the FLCAO method excels. The computational time needed for the evaluation of the potential energy matrix elements of the $(\text{ZnSe})_2(\text{ZnS})_2$ SLS (348 basis functions) is roughly equivalent to the time needed for either bulk compound (72 basis functions for ZnS and 102 basis functions for ZnSe). Thus, the computational burden of evaluating the energy matrix elements can be effectively eliminated through the use of this factorization technique.

On the other hand, the FLCAO method cannot reduce the computational time needed for the diagonalization of the energy matrix. It is this computational burden that has plagued all

TABLE XVII

COMPUTATIONAL TIME^a NEEDED FOR THE EVALUATION
OF THE ENERGY MATRIX ELEMENTS AND THE
DIAGONALIZATION OF THE ENERGY MATRIX

	Bulk ZnSe	Bulk ZnS	(ZnSe) ₁ (ZnS) ₁ SLS	(ZnSe) ₂ (ZnS) ₂ SLS	(ZnSe) ₃ (ZnS) ₃ SLS
Atoms Per Unit Cell	2	2	4	8	12
No. Basis Functions	102	72	174	348	522
KE & Overlap	0 min 18 sec	0 min 16 sec	0 min 29 sec	1 min 2 sec	1 min 40 sec
PE	8 min 34 sec	10 min 59 sec	4 min 23 sec	11 min 29 sec	21 min 38 sec

	Atoms Per Unit Cell	No. Basis Functions	Diagonali- zation
(ZnSe) ₁ (ZnS) ₁ SLS	4	174	2 min 55 sec
(ZnSe) ₂ (ZnS) ₂ SLS	8	348	17 min 55 sec
(ZnSe) ₃ (ZnS) ₃ SLS	12	522	46 min 54 sec
(ZnSe) ₄ (ZnS) ₄ SLS	16	659	105 min 17 sec
(ZnSe) ₅ (ZnS) ₅ SLS	20	870	201 min 47 sec
(ZnSe) ₆ (ZnS) ₆ SLS	24	1044	346 min 14 sec
(ZnSe) ₇ (ZnS) ₇ SLS	28	1218	545 min 26 sec
(ZnSe) ₅ (ZnS) ₇ SLS	24	1014	317 min 26 sec
(ZnSe) ₅ (ZnS) ₉ SLS	28	1185	534 min 38 sec

^a Scalar FLCAO code run on a IBM 3090-200S supercomputer.

ab initio and semi-empirical electronic structure calculations. As can also be seen from Table XVII, the amount of computational time required for a single iteration at each \mathbf{k} -point is non-linearly proportional to the number of basis functions. An additional burden for self-consistent calculations is that five iterations are generally needed to reach self-consistency. This restriction on the size of the problem which can be effectively handled has become obvious in the study of SLS's where electronic structure calculations have been limited to the short-period SLS's, which are not even fabricated due to growth difficulties. To remain an effective tool in the study of the electronic properties of today's complex crystals, vastly improved techniques for the diagonalization of the energy matrix must be developed for use in electronic structure calculations. One proposed method to reduce this computational burden is through the use of the Sturm sequences, which is a diagonalization technique (which can utilize parallel processors) used to determine the energy eigenvalues within a specified range (132). To achieve a significant time savings, though, only about 25% of the energy eigenvalues can be considered. Since the core energies are generally known to be close to the atomic core energies, however, the specified range can be used to determine the valence and lower conduction energies.

The $(\text{ZnSe})_m(\text{ZnS})_n$ SLS's

The objective of this work was to evaluate the $(\text{ZnSe})_m(\text{ZnS})_n$ SLS's as potential candidates for use in the development of optoelectronic devices. While no single study can arrive at a definitive conclusion, the results of this study do indicate that these SLS's have certain characteristics which remain unchanged with respect to the number of monolayers. From the electronic band structure calculations, the heavy- and light-hole states were found to be localized in the Se layers. The lowest conduction state, on the other hand, was determined to be delocalized. The strongest contributions to this state were from the middle Zn layers between S layers, while the weakest contributions were from the middle Zn layers between Se layers. The valence band offset was determined to be large (~ 1 eV), indicating that the heavy-

and light-holes would be confined in the ZnSe quantum wells. This proposed confinement of the heavy- and light-holes is in excellent agreement with the localization of the heavy- and light-hole states in the ZnSe monolayers. The near vanishing conduction band offset (~ 0.1 eV) indicates a negligible confinement of the electrons and suggests that the $(\text{ZnSe})_m(\text{ZnS})_n$ SLS's do not form either type of superlattice. This weak confinement of the electrons is in excellent agreement with the delocalization of the lowest conduction state and the temperature dependence photoluminescence study of Kuwabara *et al* (33) on the ZnSe (50 Å) - ZnS (50 Å) SLS. At low temperature, the PL emission lines were interpreted to be due to free excitons, where both the electrons and holes are confined in quantum wells. At room temperature, however, the PL emission lines were associated with band edge transitions. Furthermore, the localization of the heavy- and light-holes and the valence band offset were found to be roughly independent of the number of ZnS monolayers. This would suggest that for a sufficiently large enough number of ZnS monolayers, there would not be any significant overlapping of the excitonic wave functions between ZnSe sublattices. As a result, the electrons could be effectively localized in a single ZnSe sublattice at low temperatures and the electronic properties, specifically the band gap energy, could then be fine-tuned through the number of ZnS monolayers (the FLCAO results do indicate a possible upward trend of the band gap energy when n is increased). However, the results also suggest that the $(\text{ZnSe})_m(\text{ZnS})_n$ SLS's do not appear to be promising candidates for use in the development of a efficient room temperature blue LED.

BIBLIOGRAPHY

1. Kawakami, Y. and Taguchi, T., J. Vac. Sci. Technol. B 5, 1171 (1987).
2. Kawakami, Y. and Taguchi, T., J. Vac. Sci. Technol. B 7, 789 (1989).
3. Yamada, Y. and Taguchi, T., J. Cryst. Growth 101, 661 (1990).
4. Parbrook, P. J., Wright, P. J., Cockayne, B., Cullis, A. G., Henderson, B., and O'Donnell, K. P., J. Cryst. Growth 106, 503 (1990).
5. Wright, P. J., Cockayne, B., Parbrook, P. J., Jones, A. C., O'Brien, P., and Walsh, J. R., J. Cryst. Growth 104, 601 (1990).
6. O'Donnell, K. P., Parbrook, P. J., Henderson, B., Trager, C., Chen, X., Yang, F., Halsall, M. P., Wright, P. J., and Cockayne, B., J. Cryst. Growth 101, 554 (1990).
7. Shen, D. Z., Fan, X. W., Fan, G. H., Chen, L. C., Li, D. F., and Liu, Y. D., Acta Opt. Sinica 10, 643 (1990).
8. Yokogawa, T., Ogura, M., and Kajiwara, T., Appl. Phys. Lett. 49, 1702 (1986).
9. Yokogawa, T. and Narusawa, T., J. Cryst. Growth 115, 673 (1991).
10. Teraguchi, N., Takemura, Y., Kimura, R., Konagai, M., and Takahashi, K., J. Cryst. Growth 93, 720 (1988).
11. Taike, A., Teriguchi, N., Konagai, M., and Takahashi, K., Jpn. J. Appl. Phys. 26, L989 (1987).
12. Oniyama, H., Yamaga, S., and Yoshikawa, A., Jpn. J. Appl. Phys. 28, L2137 (1989).
13. Shen, A., Cui, J., Wang, H., and Wang, Z., SPIE 1519, 656 (1991).
14. Kawakami, Y., Taguchi, T., Satou, M., and Hiraki, A., Nucl. Instrum. Methods B 33, 603 (1988).
15. Kawakami, Y., Taguchi, T., and Hiraki, A., J. Cryst. Growth 89, 331 (1988).
16. Wu, Y. H., Yang, H., Ishida, A., Fujiyasu, H., Nakashima, S., and Tahara, K., Appl. Phys. Lett. 54, 239 (1989).
17. Yang, H., Fujiyasu, H., Wu, Y. H., Ishida, A., and Kuwabara, H., J. Lumin. 40&41, 717 (1988).
18. McCaldin, J. O., McGill, T. C., and Mead, C. A., Phys. Rev. Lett. 36, 56 (1976).

19. Kawakami, Y., Taguchi, T., and Hiraki, A., *J. Cryst. Growth* **93**, 714 (1988).
20. Yamada, Y., Masumoto, Y., Taguchi, T., and Takemura, K., *Phys. Rev. B* **44**, 1801 (1991).
21. Yamada, Y., Masumoto, Y., and Taguchi, T., *Surf. Sci.* **267**, 129 (1992).
22. Yamada, Y., Masumoto, Y., and Taguchi, T., *J. Cryst. Growth* **117**, 484 (1992).
23. Yokogawa, T., Saitoh, T., and Narusawa, T., *Appl. Phys. Lett.* **58**, 1754 (1991).
24. Guan, Z. P., Zhang, J. H., Fan, G. H., Fan, X. W., *J. Cryst. Growth* **117**, 515 (1992).
25. Guan, Z. P., Fan, G. H., Fan, X. W., and Yu, J. Q., *J. Lumin.* **53**, 355 (1992).
26. Guan, Z. P., Fan, X. W., Fan, G. H., and Xu, X. R., *J. Lumin.* **45**, 224 (1990).
27. Sack, W., Oberhauser, D., O'Donnell, K. P., Parbrook, P. J., Wright, P. J., Cockayne, B., and Klingshirn, C., *J. Lumin.* **53**, 409, (1992).
28. O'Donnell, K. P., Parbrook, P. J., Yang, F., Chen, X., Irvine, D. J., Trager-Cowan, C., Henderson, B., Wright, P. J., and Cockayne, B., *J. Cryst. Growth* **117**, 497 (1992).
29. Oberhauser, D., Sack, W., Klingshirn, C., O'Donnell, K. P., Parbrook, P. J., Wright, P. J., and Cockayne, B., *Superlatt. and Micro.* **9**, 107 (1991).
30. Yang, F., Parbrook, P. J., Henderson, B., O'Donnell, K. P., Wright, P. J., and Cockayne, B., *Appl. Phys. Lett.* **59**, 2142 (1991).
31. O'Donnell, K. P., Parbrook, P. J., Henderson, B., Trager-Cowan, C., Chen, X., Yang, F., Halsall, M. P., Wright, P. J., and Cockayne, B., *J. Cryst. Growth* **101**, 554 (1990).
32. Shen, A., Wang, H., and Wang, Z., *Appl. Phys. Lett.* **60**, 2640 (1992).
33. Kuwabara, Fujiyasu, H., Shimizu, H., Sasaki, A., and Yamada, S., *J. Cryst. Growth* **72**, 229 (1985).
34. Slater, J. C., *Phys. Rev.* **81**, 385 (1951).
35. Kohn, W. and Sham, L. J., *Phys. Rev.* **140**, A1133 (1965).
36. Slater, J. C., Wilson, T. M., and Wood, J. H., *Phys. Rev.* **170**, 28 (1969).
37. Wilson, T. M., Wood, J. H., and Slater, J. C., *Phys. Rev. A* **2**, 620 (1970).
38. Ceperley, D. M., *Phys. Rev. B* **18**, 3126 (1978).
39. Ceperley, D. M., and Alder, B. J., *Phys. Rev. Lett.* **45**, 566 (1980).
40. Perdew, J. P., and Zunger, A., *Phys. Rev. B* **23**, 5048 (1981).
41. Bullett, D. W., "Solid State Physics, Advances in Research and Applications," ed. by Seitz, F. and Turnbull, D. (Academic Press, New York), vol. 35, p. 129.

42. Huang, M. and Ching, W. Y., J. Phys. Chem. Solids 46, 977 (1985).
43. Wang, C. S. and Klein, B. M., Phys. Rev. B 24, 3393 (1981).
44. Wang, C. S. and Klein, B. M., Phys. Rev. B 24, 3417 (1981).
45. Heaton, R. and Lafon, E., J. Phys. C 14, 347 (1981).
46. Heaton, R. and Lafon, E., Phys. Rev. B 17, 1958 (1978).
47. Simmons, J. E., Lin, C. C., Fouquet, D. F., Lafon, E. E., and Chaney, R. C., J. Phys. C 8, 1549 (1975).
48. Ching, W. Y. and Callaway, J., Phys. Rev. B 9, 5115 (1974).
49. Menzel, W. P., Lin, C. C., Fouquet, D. F., Lafon, E. E., and Chaney, R. C., Phys. Rev. Lett. 30, 1313 (1973).
50. Kervin, P. W. and Lafon, E. E., J. Chem. Phys. 58, 1535 (1973).
51. Chaney, R. C., Lafon, E. E., and Lin, C. C., Phys. Rev. B 4, 2734 (1971).
52. Chaney, R. C., Tung, T. K., Lin, C. C., and Lafon, E. E., J. Chem. Phys. 52, 361 (1970).
53. Lafon, E. E. and Lin, C. C., Phys. Rev. 152, 579 (1966).
54. Wu, J. Z., Trickey, S. B., and Boettger, J. C., Phys. Rev. B 42, 1663 (1990).
55. Boettger, J. C. and Trickey, S. B., J. Phys.: Condens. Matter 1, 4323 (1989).
56. Boettger, J. C. and Trickey, S. B., Phys. Rev. B 34, 3604 (1986).
57. Mintmire, J. W., Sabin, J. R., and Trickey, S. B., Phys. Rev. B 26, 1743 (1982).
58. Metha-Ajmani, M., Batra, I. P., Lafon, E. E., and Fadley, C. S., J. Phys. C 13, 2807 (1980).
59. Ching, W. Y. and Lin, C. C., Phys. Rev. B 16, 2989 (1977).
60. Ching, W. Y. and Lin, C. C., Phys. Rev. B 12, 5536 (1975).
61. Ching, W. Y. and Huang, M., Superlatt. and Micro. 1, 141 (1985).
62. Ching, W. Y., Xu, Y., and Zhao, G., Phys. Rev. Lett. 59, 1333 (1987).
63. Xu, Y., Ching, W. Y., and Wong, K. W., Phys. Rev. B 37, 9773 (1988).
64. Wimmer, E., Krakauer, H., Weinert, M., and Freeman, A. J., Phys. Rev. B 24, 864 (1981).
65. Jansen, H. J. F. and Freeman, A. J., Phys. Rev. B 30, 561 (1984).
66. Anderson, O. K., Phys. Rev. B 12, 3060 (1975).
67. Lafon, E. E., J. Comput. Phys. 83, 185 (1989).

68. Wilson, T. M. and Lafon, E. E., *Int. J. Quantum Chem.* S26, 703 (1992).
69. Wilson, T. M., Lafon, E. E., and Merican, L., (unpublished).
70. Kittel, C., "Introduction to Solid State Physics," (Wiley and Sons, New York, 1986).
71. Ashcroft, N. W. and Mermin, N. D., "Solid State Physics," (Saunders, New York, 1976).
72. Poirier, R., Kari, R., and Csizmadia, I. G., "Handbook Of Gaussian Basis Sets," (Elsevier, New York, 1985).
73. Huzinaga, S., "Gaussian Basis Sets For Molecular Calculations," (Elsevier, New York, 1984).
74. Herman, F. and Skillman, S., "Atomic Structure Calculations," (Prentice-Hall, Englewood Cliffs, N. J., 1963).
75. Szabo, A. and Ostlund, N. S., "Modern Quantum Chemistry," (McGraw-Hill, New York, 1989), Chap. 3.
76. Euwema, R. N., *Phys. Rev. B* 4, 4322 (1971).
77. Batra, I. P., (private communication).
78. Mulliken, R. S., *J. Chem. Phys.* 23, 1833 (1955).
79. Mulliken, R. S., *J. Chem. Phys.* 23, 1841 (1955).
80. Ciraci, S. and Batra, I. P., *Phys. Rev. B* 15, 3254 (1977).
81. Ciraci, S. and Batra, I. P., *Phys. Rev. B* 15, 4923 (1977).
82. Chelikowsky, J. R., Wagener, T. J., Weaver, J. H., and Jin, A., *Phys. Rev. B* 40, 9644 (1989).
83. Ley, L., Pollak, R. A., McFeely, F. R., Kowalczyk, S. P., and Shirley, D. A., *Phys. Rev. B* 9, 600 (1974).
84. Pollak, R. A., Ley, L., Kowalczyk, S., Shirley, D. A., Joannopoulos, J. D., Chadi, D. J., and Cohen, M. L., *Phys. Rev. Lett.* 29, 1103 (1972).
85. Eastman, D. E., Grobman, W. D., Freeouf, J. L., and Erbudak, M., *Phys. Rev. B* 9, 3473 (1974).
86. Theis, D., *Phys. Stat. Sol. B* 79, 125 (1977).
87. Walter, J. P., Cohen, M. L., Petroff, Y., Balkanski, M., *Phys. Rev. B* 1, 2661 (1970).
88. Petroff, Y., Balkanski, M., Walter, J. P., Cohen, M. L., *Solid State Commun.* Z, 459 (1969).
89. Pantelides, S. T. and Harrison, W. A., *Phys. Rev. B* 11, 3006 (1975).
90. Chadi, D. J. and Cohen, M. L., *Phys. Stat. Sol. (B)* 68, 405 (1975).

91. Bertho, D., Boiron, D., Simon, A., and Jouanin, C., Phys. Rev. B 44, 6118 (1991).
92. Ekpenuma, S. N. and Myles, C. W., J. Phys. Solids 51, 93 (1990).
93. Vogl, P., Hjalmarson, H. P., and Dow, J. D., J. Phys. Chem. Solids 44, 365 (1983).
94. Qteish, A. and Needs, R. J., Phys. Rev. B 45, 1317 (1992).
95. Chelikowsky, J. R. and Cohen, M. L., Phys. Rev. B 14, 556 (1976).
96. Cohen, M. L. and Bergstresser, T. K., Phys. Rev. 141, 789 (1966).
97. Eckelt, P., Madelung, O., and Treusch, J., Phys. Rev. Lett. 18, 656 (1967).
98. Stukel, D. J., Euwema, R. N., Collins, T. C., Herman, F., and Kortum, R. L., Phys. Rev. 179, 740 (1969).
99. Jaffe, J. E., Pandey, R., and Kunz, A. B., J. Phys. Chem. Solids 52, 755 (1991).
100. Christensen, N. E., Gorczyca, I., Christensen, O. B., Schmid, U., and Cardona, M., J. Cryst. Growth 101, 318 (1990).
101. Bernard, J. E. and Zunger, A., Phys. Rev. B 36, 3199 (1987).
102. Martins, J. L., Troullier, N., and Wei, S. H., Phys. Rev. B 43, 2213 (1991).
103. Continenza, A., Massidda, S., and Freeman, A. J., Phys. Rev. B 38, 12996 (1988).
104. Ghahramani, E., Moss, D. J., and Sipe, J. E., Phys. Rev. B 43, 9700 (1991).
105. Marshall, T. S. and Wilson, T. M., Int. J. Quantum Chem. S26, 687 (1992).
106. Hedin, L. and Lundqvist, B. I., J. Phys. C 4, 2064 (1971).
107. Wigner, E., Phys. Rev. 46, 1002 (1934).
108. Wachters, A. J. H., J. Chem. Phys. 52, 1033 (1970).
109. McLean, A. D. and Chandler, G. S., J. Chem. Phys. 72, 5639 (1980).
110. Bertho, D. and Jouanin, C., Phys. Rev. B 47, 2184 (1993).
111. Quiroga, L., Rodriguez, F. J., Camacho, A., and Tejedor, C., Superlatt. and Micro. 10, 455 (1991).
112. Quiroga, L., Rodriguez, F. J., Camacho, A., and Tejedor, C., Phys. Rev. B 42, 11198 (1990).
113. Wu, Y., Fujita, S., Fujita, S., J. Appl. Phys. 67, 908 (1990).
114. Quiroga, L., Camacho, A., Brey, L., and Tejedor, C., Phys. Rev. B. 40, 3955 (1989).
115. Brey, L. and Tejedor, C., Phys. Rev. B 35, 9112 (1987).

116. Tejedor, C., Calleja, J. M., Meseguer, F., Mendez, E. E., Chang, C. A., and Esaki, L., Phys. Rev. B 32, 5303 (1985).
117. Bendt, P. and Zunger, A., Phys. Rev. B 26, 3114 (1982).
118. Nakayama, T., J. Phys. Soc. Jpn. 59, 1029 (1990).
119. Nakayama, T. and Kamimura, H., J. Phys. Soc. Jpn. 54, 4726 (1985).
120. Christensen, N. E. and Gorczyca, I., Phys. Rev. B 44, 1707 (1991).
121. Gorczyca, I. and Christensen, N. E., Solid State Commun. 72, 785 (1989).
122. Christensen, N. E., Phys. Rev. B 37, 4528 (1988).
123. Shahzad, K., Olego, D. J., and Van de Walle, C. G., Phys. Rev. B 38, 1417 (1988).
124. Van de Walle, C. G. and Martin, R. M., Phys. Rev. B 34, 5621 (1986).
125. Bachelet, G. B. and Christensen, N. E., Phys. Rev. B 31, 879 (1985).
126. Qteish, A. and Needs, R. J., Phys. Rev. B 42, 3044 (1990).
127. Musgrave, M. J. P. and Pople, J. A., Proc. Roy. Soc. A 268, 474 (1962).
128. Keating, P. N., Phys. Rev. 145, 637 (1966).
129. Martin, R. M., Phys. Rev. B 1, 4005 (1970).
130. Shionoya, S., "Luminescence in Inorganic Solids," Ed. by Goldberg, P. (Academic, New York, 1966), p. 205.
131. Wei, S. H. and Zunger, A., J. Vac. Sci. Technol. B 5, 1239 (1987).
132. The Sturm sequences was discussed by F. Harris during his presentation at the *1992 Sanibel Symposia*.

2
VITA

TODD S. MARSHALL

Candidate for the Degree of

Doctor of Philosophy

Thesis: *AB INITIO* NONSELF-CONSISTENT FACTORIZED LCAO CALCULATIONS
ON THE ELECTRONIC STRUCTURE OF $(\text{ZnSe})_m(\text{ZnS})_n$ STRAINED-LAYER
SUPERLATTICES

Major Field: Physics

Biographical:

Personal Data: Born in Sanata Barbara, California, June 2, 1962, the son of Richard and Barbara Marshall. Married Sherry Lynn Taylor, July 31, 1993.

Education: Received Bachelor of Science Degree in Mathematics from California State University, Hayward, California in 1984; Master of Science Degree in Physics from San Jose State University, San Jose, California in 1987; completed requirements for the Doctor of Philosophy Degree at Oklahoma State University, Stillwater, Oklahoma in Decemeber, 1993.